

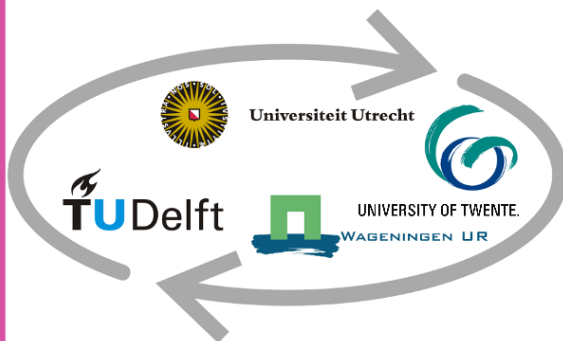
*DEVELOPING OBIA METHODS FOR MEASURING  
PLANT TRAITS AND THE LEGACY OF CROPS USING  
VHR UAV-BASED OPTICAL SENSORS.*

R.J.G. (Rik) Nuijten BSc

Dr.Ir. L. (Lammert) Kooistra

Dr.Ir. R.J.A. (Ron) van Lammeren

Wageningen University and Research





**This dissertation is submitted for the degree of Master of Science**  
**Geographical Information Management and Applications**  
**November 2018**

“In the past, farmers made field-by-field assessments. Today they are moving towards foot-by-foot data collection and analysis to make better decisions.”

(Financial Times 2017)

“Global Market Insights forecasts that the agricultural drone market size will exceed \$1 billion and 200,000 units shipped by 2024. GMI attributes the growth through 2024 to increasing awareness of the pros and cons of drones in agriculture among farmers.”

(Business Insider 2017)

\*foot-by-foot as a distance measure

## ABSTRACT

Unmanned aerial vehicles (UAV) have emerged as a flexible, affordable, and easy-to-use technology for remote sensing within fields such as geoscience, precision agriculture and forestry management. The capacity of taking very high spatial resolution (VHR) optical images makes UAVs highly suitable for individual crop detection and analysis. Following an object-based image analysis (OBIA) approach, the thesis investigates to what extent image-objects can be built for *cichorium endivia* (endive) crops at the end of the growing season. The main capabilities of OBIA are delivering a highly accurate detection of crops (99.8% accuracy) and precise measuring of crop-covered areas without including any shadows or bare soil.

Hyperspectral data and a digital surface model (DSM) are combined with the OBIA-based image-objects, so-called data fusion. These data-layers can be used for plant-volume calculations and application of vegetation indices (VI) on the object-level. A randomized agro-ecological field experiment by Barel et al. (2018) is used to validate results from spectral and geometric object analysis. They assess legacy effects of preceding crops via the soil, known as plant-soil feedback (PSF), by destructive sampling and qualifying *cichorium* plant traits such as biomass. Four different cover crop species and their mixtures are used as a plant-soil treatment: *Lolium perenne* (perennial ryegrass), *raphanus sativus* (radish), *trifolium repens* (white clover), and *vicia sativa* (common vetch). Optical and hyperspectral UAV-data was acquired prior to destructive sampling. OBIA shows comparable results. The *raphanus* monoculture and mixture *raphanus* + *vicia* cause highest plant-volumes and high scores for most VIs used. The *lolium* treatment has overall the lowest average crop volume and VI scores.

## ACKNOWLEDGEMENTS

Thanks to my supervisor Dr. Lammert Kooistra of Wageningen University and Research. Lammert introduced me to UAV-remote sensing and its application in the field of agriculture. His enthusiasm and concern about the subject, together with the constructive feedback sessions we had, motivated me to reach this final point. The thesis research project enhanced my enthusiasm about remote sensing in general, the application of UAVs, precision agriculture, and the broad discipline of ecology. Special thanks to Dr. Gerlinde de Deyn who introduced me to the relevant biological background theories and mechanisms. She was always available for further questions about the field measurements and her input helped me with the interpretation of the final results.

# CONTENTS

1	INTRODUCTION .....	1
2	RESEARCH IN CONTEXT .....	3
2.1	UAV-Remote Sensing.....	3
2.2	Object-Based Image Analysis .....	3
2.3	Precision agriculture.....	4
3	RESEARCH OBJECTIVES .....	5
4	RESEARCH SCOPE .....	6
5	THEORETICAL FRAMEWORK .....	7
5.1	Remote Sensing in agriculture .....	7
5.2	Plant-soil Feedback concept.....	8
5.3	Object-Based Image Analysis and Template matching .....	10
5.4	Spectral analysis .....	14
6	STUDY AREA AND DATA.....	17
6.1	Study Area.....	17
6.2	Sensors used .....	18
6.3	Data description.....	18
7	PRE-PROCESSING.....	19
7.1	Image rectification.....	19
7.2	Crop Surface Model .....	20
7.3	Creating Plots .....	22
8	METHODOLOGIES.....	23
8.1	OBIA applied .....	23
8.2	Template Matching .....	25
8.3	Integration of OBIA and TM .....	28
8.4	Visualization, statistics and interpretation.....	30
9	RESULTS .....	31
9.1	OBIA .....	31

9.2	Template Matching .....	32
9.3	Integration of OBIA and TM .....	33
9.4	Spectral analysis .....	34
9.5	Geometric analysis .....	37
10	DISCUSSION.....	39
10.1	OBIA .....	39
10.2	Data fusion .....	40
10.3	Plant dimensions based on DSM.....	41
10.4	Biochemical plant traits based on HSD.....	42
10.5	Plant-soil treatment’s legacies.....	42
10.6	Scalability.....	43
11	CONCLUSION.....	45
12	RECOMMENDATIONS .....	47
11	BIBLIOGRAPHY .....	49
12	APPENDICES .....	57



# LIST OF TABLES

TABLE 5.1 COMPARISON OF THE DIFFERENT RS PLATFORMS

TABLE 5.2 VEGETATION INDICES EVALUATED IN THIS STUDY

TABLE 6.1 DATASETS AND SPECIFICATIONS

TABLE 8.1 ANALYSIS STEPS AND RELEVANT SOFTWARE PACKAGES

TABLE 8.2 TESTED VALUES MIRS PER PARAMETER

TABLE 8.3 INITIAL SAMPLE TEMPLATES

TABLE 8.4 TESTED VALUES TEMPLATE MATCHING PER PARAMETERS

TABLE 8.5 A DESCRIPTION OF TPs, FPs, FNs AND TNs

TABLE 9.1 RESULTS OF TM AND THE COMBINATION WITH OBIA

TABLE 9.2 OVERVIEW OF ALL PLANT-SOIL TREATMENTS INCLUDING A CONCLUSION BASED ON THE SPECTRAL ANALYSIS

TABLE 9.3 OVERVIEW OF ALL PLANT-SOIL TREATMENTS INCLUDING A CONCLUSION BASED ON THE GEOMETRIC ANALYSIS

# LIST OF FIGURES

FIGURE 5.1 INFLUENCED CROP VOLUME BY PLANT-SOIL FEEDBACK MECHANISMS

FIGURE 5.2 FLOWCHART OF OBIA-BASED OBJECT GENERATION

FIGURE 5.3 MIRS WORK FLOW DIAGRAM

FIGURE 5.4 SEGMENT MEAN SHIFT EXPLAINED

FIGURE 5.5 FLOWCHART OF TM-BASED OBJECT DETECTION

FIGURE 5.6 SPECTRAL BANDS IN THE VISIBLE SPECTRUM

FIGURE 6.1 OVERVIEW OF THE STUDY AREA BASED ON THE RGB IMAGERY

FIGURE 7.1 COMBINATION OF THE RGB ORTHOPHOTO, THE RECEIVED HSD AND NEW HSD; WITH THE HSD SHOWN WITH 50% TRANSPARENCY

FIGURE 7.2 OVERVIEW OF THE DSM, DTM AND CSM

FIGURE 7.3 PLOT 105, 106 AND 108 WITH INCORRECT CROP HEIGHT VALUES DISPLAYED ON THE CSM

FIGURE 7.4 CREATING PLOT-OBJECTS BASED ON OBIA OUTPUT

FIGURE 8.1 GENERATED TEMPLATE

FIGURE 8.2 WORKFLOW OF THE OBIA AND TM INTEGRATION

FIGURE 8.3 THE CSM AND HSD COMBINED WITH A CROP-OBJECT

FIGURE 9.1 SEGMENTS CREATED BY MIRS FOR ONE OF THE PLOTS WITHIN THE EXPERIMENTAL FIELD

FIGURE 9.2 MATCHES WITH TM FOR PART OF THE EXPERIMENTAL FIELD

FIGURE 9.3 RESULTS OBIA AND TM COMBINED FOR ONE OF THE PLOTS WITHIN THE EXPERIMENTAL FIELD

FIGURE 9.4 THE SPECTRAL SIGNATURES OF CICHORIUM GROWN IN DIFFERENT EXPERIMENTAL PLOTS WITH ASSOCIATED TREATMENTS

FIGURE 9.5 THE SPECTRAL SIGNATURES OF CICHORIUM GROWN IN DIFFERENT EXPERIMENTAL PLOTS WITH ASSOCIATED TREATMENTS, ZOOMED-IN ON THE VISIBLE AND NEAR-INFRARED PART OF THE SPECTRUM

FIGURE 9.6 THE AVERAGE VEGETATION INDEX VALUES OF CICHORIUM GROWN IN DIFFERENT EXPERIMENTAL PLOTS WITH ASSOCIATED TREATMENTS.

FIGURE 9.7 AVERAGE PLANT-VOLUME (SQ CM) INCLUDING 95% CONFIDENCE INTERVAL

# LIST OF APPENDICES

I DSM > DTM > CSM

II SEGMENTATION TEST LAYER WEIGHT VALUES.

III SEGMENTATION TEST SCALE-FACTORS

IV SEGMENTATION TEST SHAPE FACTORS

V SEGMENTATION TEST COMPACTNESS FACTORS

VI VEGETATION INDICES APPLIED ON RGB IMAGE

VII CLASSIFICATION BASED ON TGI VEGETATION INDEX

VIII TEMPLATE GENERATION

IX OBIA VECTOR-OBJECTS

X TM POINT-FEATURES

XI POINT-FEATURES RESULTING FROM TM AND OBIA

XII ARCMAP-WORKFLOW FOR CREATING AOIS

XIII ARCMAP-WORKFLOW FOR ADDING ATTRIBUTES TO OBJECTS AND POINT-FEATURES

XIV PYTHON SCRIPT SPECTRAL SIGNATURES

XV PYTHON SCRIPT VEGETATION INDICES

XVI PYTHON SCRIPT VOLUME PLOTS

XVII PYTHON SCRIPT CORRELATION

XVIII VEGETATION INDICES APPLIED PER TREATMENT

XIX EXPLORATION CORRELATION VOLUME AND SHOOT BIOMASS

XX AVERAGE CROP VOLUME (SQ CM) FOR EACH PLOT

## LIST OF ABBREVIATIONS AND ACRONYMS

AGT:	Adaptive Gaussian thresholding
ANOVA:	Analysis of Variance
C:	Carbon
Chl:	Chlorophyll
CI:	Chlorophyll Index
CSM:	Crop Surface Model
CVI:	Chlorophyll Vegetation Index
DAP:	Digital Aerial Photogrammetry
DSM:	Digital Surface Model
NDVI:	Normalized Difference Vegetation Index
GCP:	Ground Control Point
GIS:	Geographical Information System
GPS:	Global Positioning System
HSD:	Hyperspectral Datacube
HYMSY:	Hyperspectral Mapping System
IMU:	Inertial measurement unit
LAI:	Leaf Area Index
LCC:	Leaf Chlorophyll Content
LiDAR:	Light Detection and Ranging
MCARI:	Modified Chlorophyll Absorption in Reflectance Index
MRIS:	Multi Resolution Image Segmentation
MTCI:	MERIS Terrestrial Chlorophyll Index
MTVI:	Modified Triangular Vegetation Index
N <sub>2</sub> :	Nitrogen
NIR:	Near-Infrared Region
OBIA:	Object-Based Analysis
OSAVI:	Optimized Soil Adjusted Vegetation Indices

PSF:	Plant-soil Feedback
REP:	Red Edge Position
RGB:	Red, Green, Blue
RMSE:	Root Means Square Error
RP:	Reference Point
RS:	Remote Sensing
TCARI:	Transformed Chlorophyll Absorption in Reflectance Index
TM:	Template Matching
TV:	Threshold Value
UAV:	Unmanned Aerial Vehicle
VHR:	Very High Resolution
VI:	Vegetation Index
VIS:	Visible light



# 1 INTRODUCTION

According to *World Population Prospects: The 2017 Revision*, the current world population of 7.6 billion is expected to reach 8.6 billion in 2030, 9.8 billion in 2050, and 11.2 billion in 2100 (United Nations Department of Economic and Social Affairs 2017). The population growth is expected to continue with roughly 83 million people being added every year, even taking a declining fertility level into account. This asks for massive increase in agricultural yield and massive decrease in the use of fossil fuels and water. Hunger could be the most urgent problem of the 21<sup>st</sup> century. The Netherlands, with a size of 41,543 km<sup>2</sup> and over 17 million inhabitants, is the second largest global exporter of food (91.7 billion euros) after the United States, this creates optimism in respect to world's urgent environmental and food security problems (CBS 2017; World Bank 2018). There is a desperate need for more innovative solutions within the agricultural sector and spread of agricultural innovations throughout the world.

There are roughly two types of agriculture: on the one hand high-throughput or conventional agriculture and on the other hand low-throughput or organic agriculture. The fundamental qualitative and quantitative differences are in the flow of nutrients. High-throughput agriculture depends on large-scale use of synthetic fertilizers and pesticides. Low-throughput agriculture depends on the application of compost and manure, and the use of cover crops (Clark et al. 1976).

Low-throughput agriculture depends on accurate and in-season information on the crop-level to make better management decisions according to the farm inputs, necessitating the rise of precision agriculture. Yet there are other motivations for precision agriculture: yield enhancement, management strategy improvement, financial cost reduction, scientific interest, and breakthrough of digital agriculture technologies. The following definition is used for precision agriculture:

*“Precision agriculture generally involves better management of farm inputs such as fertilisers, herbicides, seed, fuel (used during tillage, planting, spraying, etc.) by doing the right management practice at the right place and the right time”* (Mulla 2013, p. 358).

Precision agriculture started in the 80's with ground sensors for measuring soil matter. Afterwards agricultural remote sensing platforms included satellites, airplanes handhelds, and tractors. Today, advanced sensor technologies are used such as light detection and ranging (LiDAR), fluorescence-, thermal-, optical-, and near-infrared spectroscopy (Mulla 2013).

Remote sensing (RS) with unmanned aerial vehicles (UAV) has potential for low-throughput and precision agriculture. UAVs have specific capabilities making them different from satellite and airborne platforms. First, UAVs have a very high spatial resolution which enables characterization of plant traits related to shape and dimensions (Feng, Liu, and Gong 2015). Second, digital surface models (DSMs) can be derived automatically which could provide more accurate estimations of crop height and volume (Suomalainen et al. 2014). Third, the spectral resolution of UAVs is higher,

resulting in more and narrower spectral bands. Fourth, they are capable of delivering flexible in-time information (Andújar et al. 2016). Fifth, UAVs are advantageous because they are a relatively cheap solution and the images are unaffected by clouds due to low flying altitude (Andújar et al. 2016).

However, methods and applications that make use of these advantages need to be further developed and scientifically tested. Specifically, state-of-the-art Object-Based Image Analysis (OBIA) methods and techniques require further research to be able to take advantage of the very high spatial resolution (VHR) of the UAV-based data sources. OBIA allows for the observation and analyzation of variations in textural, contextual, and morphological object-features (Castillejo-González et al. 2009). Crop-level analysis could provide more information about crop's shape and dimensions (e.g. height, volume, and biomass). Data fusion with hyperspectral data could also provide biochemical characteristics on the individual crop-level.

In a recent experiment by Barel et al. (2018), the legacy effects of diversity in space and time driven by preceding crop biomass and soil nitrogen concentration on successive crops (i.e. *cichorium* and *Aaena*) is analysed. Quantitative laboratory measurements show a significant influence of preceding crops on the successor's quantity and quality. The key-concept is plant-soil feedback (PSF) and it describes reciprocal interactions between plants and soil biota. To understand and monitor these PSF effects, detailed characterization and monitoring of crop traits is a pre-requisite. Laboratory measurements to quantify crop traits is labour intensive and time consuming; this creates a bottleneck for precision agriculture in general. Our research attempts to achieve the same results as the field experiment by using VHR UAV-images, hyperspectral data, height data, and OBIA-methods.



## 2 RESEARCH IN CONTEXT

The investigated methodology could be used for deriving plant traits during the growing season as an input for precision agriculture. Yield could increase while the use of fertilizers and herbicides decreases. Information and knowledge about plant-soil feedback could improve expansion of low-throughput agriculture. Moreover, societal and scientific relevance is high. The growing world population demands an increase of yield in agriculture and a decrease of the use of water, chemicals, and raw materials. Multiple gaps in literature are present. Little is known about the effects of plant-soil feedback on plant traits (Putten et al. 2013). Moreover, little is written about the use of OBIA methods and techniques with VHR UAV-imagery and data fusion with hyperspectral images.

### 2.1 UAV-REMOTE SENSING

Information about plants for precision agriculture is often acquired using RS technologies; this means non-contact measurements of light emittance, reflectance, transmittance, and absorption (Mulla 2013). Plant traits are particularly measured from the canopy-level (Kooistra and Clevers 2016). Today, UAV-RS is an active field of study and has potential for the retrieval of crop characteristics and precision agriculture. The key advantage of UAV-RS is that data acquisition is cheaper due to lower technological and operational costs compared to other RS platforms (Vastaranta et al. 2014). Reasons for the growth of UAV-usage in RS are: (1) improved UAV airframes, (2) development of small, high-quality, and low-cost sensors, and (3) increased computer processing capacity and improved 3D imaging software (Colomina and Molina 2014)

The combination of UAV-RS and precision agriculture is a new and promising field of research. It has high potential for real-life applications. The possibility to acquire VHR-imagery at low altitudes (Feng, Liu, and Gong 2015), high spectral resolution, and automatic creation of DSMs (Suomalainen et al. 2014) are most important advantages of UAVs in respect to this research. This allows for more accurate estimations of plant traits, dimensions, and biomass.

### 2.2 OBJECT-BASED IMAGE ANALYSIS

Computer-based image processing techniques are currently used in different sectors, like the food and smartphone industries. Back in the 90s the food industry was one of the largest industries where image processing techniques were applied (Gunasekaran 1996). These technologies enabled a relatively recent paradigm shift in RS image analysis during the last twenty years. From a predominantly pixel-based model, we are moving towards an object-based contextual model which adapts the way humans interpret imagery (Hay and Castilla 2008). Image segmentation is one of the earliest methods for building image-objects, which dates back to the '70s. OBIA started to build

a critical bridge between the raster domain of RS and the primarily vector-domain of Geographical Information Systems (GIS) (Blaschke 2010).

*“Geographic Object-Based Image Analysis is a sub discipline of Geographic Information Science devoted to developing automated methods to partition Remote Sensing imagery into meaningful image-objects, and assessing their characteristics through spatial, spectral and temporal scales, so as to generate new geographic information in GIS-ready format” (Hay and Castilla 2008, p. 77).*

The definition of Hay and Castilla (2008) is taken as the leading definition for OBIA. This definition focusses on the bridge between RS and GIS. It emphasizes on automated methods for partitioning RS-imagery and the use of image-objects as the basic spatial-unit for further analysis on spatial, spectral, and temporal scale. Research has proven that OBIA gives a much higher accuracy than a pixel-based approach in thematic mapping, as for a coal fire area in Inner Mongolia (Yan et al. 2006) or a mixed urban-suburban-agricultural landscape in Pennsylvania (Platt and Rapoza 2008).

OBIA techniques are promising in relation with crop discrimination via RS. Conventional RS methods based on spectral pixel information lack the possibility to observe variations from textural, contextual, and morphological features (Castillejo-González et al. 2009). Using OBIA, adjacent pixels could be merged into spatially and spectrally homogeneous objects via segmentation and classification processes (Castillejo-González et al. 2009). No research is found which applies OBIA on the crop-level for deriving shape, plant dimensions, and biochemical characteristics. It is perceived that by using OBIA, estimated plant traits on the crop-level will be more accurate over using common pixel-to-pixel analysis.

## 2.3 PRECISION AGRICULTURE

Precision agriculture, as explained by the definition of Mulla (2013), is useful for low-throughput agriculture as well as high-throughput agriculture. A simpler and wider definition is given by Dixon and McCann (1997): “a management strategy that uses information technology to bring data from multiple sources to bear on decisions associated with crop production”. Some authors like Wang et al. (2006) emphasise more on the improvement of crop productivity while others like Mulla et al. (2002) and Tian (2002) emphasise more on the improvement of environmental quality because of the reduced use of fertilizers and pesticides.

Precision agriculture started in the 80’s with remote sensors for soil matter and progressed through many stages from then on. It moved to more site-specific crop management, based on management-zones and sampling methods. Currently, precision agriculture is inseparable related to spatial-temporal information collection, analysis, and management.

# 3 RESEARCH OBJECTIVES

The general objective is the development and evaluation of a methodology to measure plant traits and crop legacies based on VHR-imagery taken by UAVs. The following question is formulated to reach the research objectives:

*To what extent could legacy of plant-soil treatments be identified, using VHR optical UAV-imagery incorporating OBIA methods and techniques; considering plant dimensions, biomass, and biochemical plant traits?*

The objectives that should be reached in order to elaborate on the research problem are described by the following sub-questions:

- *To what extent can individual cichorium crops be identified using OBIA?*
- *To what extent can other data-layers as hyperspectral imagery and a DSM be combined with OBIA?*
- *To what extent can plant dimensions and biomass be defined using the orthorectified image, DSM, and crop-objects?*
- *To what extent can biochemical plant traits be defined using hyperspectral imagery and crop-objects?*
- *To what extent are legacies of plant-soil treatments observable in the measured plant traits?*
- *To what extent is the methodology used scalable?*

A first step is investigating to which extent crop-objects could be identified and classified. This is crucial for determining plant dimensions. A second step is investigating how well additional spatial data can be combined with OBIA-objects. Combining the objects with a DSM could give more insights on plant shape, dimensions, and biomass. Combining the objects with hyperspectral imagery could give more information about biochemical plant traits. Results could describe to what extent plant-soil treatments' legacies are observable. The discussion deals with the scalability of the investigated methodology.

# 4 RESEARCH SCOPE

Related research has been done by Meij et al. (2017) based on the data of Barel et al. (2018). They prove that plant traits and crop legacies can be well approached by UAV-based optical sensors. Our research has major differences compared to Meij et al. (2017). They focus on the crop species *avena sativa* (oats) instead of *cichorium endivia* (endive), use traditional pixel-to-pixel analysis methods and focus more on finding correlation between in-situ measurements and vegetation indices. *Cichorium* is a much smaller crop and is suitable for applying OBIA methods. This leads to information on plant dimensions and possibly higher accuracies concerning biochemical plant traits. Only measurements of *cichorium*'s root and shoot biomass are available. To be able to investigate results and patterns concerning plant-soil feedback, this research project depends on a comparison with earlier founded patterns by Barel et al. (2018).

## **What is NOT included in the research project?**

- A full description of image data; descriptions can be found in Meij et al. (2017).
- The creation of an orthophoto and DSM; methods and procedures used can be found in Suomalainen et al. (2014).
- Sensor systems sensitive to other parts of electromagnetic spectrum than the visible and near-infrared regions.
- Images derived by satellites, aircrafts or fixed-wing UAVs.
- Further elaboration on phenotyping and the potential of UAV-RS for this discipline.
- Own field measurements; descriptions can be found in Barel et al. (2018).
- Computing time and other relevant challenges like extensive visualization, large data volumes and data redundancy.
- A temporal aspect; the growth of the crops through time cannot be analysed or evaluated.
- A comparison of different software packages and libraries.

# 5 THEORETICAL FRAMEWORK

## 5.1 REMOTE SENSING IN AGRICULTURE

Remote sensing (RS) is “the science of deriving information about an object without actually coming in contact with it” (Campbell and Wynne 2011). RS can be active (energy source: the RS platform) or passive (energy source: the sun). A sensor mounted to a platform measures the incoming radiation from a target object. The amount of incoming radiation depends on the amount of energy emitted by the energy source and energy transmitted, absorbed, and reflected by particles in the atmosphere, earth’s surface, and target-object. Traditional RS platforms are satellites and piloted aircrafts. Mostly, these do not have the suitable spatial and temporal resolutions for measuring plant traits on the plot or individual crop-level and real-time analysis. UAVs are relatively easy-to-use, flexible in terms of operability, affordable, and have a high resolution. A concise comparison of the RS platforms is given in table 5.1.

**TABLE 5.1 COMPARISON OF THE DIFFERENT RS PLATFORMS (SOURCE: CANDIAGO ET AL. 2015)**

	<b>Spatial resolution</b>	<b>Operability</b>	<b>Field of view</b>	<b>Usability</b>	<b>Maximum weight sensors</b>	<b>Cost data acquisition</b>
UAV	0.5 – 10 cm	Flexible	50 – 500 m	Easy	Limited	Low
Helicopter	5 – 50 cm	Moderate	0.2 – 2 km	Pilot needed	Almost unlimited	Medium
Airborne	0.1 – 2 cm	Moderate	0.5 – 5 km	Pilot needed	Unlimited	High
Satellite	1 – 25 m	Limited	10 – 50 km	N/A	N/A	Very high

UAV-platforms with imaging, ranging, and positioning sensors could offer excellent possibilities for precision agriculture (Guo, Kujirai, and Watanabe 2012), forestry management (Ouédraogo et al. 2014), and geosciences (Westoby et al. 2012). Usage of UAVs depends on the technological development of three different systems: airframes, sensors, and 3D imaging software. Two major airframe types, rotary and fixed-wing, are available within a price range of €600 - € 100,000. Capabilities such as battery range, payload capacity, and completely autonomous flights are improving as technology continuous to develop (Nex and Remondino 2014). Considering the UAVs limited payload capacity, the sensor’s size and weight is a limiting factor. Sensor development follows the same path as everyday smart-phone cameras. Smaller low-cost sensors with improved spatial and spectral resolutions are developed continuously. At last, improving 3D imaging software enables automated and improved generation of geo-referenced orthophotos and DSMs (Colomina and Molina 2014).

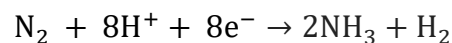
Today, it is possible to acquire VHR-imagery with UAVs at low altitudes (Feng, Liu, and Gong 2015), unaffected by clouds, relatively cheap, and in-time (Andújar et al. 2016). Mulla (2013) states that for precision agriculture a spatial resolution of at least 10 meters is needed for site-specific management, which makes UAV-RS promising for precision agriculture. Furthermore, with

relative cheap flights on a regular and flexible basis, farmers can make reliable decisions, save time and money, and potentially increase their productivity while applying low-throughput agriculture (Candiago et al. 2015).

## 5.2 PLANT-SOIL FEEDBACK CONCEPT

Plant-soil feedback (PSF) describes the reciprocal interactions between plants and soil biota. This mechanism may explain species invasion, maintenance of diversity through plant coexistence, and plant diversity-productivity relations (Cortois et al. 2016). Plant-soil feedback is important to understand in relation to low-throughput agriculture (Cortois et al. 2016). Specific preceding crops can have a positive or negative influence on the biomass of the succeeding crops. Winter crops could influence crop productivity, nitrogen (N) concentration, soil organic matter content, and soil mineral content (Barel et al. 2018). Recent decades have shown a growing scientific interest in PSF, though large-scale field studies are needed to evaluate the role of PSF processes under field conditions (Kulmatiski et al. 2008; Putten et al. 2013).

An important process carried out naturally in the soil is nitrogen (N<sub>2</sub>) fixation. The importance of N<sub>2</sub> fixation for low-throughput agriculture systems has been extensively reviewed (Ledgard 2001). There is a strong positive effect of a winter crop's biomass and N-concentration on the biomass of succeeding crops. Some of the N-fixating bacteria have a symbiotic relationship with certain plant species such as legumes. Some plants such as rice have a looser relationship with those bacteria. Atmospheric N<sub>2</sub> is converted to ammonia (NH<sub>3</sub>) by the enzyme nitrogenase (Postgate 1998):

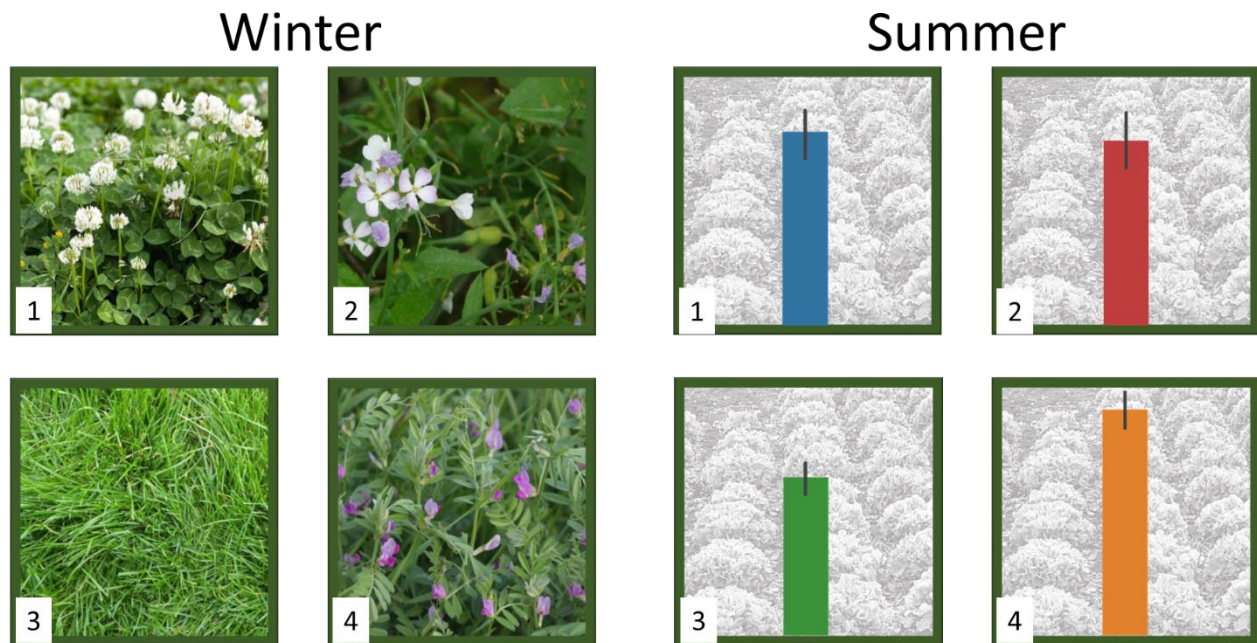


Soil biota describes all organisms that spend a significant part of their life within soil, such as earthworms, fungi, and bacteria. The composition of the soil's biota influences the growth of plant species, but its effect-size and direction differ for different plant species. For graminoids, which are herbaceous plants with a grass-like morphology, and early-successional plant species, a predominantly negative plant-soil feedback is found. This is likely due to a build-up of host-specific pathogens (Cortois et al. 2016). Late-successional plant species have a more positive plant-soil feedback as they are slower growing and benefit more from arbuscular mycorrhizal fungi (AMF) colonization. AMF colonization is a form of mycorrhiza; fungus penetrates the cortical cells of the roots of a vascular plant (Heinze et al. 2015).

Plants have an ability to insulate N for longer time periods than most microorganisms. For short timescales microorganisms compete better for N, especially NH<sub>4</sub><sup>+</sup>. Over the long-term plants will win: microorganisms will turn over N much faster than plants' roots. N will become available again in the soil, whereby plants are able to retain more N. This turnover point is when the C:N ratio is reached; the higher this ratio, the less N is needed per unit C. On the contrary, when N is scarce,

bacteria and fungi will grow on the available C of organic material and deduct soil-N, so N is temporally not available to the plants' roots (Hodge, Robinson, and Fitter 2000).

Barel et al. (2018) found that *lolium perenne*, which is an English winter ryegrass, does not increase the productivity of *cichorium* and reduced productivity of *avena*. It is expected that this is partly due to temporal limited availability of mineral N, caused by the described processes, and plant-feeding nematodes. Results could look similar to figure 5.1, where crop volume is relatively low for treatment 3 and relatively high for treatment 4. Barel et al. (2018) make use of destructive sampling which causes destruction of a small number of specimens within each plot. When generalizing destructive samples to the plot-level, irregularities within a plot could be missed. There is a need for the development of non-destructive sampling methods making use of RS. It enables to do research on PSF processes for larger areas and discards the need to destroy crops and to generalize from a limited number of samples. Biophysical molecules such as chlorophyll, are not always equally distributed over leaves and plants, so a non-destructive sampling approach could also be more accurate (Ciganda, Gitelson, and Schepers 2009).



**FIGURE 5.1 INFLUENCED CROP VOLUME BY PLANT-SOIL FEEDBACK MECHANISMS**

### 5.3 OBJECT-BASED IMAGE ANALYSIS AND TEMPLATE MATCHING

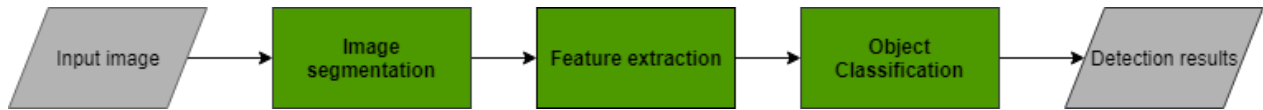
A relative recent paradigm shift in RS has taken place during the last twenty years, from a pixel-based model to an object-based contextual (Hay and Castilla 2008). The Machineseq program developed in 1984, was one of the first object detection techniques in RS. It could identify roads based on shape, size, and spectral information (Flanders, Hall-Beyer, and Pereverzoff 2003). Revolutionary software that strengthened the paradigm shift is eCognition, which was released in late 2000. The following main object detection approaches can be distinguished: 1) Template matching-based; 2) OBIA-based; 3) Knowledge-based; and 4) Machine learning-based (Cheng and Han 2016). Knowledge-based and machine learning-based will not be treated in this research but could be interesting in further research.

OBIA builds vector-objects based on raster data and starts to build a critical bridge between the raster-domain of RS and the primarily vector-domain of Geographical Information Systems (GIS) (Blaschke 2010). With OBIA meaningful multi-pixel objects can be created using spectral and spatial characteristics (Flanders, Hall-Beyer, and Pereverzoff 2003). Object variations like shape, size, and patterns can be derived from textural, contextual, and morphological features within the images. Conventional pixel-to-pixel approaches lack these capabilities and have difficulty with adequately exploiting contextual information or expert knowledge. It is hard to discriminate natural objects in especially heterogeneous areas with high spectral variability and mixed pixels. This makes making statements about object's dimensions cumbersome (Peña-Barragán et al. 2014). An OBIA approach is highly suitable or even mandatory for measuring individual plant dimensions as area, height, and volume,.

Castillejo-González et al. (2009) shows that the accuracy of thematic land-use mapping could increase by 22% when using OBIA over pixel-based analysis. Several studies confirm that OBIA can give much higher accuracies and enhance spectral separability compared to a pixel-based approach in thematic mapping (Yan et al. 2006, Platt and Rapoza 2008 Wang, Sousa, and Gong 2004; Peña et al. 2014; Verhoeff 2017; Peña-Barragána et al. 2012).

Segmentation and classification are fundamental parts of OBIA, as illustrated in figure 5.2. Segmentation is based on colour, texture, shape, and/or pixel-scale (Cheng and Han 2016). Segments are regions with homogeneity on one or more dimensions of a feature space (Blaschke 2010). Classification is based on rule-based decisions and fuzzy logic classifiers. After completion, an accuracy assessment that measures how well the objects are selected and classified compared to existing geographic objects is important (Cheng and Han 2016). From an algorithmic perspective, there are four categories of segmentation: point-based, edge-based, region-based, and combined (Blaschke, 2010).

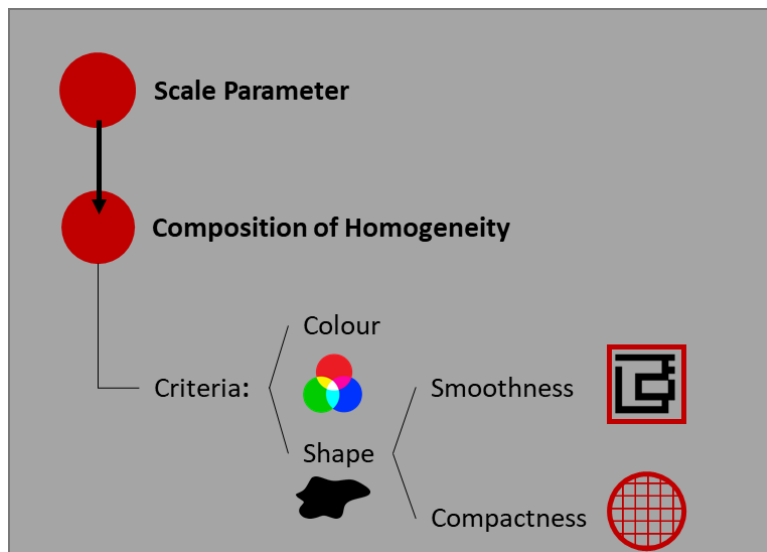




**FIGURE 5.2 FLOWCHART OF OBIA-BASED OBJECT GENERATION**

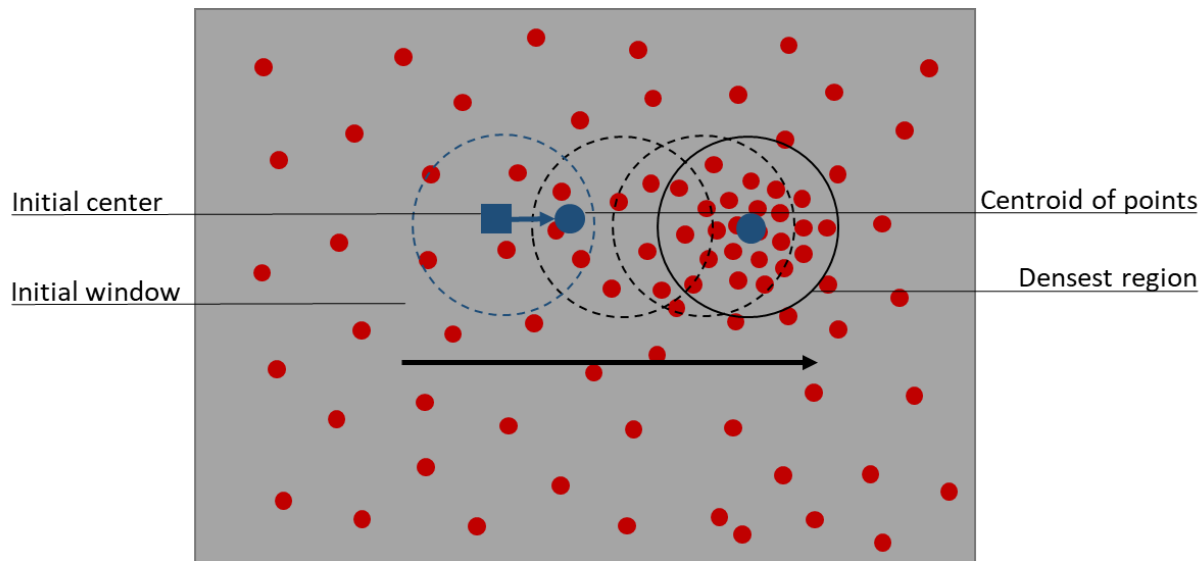
The multiresolution image segmentation (MIRS) algorithm is a patented algorithm included in eCognition. It is a region-growing segmentation algorithm that creates multi-pixel object primitives based on both spatial and spectral features (Flanders, Hall-Beyer, and Pereverzoff 2003). It takes individual pixels as a starting point and merges the most similar adjacent regions, considering a user-defined threshold (scale-factor) for the maximum internal heterogeneity. The algorithm creates a hierarchy of fine objects. Those fine objects can be aggregated to larger objects during a classification process based on their hierarchy (Benz et al. 2004). Image segmentation algorithms always deal with the following trade-off: averaging pixels over a larger area is needed to be certain about a pixel’s class, while this makes the location of the object’s boundaries less certain (Bhalerao 1995). MIRS can help overcome that problem by producing fine objects. It is hard to describe the algorithm in further detail as not all details are available.

The scale-factor of MIRS defines the maximum standard deviation of the homogeneity criteria, as shown in figure 5.3, while respecting the weights of the image layers. Defining the optimal scale-factor is not a standardized process. A large scale-factor results in large objects and vice versa (Wang, Sousa, and Gong 2004). Moreover, segmentation results also depend on data characteristics like the number of spectral bands, spatial resolution, image quantization, and scene characteristics (Stumpf and Kerle 2011).



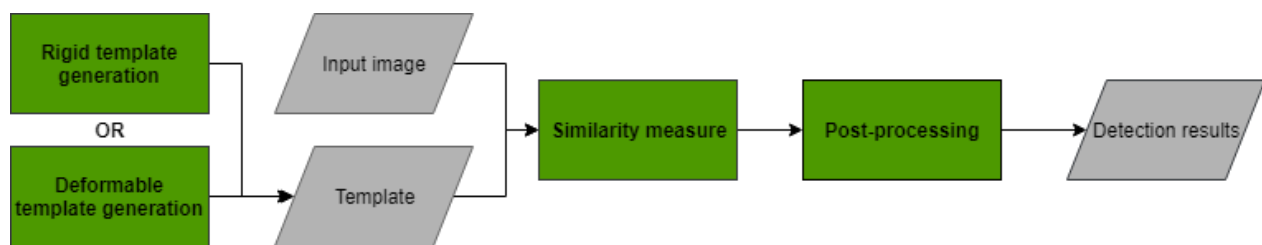
**FIGURE 5.3 MIRS WORK FLOW DIAGRAM**

Another segmentation method is segment mean shift, an unsupervised region-based segmentation algorithm that is included in the GIS software package ArcGIS. It uses a moving window with a certain bandwidth parameter. The algorithm seeks local maxima of density in the feature space. If the centre of a moving window matches with a centroid of points (local maxima of density), then the whole window is classified as a homogeneous vector-object. The steps of a moving window are larger within low-density regions and smaller in high-density regions (Tao, Jin, and Zhang 2007). This process is summarized in figure 5.4.



**FIGURE 5.4 SEGMENT MEAN SHIFT EXPLAINED**

Template Matching (TM) is a measure of similarity between a template and a feature within an image (Lewis 1995; Kalantar et al. 2017); it is one of the simplest and earliest approaches of object detection. An overview of TM is shown in figure 5.5. The first step is template generation, which can be hand-crafted or learned-based on a training dataset. The second step is a similarity measure, the template is positioned and compared in all different positions. There are two main TM categories: rigid-TM and deformable-TM. Rigid-TM is applicable on objects with small variations and a simple appearance (e.g. roads). The template must be precise. It is sensitive to shape and density variations (Cheng and Han 2016). Deformable-TM is introduced by Fischler and Elschlager (1970), it can deal with shape deformations and intra-class variations (Cheng and Han 2016).



**FIGURE 5.5 FLOWCHART OF TM-BASED OBJECT DETECTION**

Deformable-TM could roughly be divided in two classes: free-form deformable templates and parametric deformable templates. Free-form deformable templates take an arbitrary object shape with general constraints on aspects like continuity and smoothness. It is simple and easy to implement, but it is sensitive to change in shape and viewpoint, and is dependent on scale and rotation. Parametric deformable-templates use a formula to parameterize the object and its variations. It is powerful and flexible in dealing with the object's shape and intra-class variations. On the other hand, computations are extensive and prior information on the geometrical shape is required (Cheng and Han 2016). A relevant study on the detection of tree-crowns on medium resolution UAV-imagery is done by Hung, Bryson, and Sukkarieh (2012).

When building a template library for rigid-TM the following aspects should be taken in consideration: object's shape, template size, image's brightness, and shadow direction (Tiede et al. 2017). Rectangular shapes can have shadows on a single-side or two-sides. With round objects, shadow can only occur at a single-side. A template should cover the object including all shadow directions and parts of the surrounding area. At last, it is important to select objects at different locations, other weather conditions, solar azimuth angles, and time-scales (Tiede et al. 2017).

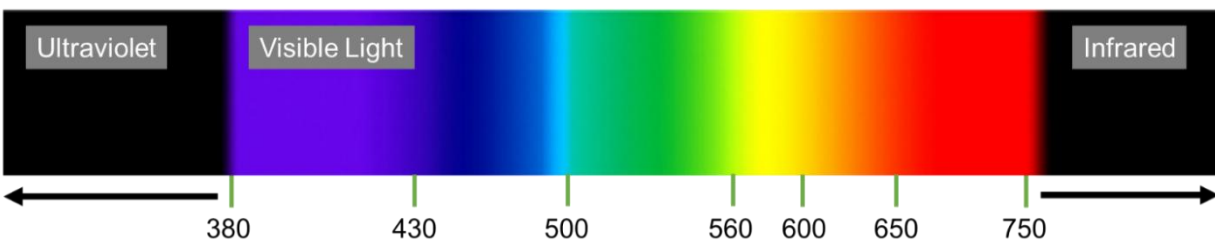
Verhoeff (2017) successfully applies rigid-TM. He uses Adaptive Gaussian thresholding (AGT), which uses a moving window with a user-defined window size and threshold value (TV). The TM algorithm implemented in eCognition uses normalized cross-correlation. Cross-correlation is a sophisticated recognition technique for detecting features. Cross-correlation normalizes both the template and image to unit length. It is a measure of similarity between two real-valued functions,  $f$  and  $g$ , incorporating a function of displacement ( $t$ ) relating to the functions  $f$  and  $g$ . Cross-correlation has a few drawbacks. Feature matching could fail if the energy displayed on an image is not constant, e.g. when there are bright spots. Furthermore, cross-correlation measurements are dependent on template's size and image amplitudes (Lewis 1995).

Cheng and Han (2016) show that OBIA methods and TM are generally handled separately. A typical problem of TM is a high number of false positives in more complex images. With generated OBIA-objects irrelevant areas can be excluded, this is so-called stratified TM (Tiede et al. 2017). A workflow, in which TM and OBIA are integrated, is recently found as a suitable and accurate method to detect a variety of objects within VHR images. Such objects are for example dwellings within refugee camps (Tiede et al. 2017) and oil palm trees (Kalantar et al. 2017).

## 5.4 SPECTRAL ANALYSIS

Processing, interpretation, and analysis of retrieved RS data is needed. The energy interacts with a target-object and is reflected over many wavelengths of the electromagnetic spectrum. The reflection over these wavelengths is shaped by distinct properties of the target-object (Campbell and Wynne 2011). Reflectance data within the visible (VIS) and near-infrared (NIR) regions of the electromagnetic spectrum is an effective source of information for: monitoring vegetation, quantifying biochemical and biophysical plant traits, and temporal monitoring of plant development (Candiago et al. 2015).

RS can give accurate approximations of biochemical aspects like chlorophyll for specific areas in the field (Franceschini et al. 2017). The amount of chlorophyll could give an estimation of the rate of photosynthesis and the crop's response on N application (van Evert et al. 2012). More important, chlorophyll is an import proxy for plant productivity in space and time (Houborg, Fisher, and Skidmore 2015). The reflectance in the NIR does mainly rely on leaf structure, and reflectance in the VIS mainly relies on leaf chlorophyll content (LCC) (Daughtry et al. 2000). Measurements in the red edge region show best results for predicting N. Both the green (550nm) and red edge (710nm) bands show a high correlation with chlorophyll (Kooistra and Clevers 2016). Figure 5.6 shows the VIS region of the electromagnetic spectrum, including the red edge and lowest part of the NIR region.



**FIGURE 5.6 SPECTRAL BANDS IN THE VISIBLE SPECTRUM**

The reflected light of plants has a characteristic spectral signature, which is affected by the morphology and physiology of the plant, and the open soil between canopies (Gates et al. 1965). Vegetation indices (VI) are appropriate for estimating plant traits. VIs are arithmetic calculations on the light reflected at different wavelengths. VIs vary in spectral wavelengths used for the calculations, have varying spectral resolutions (bandwidths), and use different arithmetic formulas (Rasmussen et al. 2016). The most common specializations of VIs are: LCC, above ground biomass, leaf area index (LAI), and N content (Rasmussen et al. 2016). Some are sensitive to LAI while insensitive to other aspects, like background and LCC (Kooistra and Clevers 2016).

The earliest and most commonly VIs used are based on spectral bands in the red and NIR region. Differences of reflectance within and between these regions is characteristic for dense green vegetation. The Normalized Difference Vegetation Index (NDVI) is the most common VI. It is the ratio of  $NIR - red$  over  $NIR + red$  (Tucker 1979). The red edge region between 680 and 780 nm

has proven to be a good measure for LLC, N, and LAI, with low sensitivity for canopy structure (Wu et al. 2008; Ciganda, Gitelson, and Schepers 2009; Clevers and Kooistra 2012; Franceschini et al. 2017). Common VIs in the red edge region are Red Edge Position (REP) (Cho et al. 2007; Clevers and Kooistra 2012), MERIS Terrestrial Chlorophyll Index (MTCI) (Dash and Curran 2004), MCARI (Haboudane et al. 2002), and red edge Chlorophyll Index (CI<sub>red edge</sub>) (Kooistra and Clevers 2016).

$$\text{NDVI} = \frac{\text{NIR} - \text{Red}}{\text{NIR} + \text{Red}}$$

Several VIs are specialized in measuring LCC. Few VIs show correlations with LAI, height, and N. According to Meij et al. (2017) only NDVI<sub>[735,750]</sub>, REP, and MTCI have, besides a strong correlation with LCC, a relatively high correlation with N content in *avena* crops. REP, MTCI, and MCARI/MTVI2 have the highest correlation with plant height. Correlation with LAI is limited. A VI for which LAI plays a relative large role (16.2% of the variation explained by LAI) is Chlorophyll Vegetation Index (CVI) (Kooistra and Clevers 2016). According to Kooistra and Clevers (2016) the CVI is also an effective VI for estimating LCC of potato plants. CVI requires bands in the green, red, and NIR range of the spectrum.

Franceschini et al. (2017) found that most VIs are overestimating LCC when used on UAV-imagery; red edge region VIs overestimate less. Red edge region VIs are considered to be the best predictors of LCC. Moreover, they show that MTCI has the best performance for the estimation of LCC for potato plants. An experiment with butterhead lettuce shows that red edge indices give better estimations on LCC compared to NDVI (Filella et al. 1995). Jones et al. (2007) shows that NDVI based on the red band 680 provided the best estimate of LCC for spinach plants.

Experiments of Clevers and Kooistra (2012) shows that especially the red edge variations of MCARI/OSAVI<sub>[705, 750]</sub> and TCARI/OSAVI<sub>[705,750]</sub> are the best indices for estimating LCC of potato plants.

The following red edge VIs are used: REP, MTCI, MCARI/OSAVI<sub>[705,750]</sub>, TCARI/OSAVI<sub>[705,750]</sub>, NDVI<sub>[735,750]</sub>, NDVI<sub>[720,820]</sub>, and CI<sub>red edge</sub>. Besides, the following regular VIs are used: NCVI<sub>[650,800]</sub>, MCARI/MTVI2, MCARI/OSAVI, TCARI/OSAVI, CVI, and CI<sub>green</sub>. The indices used are shown in table 5.2 including their formulas, sensitivities, and sources. Red and green coloured names represent the red edge and regular indices respectively.

**TABLE 5.2 VEGETATION INDICES EVALUATED IN THIS STUDY**

Vegetation Index	Formula	Sensitivity	Source
CI <sub>green</sub>	$\frac{R780}{R550} - 1$	LCC	Gritz, and Merzlyak (2003)
CVI	$\frac{R870}{R550} * \frac{R670}{R550}$	LCC and LAI	Vincini, Frazzi, and D'Alessio (2008); Kooistra and Clevers (2016)
MCARI / MTVI2	$\frac{(R700-R670-0.2(R700-R550)) \left(\frac{R700}{R670}\right)}{1.5(1.2(R800-R550)-2.5(R670-R550))}$ $\sqrt{2(R800 + 1)^2 - 6(R800-5\sqrt{R670})} - 0.5$	Height, N and LCC	Tian et al. (2011); Meij et al. (2017)
MCARI / OSAVI	$\frac{((R700 - R670) - 0.2(R700 - R550))(R700/R670)}{1.16(R800 - R670)/(R800 + R670 + 0.16)}$	LCC	Daughtry et al. (2000)
NDVI <sub>[650,800]</sub>	$\frac{R800 - R650}{R800 + R650}$	Overall condition canopy	(Tucker 1979)
TCARI / OSAVI	$\frac{3((R700 - R670) - 0.2(R700 - R550)) \left(\frac{R700}{R670}\right)}{1.16(R800 - R670)/(R750 + R670 + 0.16)}$	LCC	Haboudane et al. (2002)
CI <sub>red edge</sub>	$\frac{R780}{R710} - 1$	LCC	Gritz, and Merzlyak (2003)
MCARI / OSAVI <sub>red edge</sub>	$\frac{((R750 - R705) - 0.2(R750 - R550))(R750/R705)}{1.16(R750 - R705)/(R750 + R705 + 0.16)}$	LCC	Wu et al. (2008)
MTCI	$\frac{R755 - R710}{R710 - R680}$	Height, N LCC	Tian et al. (2011); Meij et al. (2017)
NDVI <sub>[735,750]</sub>	$\frac{R750 - R735}{R750 + R735}$	Height, N LCC	Meij et al. (2017)
NDVI <sub>[720,820]</sub>	$\frac{R820 - R720}{R820 + R720}$	Height, N LCC	Meij et al. (2017)
REP	$700 + 45 * \frac{Rre - R700}{R740 - R700} \quad Rre = \frac{R670 + R780}{2}$	Height, N and LCC	Cho et al. (2007); Meij et al. (2017)
TCARI / OSAVI <sub>red edge</sub>	$\frac{3((R750 - R705) - 0.2(R750 - R550)) \left(\frac{R750}{R705}\right)}{1.16(R750 - R705)/(R750 + R705 + 0.16)}$	LCC	Wu et al. (2008)



# 6 STUDY AREA AND DATA

## 6.1 STUDY AREA

The field experiment is established in 2015 to investigate the legacies of different monocultures and mixtures grown during winter on the succeeding summer crops: *avena sativa* (oats) and *cichorium endivia* (endive). *Lolium perenne* (perennial ryegrass), *raphanus sativus* (radish), *trifolium repens* (white clover), and *vicia sativa* (common vetch) monocultures and their mixtures *lolium* + *trifolium* and *raphanus* + *vicia* are the used winter crops. One of the plant-soil treatments is classified as *fallow*, which means that the plot did not receive a treatment. The acre is property of Wageningen UR, specific coordinates are: 51°59'41.72" N and 5°39'17.89" E using WGS-1984. The acre is divided in 120 plots of 3 × 3 m, of which 60 *cichorium* plots, each plot consists of two experimental units (1.5 × 3 m). Each crop rotation treatment is performed five times in a random order over the acre. Some plots accommodate two different mixtures, each within an own experimental unit (Barel et al. 2018).



FIGURE 6.1 OVERVIEW OF THE STUDY AREA BASED ON THE RGB IMAGERY

## 6.2 SENSORS USED

The lightweight hyperspectral mapping system (HYMSY) used has an ordinary camera with 16 megapixels (Panasonic GX1), a pushbroom spectrometer (PhotoFocus SM2-D1328 + Specim ImSpector V10 2/3), and an IMU-enhanced GPS sensor for calibration (XSens MTi-G-700) on board. The spectrometer has a spectral range of 400 to 950 nm, a spectral resolution of 10nm, a speed of 25 lines/second, and a spatial resolution of 328 pixels/line (Suomalainen et al. 2014). The HYMSY can create orthophotos at 1-5 cm resolution, DSMs at 5-10 cm resolution, and Hyperspectral Datacubes (HSD) at 10-50 cm resolution (Suomalainen et al. 2014).

Fresh biomass is recorded by clipping a small area per plot and weighing all above-ground vegetation. Dry biomass is derived by drying the fresh biomass in an oven of 70°C (Meij et al. 2017).

## 6.3 DATA DESCRIPTION

Four datasets are provided, the specifications of these datasets are summarized in table 6.1. All images are projected in UTM zone 31N using WGS-84 global datum. The DSM and orthophoto are derived from the RGB photos using Agisoft PhotoScan Pro and steps described by Suomalainen et al. (2014). The imagery is geometrically corrected and radiometrically calibrated according to the procedures of Suomalainen et al. (2014). Required additional pre-processing is described in chapter 7.

**TABLE 6.1 DATASETS AND SPECIFICATIONS**

<b>Dataset</b>	<b>Spatial resolution</b>	<b>Spectral resolution</b>	<b>Spectral range</b>
Orthophoto	1px = 1.5 cm	N.A.	RGB
Digital Surface Model (DSM)	1px = 2.9 cm	N.A.	RGB
Hyperspectral Datacube (HSD)	1px = 13.4 cm	5 nm	450-915 nm
Field Measurements	N.A.	N.A.	N.A.

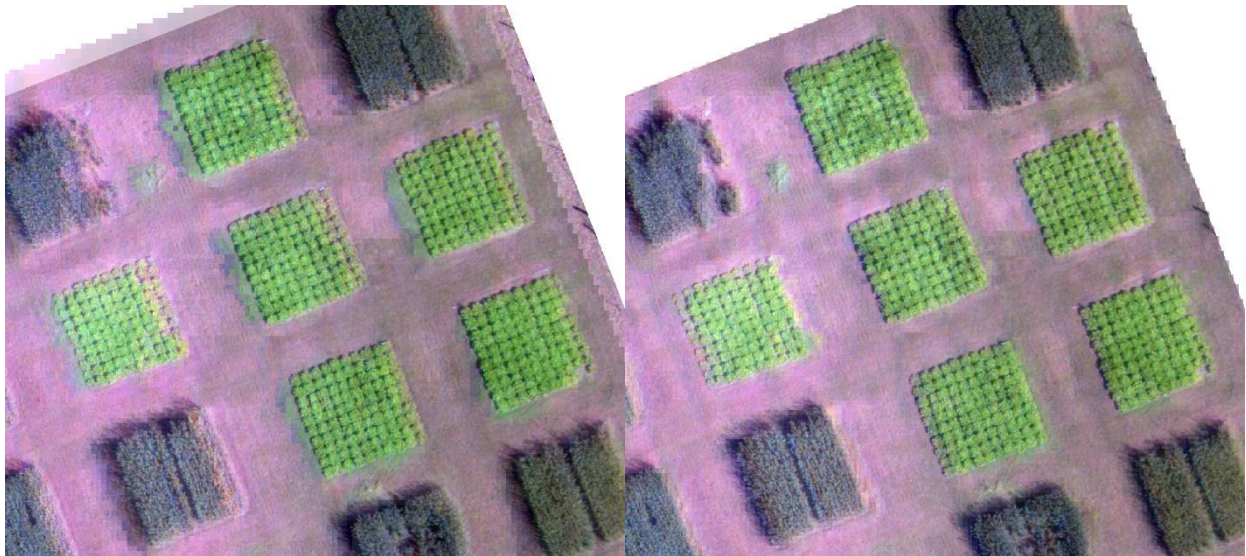
An HSD combines spatial and spectral dimensions in a three-dimensional Datacube.  $X$  and  $y$  represent the spatial dimension and  $\lambda$  the spectral dimension. It consists of a set of images all collected at a narrow spectral band positioned in the electromagnetic spectrum (McNamara et al. 2009). The images are divided into 94 adjacent bands with 5 nm intervals between 450 to 915 nm.



# 7 PRE-PROCESSING

## 7.1 IMAGE RECTIFICATION

To avoid including spectral data from non-crop pixels within crop-objects, OBIA requires strict alignment between image-objects based on the orthophoto and other data-layers. With pixel-to-pixel analysis, the negative effects of misalignment on the results could be averted by manually selecting samples away from crop-edges, as is done by Meij et al. (2017). Image rectification is a transformation process to project images with different alignment and proportions onto a common image plane. It allows merging images taken from different perspectives into a common projection system. Geometric distortions can occur in images, which can be caused by: misalignment, variability of the platform's attitude and altitude, lens distortions, and different viewing angles (Xiang and Tian 2011). The UAV used contains two separate sensors, an optical camera and a hyperspectral sensor, and therefore the risk of misalignment between the images (Suomalainen et al. 2014). Figure 7.1 (left) shows too much misalignment between the RGB image and the HSD. The HSDs for both flight lines are rectified. Its improved final alignment is shown in figure 7.1 (right).



**FIGURE 7.1 COMBINATION OF THE RGB ORTHOPHOTO, THE RECEIVED HSD (LEFT) AND NEW HSD (RIGHT); WITH THE HSD SHOWN WITH 50% TRANSPARENCY**

The spectral images of two flight lines are rectified using Hexagon Erdas Imagine software. Image rectification needs a reference layer with clearly recognizable objects. First ground control points (GCP) and reference points (RP) are selected equally distributed over both flight lines. Thereafter a polynomial transformation as described by Richards (2013) is applied to shift the HSD images. The RGB orthophoto could be used as a reference layer, but it is decided to use the OBIA crop-

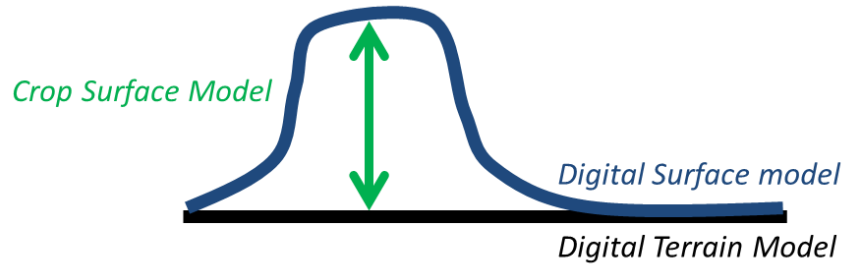
objects as described in paragraph 8.1 and 9.1. It makes it easier to distinguish plot and crop borders, as it displays the edges of plots and crops properly.

RPs are placed on the corners of *cichorium* plots. GCPs are placed on the HSD, which is an error-prone process as edges are not always displayed clearly. At first attempt, 10 GCPs were used for the resampling operation. Based on visual inspection, it is concluded that the resulting image still shows too much misalignment at some plots. It is decided to place RPs and GCPs on all suitable plots containing *cichorium*, which results in improved alignment. Flight line 1 contains 117 GCPs with a root mean square (RMS) error on the x-axis of 0.2105 (pixels) and 0.1872 on the y-axis. For flight line 2, 119 GCPs are placed resulting in an RMS error on the x-axis of 0.2090 and 0.1506 on the y-axis.

The higher the polynomial transformation order, the more complex distortions can be corrected. A higher order polynomial shift requires more calculation power and could cause more errors, but results are perceived to be more accurate (Richards, 2013). Polynomial shifts with an order up to 7 are executed, but results do not improve after the second order. A second order polynomial shift is applied to rectify the images. To determine and calculate new pixel reflectance values for the new shifted raster image, a resampling algorithm is used. The following three algorithms are most common: *nearest neighbourhood resampling*, *bilinear interpolation*, and *cubic convolution interpolation*. *Nearest neighbourhood* is often chosen for large images as it is least time consuming (Richards 2013). Experiments show that *bilinear* and *cubic convolution* show slightly better results. In our case the difference in calculation-time is negligible, and resampling is done based on *cubic convolution*. For more information on these techniques, see Richards (2013).

## 7.2 CROP SURFACE MODEL

The DSM contains height values of the top surface, in respect to a vertical coordinate system. A vertically coordinate system is based on an ellipsoid which is a mathematically defined surface that approximates the true figure of the earth or the geoid. The DSM's height values could represent both terrain and crops, or only crop height when actual terrain height is similar or lower than the ellipsoid. The DSM is created by digital aerial photogrammetry (DAP), with DAP it is not possible to look through vegetation to derive terrain heights, like LiDAR technology can (Vastaranta et al. 2014). A first step is deriving a digital terrain model (DTM) from the DSM. The second step is normalizing the DSM with the DTM to derive a model representing crop heights, a so-called crop surface model (CSM). Figure 7.2 shows an overview of the DSM, DTM, and normalized DSM (CSM).

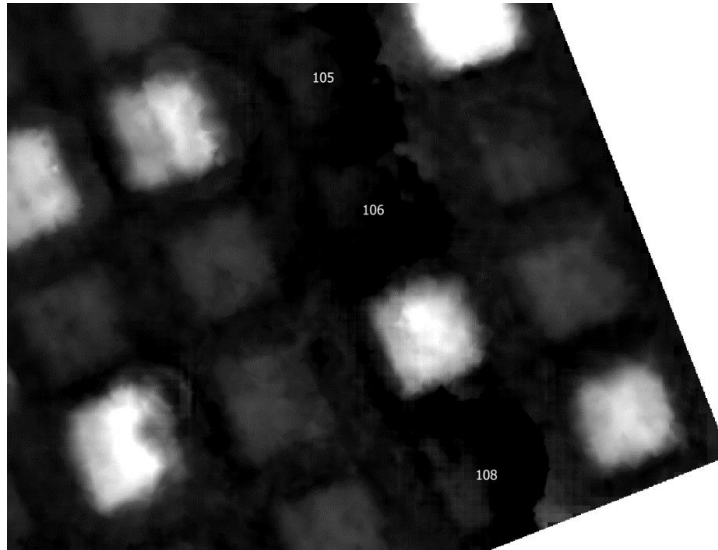


**FIGURE 7.2 OVERVIEW OF THE DSM, DTM AND CSM**

The DTM is created by interpolating the height values of areas between plots. Only if enough areas without vegetation cover are available in the image, can an accurate DTM be created (Goodbody et al. 2017). Higher areas are overrepresented within the DSM; objects do not have sharp edges and height values decrease smoothly away from the object. The plots in the field are erased from the DSM, including a 30-centimeter buffer to compensate for the explained phenomenon. Literature confirms that heights of objects are mainly underestimated at the edges and area-cover is overestimated when using height models created by DAP (Tilly et al. 2014).

The resulting raster is turned into a point cloud, containing 1,112,497 point-features. This point cloud is used to interpolate the final DTM. A random point sample is selected, containing 0.1 percent of all points, to enhance calculation speed of interpolation and to have more equally distributed points. Inverse distance weighted (IDW), Triangular Irregular Network (TIN), Kriging, and Natural Neighbour (NN) are the three most common interpolation techniques. The best linear unbiased estimates are provided with the Kriging technique while IDW is much quicker and simpler (Mueller et al. 2004). The NN method uses the same basic equation as IDW, is as efficient, and does not need user-specified parameters. The NN method is appropriate for point-features with an uneven distribution and density. It limits overshoots of local high values and undershoots of local low values (Boissonnat and Gazais 2002). The final DTM is created by NN because of those advantages.

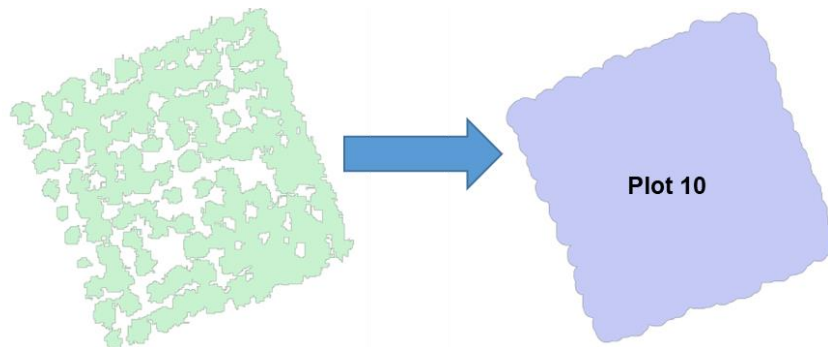
The mosaic-line within the orthophoto is distinguishable in the DSM. Along both sides of the mosaic-line height values can deviate. This has effect on the interpolation and results in incorrect crop height values around the mosaic-line, which are close to zero or negative. This is the case for plot 105, 106, and 108, as shown in figure 7.3. These plots are excluded in further geometric analysis.



**FIGURE 7.3 PLOT 105, 106 AND 108 WITH INCORRECT CROP HEIGHT VALUES DISPLAYED ON THE CSM**

### 7.3 CREATING PLOTS

Plot-objects, or so-called areas of interest (AOI), need to be created in order to relate image-objects to a certain experimental plot and treatment. Creating those plots is done according to a custom workflow in Esri Arcmap, as presented in appendix XII. OBIA crop-objects as described in paragraph 8.1 and 9.1 are a required input for the workflow. Most single crops are in fact represented by a larger object due to leaf overlap, as visible in figure 7.4. The workflow selects the largest objects based on a certain threshold ( $> 1 \text{ m}^2$ ) and these are taken as the basis for the plots. In some cases, individual *cichorium* crops are stored as single objects and are attached to the main plot. This is done by creating buffers of 10 centimetres around the largest objects and merging them with intersecting smaller objects. Finally, the created plot-objects are numbered and ready for further use. Figure 7.4 shows an example of input crop-objects and an output plot-object.



**FIGURE 7.4 CREATING PLOT-OBJECTS BASED ON OBIA OUTPUT**

# 8 METHODOLOGIES

This chapter describes the actions taken to investigate the research problem, including analysis steps and choices made. Consult chapter 7 for actions taken related to data pre-processing. The Object-Based Image Analysis exists of two parts, segmentation and classification, which are both executed in eCognition. Moreover, the TM process is described, which exists out of building a template library and applying a rigid-TM algorithm as described in paragraph 5.3. This chapter describes how TM and OBIA are combined, and how further spectral and geometrical analyses are executed and visualized. The goal is to find the most optimal settings for each processing step and to get the most accurate results possible. The analysis steps and software used are described in table 8.1.

**TABLE 8.1 ANALYSIS STEPS AND RELEVANT SOFTWARE PACKAGES**

Step	Activity	Software
1A	<b>Pre-processing:</b> Rectification HSD	<i>Erdas Imagine</i>
1B	<b>Pre-processing:</b> Interpolation and calculation CSM	<i>Arcmap</i>
2A	<b>OBIA:</b> Image segmentation and classification	<i>eCognition</i>
2B	<b>TM:</b> Generation template and execution matching	<i>eCognition</i>
3A	<b>Processing:</b> Creation AOI's (plots)	<i>Arcmap</i>
3B	<b>Processing:</b> Join geometric and hyperspectral attribute data on vector-objects	<i>Arcmap</i>
4A	<b>Geometric analysis:</b> Calculation volumes	<i>Arcmap, Python (Pandas and Scikit)</i>
4B	<b>Hyperspectral analysis:</b> Application vegetation indices	<i>Python (lib.: Pandas and Numpy)</i>
5	<b>Visualizations:</b> Plot statistics	<i>Python (lib.: Pandas and Seaborn)</i>

## 8.1 OBIA APPLIED

Prior to the research project, several segmentation methods and techniques included in available software programs and libraries were explored and assessed: those are *segment mean shift* included in *ArcGIS*, algorithms in *Orfeo Toolbox*, and *multi resolution image segmentation* included in *eCognition*. The *segment mean shift* algorithm is described in paragraph 5.3. Unfortunately, this algorithm cannot be described as a truth OBIA method. It produces a classified raster image instead of meaningful vector-objects; its main purpose is image classification. Individual crops could not be clearly distinguished. Alternatively, *Orfeo Toolbox* could be used which contains several segmentation algorithms: *segment mean shift*, *connected components* and *watershed segmentation*. eCognition's *multi-resolution image segmentation* (MIRS) algorithm gets most attention in previous research articles on image segmentation. Neubert et al. (2001) show that MIRS does best segmentation based on VHR imagery compared to several other segmentation algorithms. Different papers show excellent results for building image-objects with MIRS (Flanders, Hall-Beyer, and Pereverzoff 2003; Cheng and Han 2016). MIRS will be used and is further elaborated in this chapter. A further comparison of software packages and algorithms is not given.

The RGB image is used as input for MIRS. The available hyperspectral data and elevation data are considered as possible additional sources for segmentation, as it could enhance final segmentation results. Unfortunately, this is impossible due to too much difference in resolution between all data sets and too much geometric distortion within the hyperspectral data. Data fusion with raster data sets is only possible with adequate alignment between images. The following time-consuming OBIA related steps are taken: first, determine the right parameters for MIRS; second, define the rules for classification; third, manually check OBIA results with the plots or areas of interests (AOI).

The segmentation algorithm uses three parameters as described in paragraph 5.3 and shown by figure 5.4: the scale-factor, the weight of shape heterogeneity, and the weight of compactness. In addition to those parameters, the outcome of the segmentation depends on several other choices. The choices are related to the weight factors used for the spectral bands and classification rules. All settings and parameters are tested in isolation. In other words, when an individual parameter is tested, all other parameters are kept on default. It would be too complicated and time-consuming to test all combinations; using a programming language would allow more extensive testing, but *eCognition* does not allow this. A decision upon the most optimal parameter is made based on the visual results, those results are shown in the appendices.

The first test adjusts the weights of the individual spectral bands, according to the values in table 8.2. By default, the weights are equal. It is expected that increasing the weight value of the green band would have positive effects on the segmentation results as the green band shows most contrast between crop-covered areas and other land cover types. A higher weight for the green layer results in slightly more isolated crop-objects. Moreover, the shapes of resulting crop-objects differ slightly but they are not convincingly smaller or larger. It is decided to keep all band layer weights equal. A comparison of segmentation results using weight factors 1 and 20 for the green layer is shown in Appendix II.

**TABLE 8.2 TESTED VALUES MIRS PER PARAMETER**

Parameter	Values											
Scale-factor	1	5	10	15	20	25	30	35	40	45	50	
Shape	0.1	0.2	0.3	0.4	0.5	0.6	0.7	0.8	0.9			
Compactness	0.1	0.2	0.3	0.4	0.5	0.6	0.7	0.8	0.9			
VI (TGI) threshold value	10	15	20	25	30	35	36	37	38	39	40	45
Red band weight factor	1	2	3	5	10	15	20					
Green band weight factor	1	2	3	5	10	15	20					
Blue band weight factor	1											

The second test adjusts the scale-factor. This is a user-defined threshold value for the maximum internal heterogeneity within an object (Benz et al. 2004); a lower scale-factor results in smaller objects. With a low scale-factor (e.g. value 5) and thus small objects, the final classified objects look grainier. When using a scale-factor higher than 10, some non-crop areas between crops are wrongly classified as crops, thus enabling potential overestimation of *cichorium*-covered areas.

Images of this test are shown in Appendix III. The default scale-factor 10 is chosen for the final segmentation.

The third test increases the shape factor with steps of 0.1 between 0.1 and 0.9. The higher the value, the lower the influence of colour on the segmentation process. With the highest possible value of 0.9 some *cichorium* crops are missed. For the example plot shown in appendix IV there are five crop areas not detected as crop when using value 0.9. It is concluded that there are no significant improvements when increasing the default value of 0.1.

The fourth test adjusts the compactness value. It defines the weight of the compactness criterion, the higher the value the more compact image-objects may be. The default value is increased with steps of 0.1 between 0.1 and 0.9. The higher the compactness value the less protrusions are observed. Changes are minor and above 0.5 negligible, results are shown in appendix V.

For the classification of the objects three VIs suitable for RGB images are explored: an adjusted version of *NDVI* (Rabatel et al. 2011), *VARI* and *TGI* (Mckinnon and Hoff 2017). Appendix VI shows applications of the three VIs. *TGI* shows highest contrasts and *cichorium* is standing out more clearly. Moreover, edges of individual crops are shown more clearly with *TGI*. The formula is:

$$TGI = Green - 0.39 * Red - 0.6 * Blue$$

Small objects can be classified and merged to larger crop-objects based on a *TGI* value. The minimum *TGI* value or threshold value is found by trial-and-error. The most optimal threshold value found is 38. Appendix VII shows the classifications for values 37, 38 and 39. When using value 37 more open spots within the plots and areas outside the plots are classified as *cichorium* crops, which are so-called false positives. The amount of missed *cichorium* crops is low, so-called false negatives. When increasing the value to 38, there are more open areas within the plots while the classification still seems to cover the *cichorium* crops properly. With TV 39 some crops are completely missed in the classification.


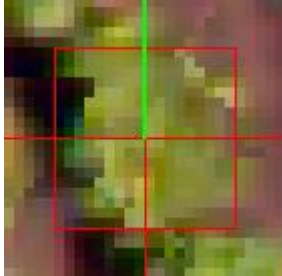
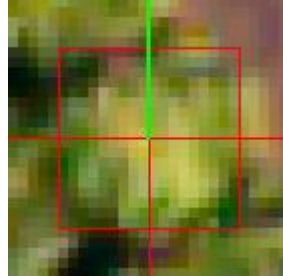


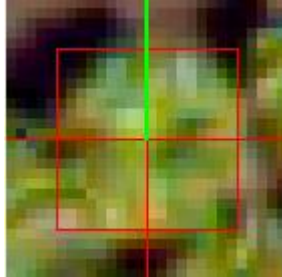


## 8.2 TEMPLATE MATCHING

An optimized template is created during an iterative process, consisting of two main steps: sample template selection and template testing. A template library is built from several manually selected samples. As described in paragraph 5.3 samples with different shapes, sizes, and shadow directions should be selected. Crops can have overlap on four sides; those are all included in the initial template library. The different categories are: no-overlap, one-side, two-side, three-side, and four-side overlap. In addition, other contextual factors should be considered: crops within high-density plots, surrounded by bare soil, situated at a plot's corner, and with shadow. Those criteria resulted in eight selected template samples, presented in table 8.3. A first average template is created based

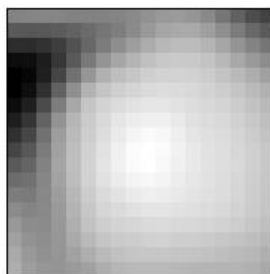


on those 8 samples, the values of the overlapping pixels are averaged. Figure 8.1 shows the results of TM.

**TABLE 8.3 INITIAL SAMPLE TEMPLATES**

<p>No-overlap (bare soil)</p> 	<p>Two-sided overlap</p> 	<p>Three-sided overlap</p> 	<p>Four-sided overlap (high-density plot)</p> 
<p>Non-shadow side</p> 	<p>Shadow side</p> 	<p>Plot corner</p> 	<p>Error</p> 

A region is selected to test the initial average template. This region should include at least one plot with *cichorium* crops and part of the remaining features within the image: bare soil and other vegetation. A test region containing one plot and part of the described surrounding area can contain around 350 to 500 generated matches compared to approximately 100 actual crops. Features that match the initial template are automatically selected and manually checked afterwards. This workflow is facilitated by eCognition, which classifies matches as correct or incorrect. Based on the correct matches and initially selected samples, a new average template is generated. TM is executed on a single spectral band. The band with the highest visual contrast between crops and background, and the highest correlation score during testing is selected. The template test gives a correlation score between 0-1. TM is executed three times, once for every spectral band: red, green, and blue. The green band shows both the highest contrast and highest correlation: 0.768 compared to 0.627 (red band) and 0.591 (blue band).



**FIGURE 8.1 GENERATED TEMPLATE**



TM uses two parameters: a rotation angle and a correlation threshold. The rotation angle defines how many times the template rotates each step. The rotation angle parameter does not need extensive testing. The crops are round-shaped which makes template rotation unnecessary. The correlation threshold determines when a match is detected; a lower value results in more matches and potentially more false-positives. Correlation threshold values between 0.30 and 1 are tested, as shown in table 8.4. The threshold value is decreased by steps of 0.05 from 1 onwards, until no additional crops are detected within plots. A threshold value of 0.55 resulted in 10,883 identified crops and 0.35 resulted in 21,500 identified crops.

**TABLE 8.4 TESTED VALUES TEMPLATE MATCHING PER PARAMETER**

Parameter	Values											
Input layer	Red	Green	Blue									
Rotation angle	0											
Correlation threshold	0.3	0.35	0.4	0.45	0.5	0.55	0.6	0.65	0.7	0.8	0.9	1

To evaluate the results of TM, the true positives (TP), false positives (FP), and false negatives (FN) should be counted and used to calculate an accuracy index (AI). A point is considered a TP when it correctly represents the geographical crop-object. Table 8.5 explains what TPs, FPs, FNs, and true negatives (TN) are in respect to our research. True negatives are not produced during the analysis. The algorithm finds crops and does not find areas without trees. Following two research papers (Pouliot and King 2005; Pouliot et al. 2005), an accuracy index quantifying the trade-off between omission (FP) and commission errors (FN) can be defined as the formula below. The FN value will be zero. The equation allows for negative AI values if the performance is poor.

$$AI(\%) = 100 \left( 1 - \frac{N_{FP} + N_{FN}}{N_{reference\ points}} \right)$$

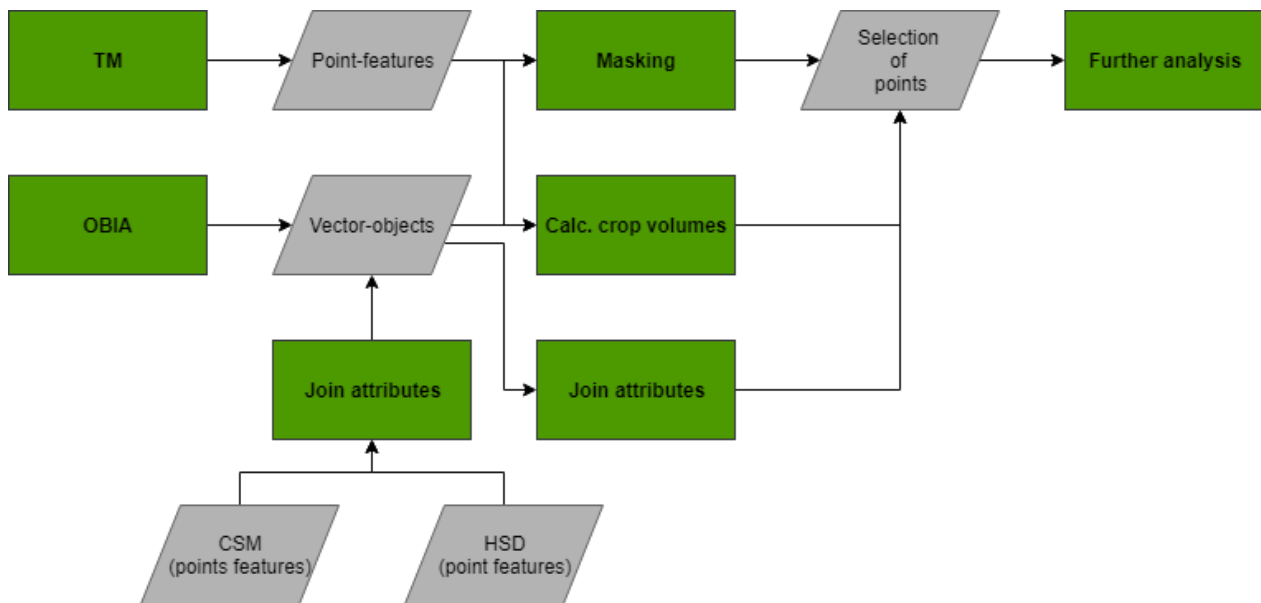
**TABLE 8.5 A DESCRIPTION OF TPs, FPs, FNs, AND TNs**

<b>True Positive</b>	<b>False Positive</b>
Reality: There is an actual crop Computer says: Crop (point-feature)	Reality: There is no actual crop Computer says: Crop (point-feature)
<b>False Negative</b>	<b>True Negative</b>
Reality: There is an actual crop Computer says: No crop (no point-feature)	Reality: There is no actual crop Computer says: No crop (no point-feature)

### 8.3 INTEGRATION OF OBIA AND TM

A workflow in which TM and OBIA are integrated could be a suitable and accurate method to detect a variety of objects within VHR images (Kalantar et al. 2016; Tiede et al. 2017), as is explained in paragraph 5.3. TM and OBIA methods are executed independent and results are integrated in further analysis steps. Those methods result in point-features representing identified crops and vector-objects representing crop-covered areas. The results will be combined within the research’s workflow at three steps. Figure 8.2 gives an overview of the workflow. TM and OBIA come together at the following steps:

1. The image-objects are used to mask (or clip) the point-features;
2. The number of crops within an image-object is used to calculate the average crop volume;
3. Attributes associated with the image-objects are linked to the individual point-features to account for various object sizes and vector image-objects containing different numbers of crops.



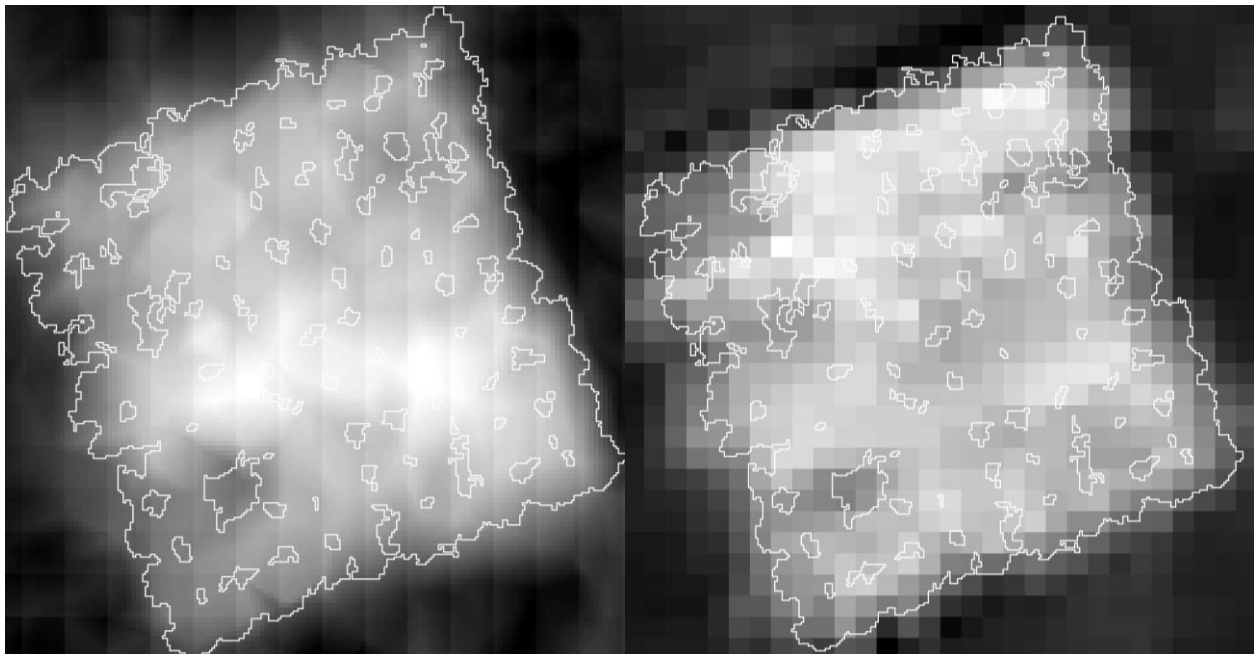
**FIGURE 8.2 WORKFLOW OF THE OBIA AND TM INTEGRATION**

According to Tiede (2014) integrating vector-objects and information of raster images with different scales can be complex. Different options are: select pixels fully within the object, select pixels with any overlap with the object, and select pixels with a certain minimum overlap with the object. As both the CSM and HSD tend to have more error at the edges of real-life objects it is convenient to exclude all pixels partly intersecting the object. The chosen solution can be categorized as “select pixels with a certain minimum overlap”. The raster cells of the HSD and CSM are converted to point-features, representing the cells’ centroid. A value is aggregated to the object-level if the point-feature intersects with the object. This ensures that pixels at the object’s

edge are aggregated to the object if they have approximately 50 percent overlap. Theoretically a pixel with less overlap could also be aggregated to the object if it is underneath a spur of a vector-object. Finally, the area of the object is used together with the number of point-features within an object to calculate average crop volume, as shown in the formula below.

$$\text{Average crop volume} = \frac{\text{Height} * \text{Area}}{\text{Count of crops}}$$

Figure 8.3 shows that the CSM and HSD do not completely match with the created vector-objects. The left image shows hardly recognizable object boundaries in the CSM and the right image shows misalignment of the HSD. The causes of misalignment for the HSD are explained in paragraph 7.1 and the error at the object's boundaries in the DSM in paragraph 7.2. It is debatable whether the object-level is the right way for spatially aggregating raster data. Despite this criticism, both the CSM and HSD tend to represent the general shapes of the plots adequately. An OBIA approach could compensate for errors within crop-covered areas because pixel values will be averaged. Due to geometric distortions and spatial resolution, it is decided that claims on the object-level cannot be done when vector-objects represent small geographical objects like individual crops. The vector-object's attributes are added to the intersecting identified crops and finally averaged to the plot-level in further analysis as explained by the workflow in figure 8.2.



**FIGURE 8.3 THE CSM (LEFT) AND HSD (RIGHT) COMBINED WITH A CROP-OBJECT**

## 8.4 Visualization, statistics and interpretation

As described in paragraph 8.3 both spectral and geometric attributes are assigned to the individual detected crops. Those points are again aggregated to the corresponding plots. This is necessary to account for the fact that some vector-objects almost cover the whole plot while others cover smaller areas or even individual crops. Not taking this into account would cause misleading variation in final statistics. Moreover, the CSM and HSD data-layers are not precise enough for further analyses based on small vector-objects.

The VIs are applied on the spectral object attributes using *Python* together with the *Pandas* library developed for data manipulation and analysis. Reflectance values for available spectral bands are stored in columns within a data table containing all individually identified crops. The *Python* libraries, *Matplotlib* and *Seaborn*, are used for visualization of spectral signatures, VIs, average crop volumes, and correlations. Python scripts are attached in Appendix XIV to XVII. A boxplot is a simple visualization method for insights on basic statistics. It visualizes the median, the quartiles, and the highest and lowest values, so-called outliers. The spread, symmetry, and level of distribution can easily be identified and described according to the boxplot (Williamson, Parker, and Kendrick 1989).

Murakami and Idezawa (2013) have shown positive correlation between crop-covered areas and fresh weights of plants for different treatments of *crisphead lettuce*. This research will investigate if there is correlation with the estimated crop volumes and the in-situ shoot biomass per treatment measured by Barel et al. (2018). A suitable correlation test will be executed which describes the dependency of the variable volume on the independent variable biomass. The Pearson correlation coefficient is a common measure for linear correlation between variables  $x$  and  $y$ . Pearson correlation is sensitive to data distribution; it assumes values to be continuous, normally distributed, and linear related. A non-parametric approach could give more meaningful results if normality does not hold (Soper et al. 1932). Spearman correlation coefficient is a non-parametric measure which describes the relationship's monotonicity between two datasets and does not assume normality (Hauke and Kossowski 2011).

An Analysis of Variance (ANOVA) or non-parametric Kruskal Wallis test could provide additional statistical information. These methods can test for significant differences between population's means of two or more groups (Fisher 1928). The ANOVA test is used in a similar context by Meij et al. (2017); they measured the statistical difference between in-situ quantified plant traits as chlorophyll and predicted plant traits. Volume and shoot biomass have incomparable units of measurement, so a statistical comparison of the means between those two groups will not be carried out in this study. The Spearman correlation test is more suitable.

# 9 RESULTS

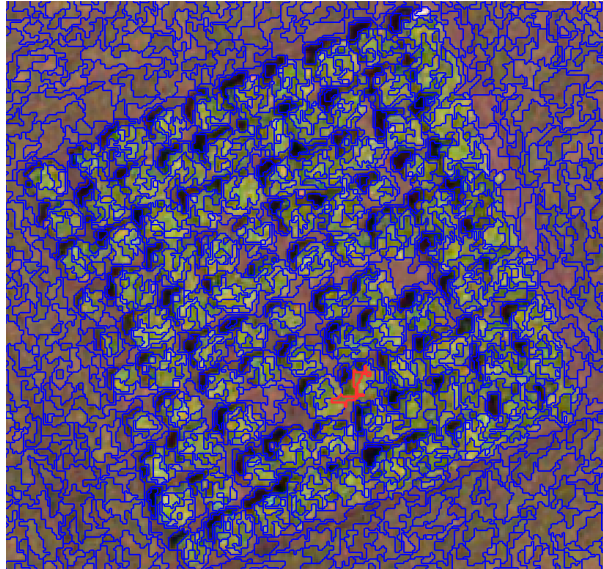
The results of OBIA and stratified TM are presented in this chapter. *MIRS* and further classification results in vector-objects covering *cichorium* crops adequately, while excluding bare soil within plots. TM produces over 21,500 points-features of which 15,000 false positives. An integration of the resulting vector-objects and point-features resulted in 8 false positives and 1 false negative for crop detection. The overall accuracy rate of the combined methods for identifying crops is 99.8%. Technically, the OBIA-based results show two major advantages. First, the method compensates for peaks in additional datasets, like the CHM, and underrepresented areas at the object's edges. Those values are aggregated to the vector-object-level. Second, the natural shape of vegetation is well represented by the vector-objects. This allows for accurate calculations of crop-covered area which is difficult with a common pixel-to-pixel approach and related classification methods.

## 9.1 OBIA

*MIRS* is executed as described in paragraph 8.1. Highest sensitivity and most influence on the OBIA results is shown for the scale-factor, the contrast enhancing VI used, and related classification. A scale-factor that is too high will include many shadows within vector-objects. The threshold value to classify segments based on the VI is sensitive; crop-covered areas can easily be under- or overrepresented if this value is changed.

*MIRS*, in combination with a suitable classification, is well capable of distinguishing crop-covered areas. The contrast enhancing VI *TGI* delivers proper results with classification. Both the VI and the VI classification threshold could be different for other crop species or light conditions. After segmentation and classification, in total 339 objects are identified as *cichorium* crops. An overlay with the plots (AOI) resulted in 138 objects identified as false positives because they are located outside the plots.

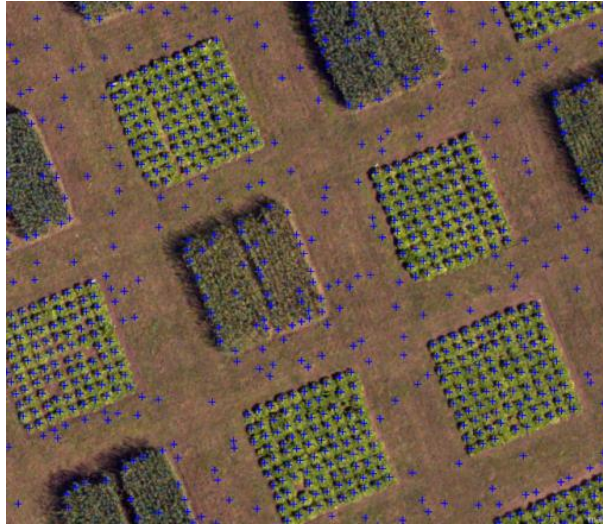
A single crop could be covered by several fine segments before classification. Moreover, within high-density plots, segments could include parts of two or more individual crops, as shown in figure 9.1. Single objects for individual crops could not be built by *MIRS* within a high-density plot. If a crop is surrounded by bare soil, around 3-6 centimetre, a single object could be created for that crop. Bare soil and shadows are not classified as crop-objects. The objects are highly suitable for calculating crop-covered areas and data fusion with additional data-layers.



**FIGURE 9.1 SEGMENTS CREATED BY MIRS FOR ONE OF THE PLOTS WITHIN THE EXPERIMENTAL FIELD. THE RED OBJECT IS AN OBJECT THAT IS PART OF TWO DIFFERENT PLANTS.**

## 9.2 TEMPLATE MATCHING

With the final used settings, 21,500 spots are identified as crops, in contrast to the actual total of 5,930 crops. As described in paragraph 8.2, decreasing the threshold value for TM results in less missing crops within plots, which means a smaller number of false negatives but a tremendous number of false positives. TM as a stand-alone method is not suitable for crop detection. Visual inspection shows that crops are identified precisely within plots, without hardly any false negatives. In terms of accuracy, most points are not representing the exact crop's centroids. The points tend to be located more towards the crop's shadow. TM is non-time-consuming and achieves good results. Objects with different characteristics and conditions (e.g. size, shape) can easily be included within the workflow.



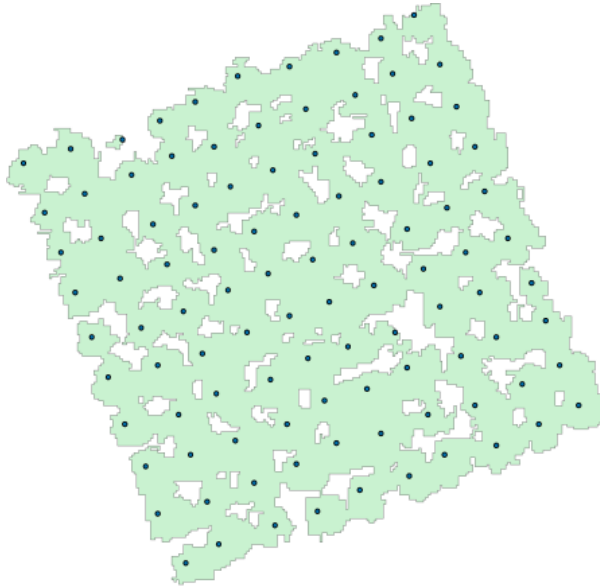
**FIGURE 9.2 MATCHES WITH TM FOR PART OF THE EXPERIMENTAL FIELD.**

### 9.3 INTEGRATION OF OBIA AND TM

The combination of the resulting objects from OBIA with TM delivers accurate results. The image-objects are used as a mask for the matches derived with TM as explained in paragraph 8.3. In this way, points outside the vector-objects are identified and removed. This results in 5,922 identified *cichorium* crops. All plots are inspected to identify and count false positives and negatives. A false positive is found on plot 34 and a false negative on plot 21, 37, 61, 67, 80, 86, 92, 94, and 119. The *cichorium* crops are detected with an accuracy of 99.83%. An example of the combined OBIA and TM dataset is presented in figure 9.3; results are summarized in table 9.1. The vector-objects, point-features, and their integration is shown for the complete field in Appendix IX to XI.

**TABLE 9.1 RESULTS OF TM AND THE COMBINATION WITH OBIA**

Manual	Actual number of crops	5,930
TM	Identified crops	21,500
TM and OBIA	Identified crops combined TM and OBIA	5,922
	True Positives (TP)	5,921
	False Positives (FP)	1
	False Negatives (FN)	9
	Overall accuracy	99.83%



**FIGURE 9.3 RESULTS OBIA AND TM COMBINED FOR ONE OF THE PLOTS WITHIN THE EXPERIMENTAL FIELD.**

#### 9.4 SPECTRAL ANALYSIS

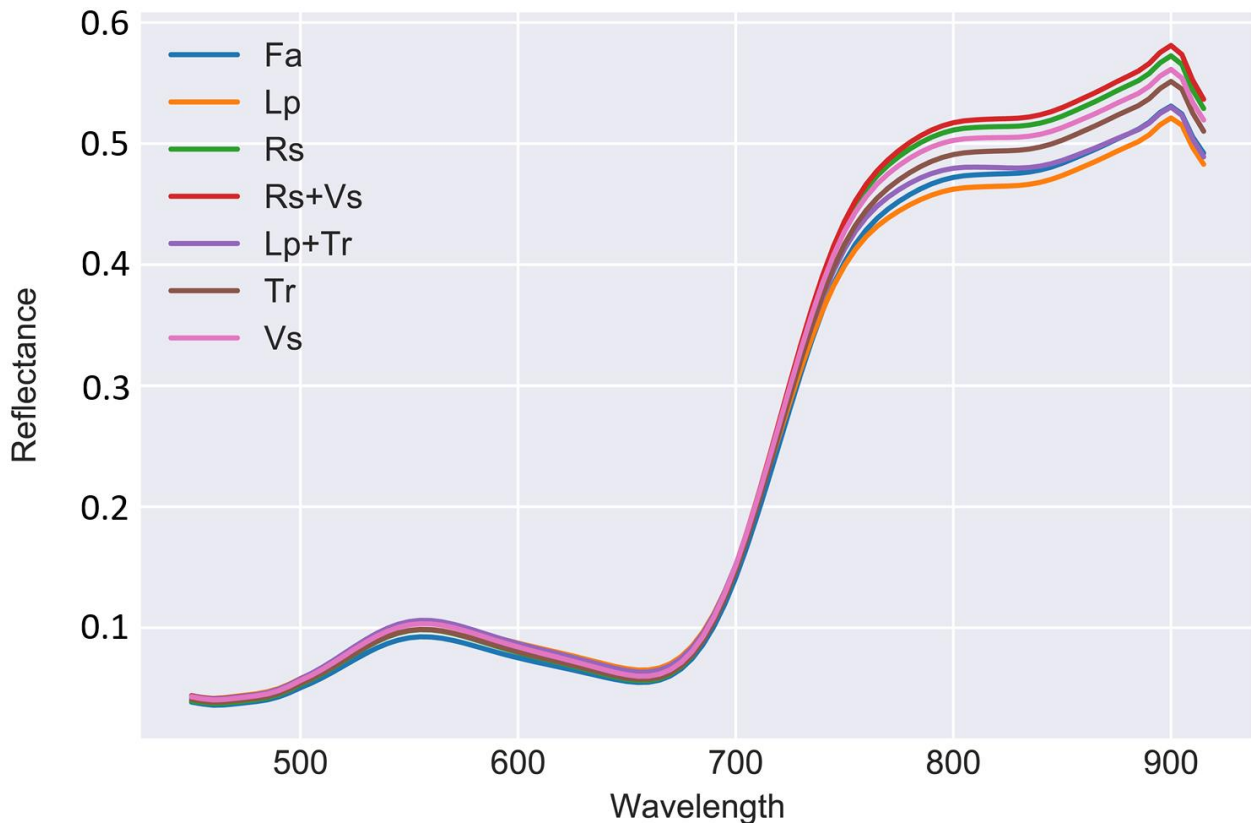
The spectral signatures of *cichorium* are discussed and compared for all associated plant-soil treatments. Figure 9.4 shows the full spectral signatures; the visible and near-infrared part of the electromagnetic spectrum are shown separately in figure 9.5. Within the green part of the visible spectrum, the following three plant-soil treatments have the highest average reflectance values: (1) the combination of *lolium* and *trifolium*, (2) *lolium* monoculture, and (3) the mixture of *raphanus* and *vicia*. This higher reflectance could indicate a higher amount of green chlorophyll pigments within the plant. Within the near-infrared part of the visible spectrum the following three plant-soil treatments have the highest average reflectance values: (1) the combination of *raphanus* and *vicia*, (2) *raphanus* monoculture, and (3) *vicia* monoculture. As described in paragraph 5.3, high reflectance at the near-infrared wavelengths is mainly caused by the internal structure of healthy leaves.



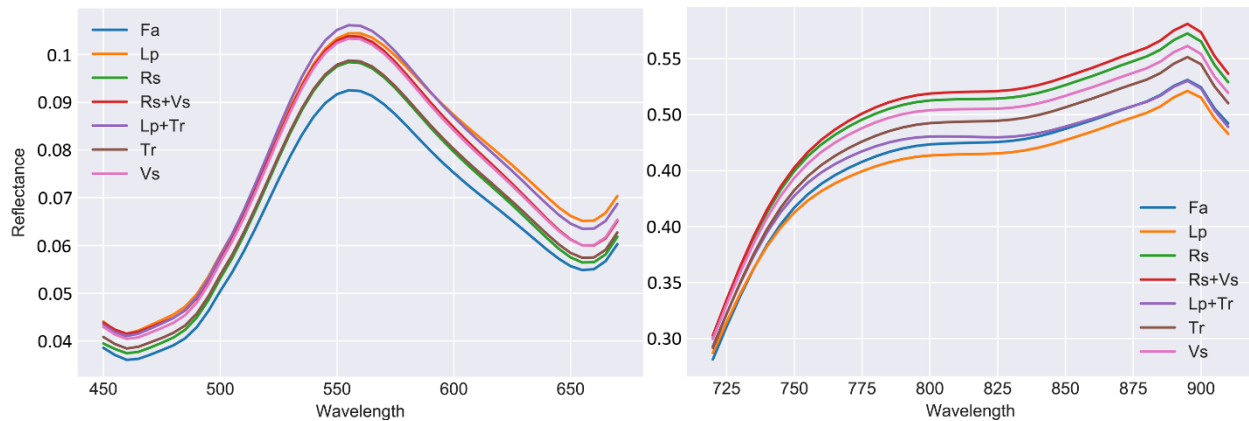
**TABLE 9.2 OVERVIEW OF ALL PLANT-SOIL TREATMENTS INCLUDING A CONCLUSION BASED ON THE SPECTRAL ANALYSIS**

Abbreviation	Full name	Main conclusion(s)
Fa	Fallow	Low performance with leaf chlorophyll content (LCC) related VIs.
Lp	Lolium	Low performance with all Vis.
Rs	Raphanus	High performance with leaf chlorophyll (LCC) related VIs.
Rs + Vs	Raphanus and Vicia mixture	High reflectance values within the NIR part and spectrum overall. High performance with leaf chlorophyll (LCC) related VIs.
Lp + Tr	Lolium and Trifolium mixture	Highest reflectance values in the green part of the electromagnetic spectrum. Low performance with all VIs.
Tr	Trifolium	Average performance with all VIs
Vs	Vicia	Average performance with all VIs

Notable is that *raphanus* as a monoculture and mixture has high reflectance values overall which likely indicates a high productivity. A quantitative comparison of the productivity between the treatments is not directly possible based on the spectral signatures only. A notable treatment is the combination of *lolium* and *trifolium*, as it has one of the highest reflectance values in the green part of the visible spectrum but low reflectance values in the near-infrared spectrum.



**FIGURE 9.4 THE SPECTRAL SIGNATURES OF *CICHORIUM* GROWN IN DIFFERENT EXPERIMENTAL PLOTS WITH ASSOCIATED TREATMENTS. PLANT-SOIL TREATMENTS ARE *FALLOW*, *LOLIUM PERENNE*, *RAPHANUS SATIVUS*, *TRIFOLIUM REPENS*, *VICIA SATIVA*, AND TWO MIXTURES.**

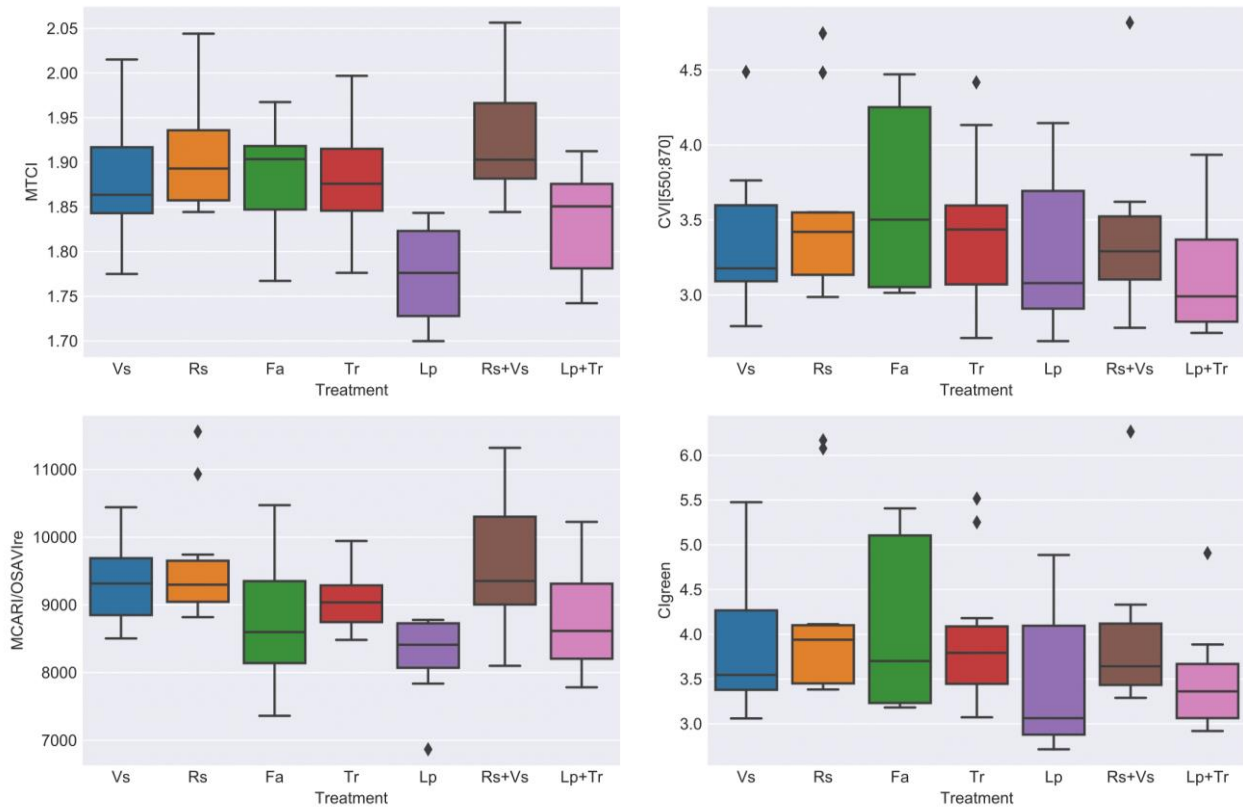


**FIGURE 9.5 THE SPECTRAL SIGNATURES OF CICHORIUM GROWN IN DIFFERENT EXPERIMENTAL PLOTS WITH ASSOCIATED TREATMENTS, ZOOMED-IN ON THE VISIBLE (LEFT) AND THE NEAR-INFRARED PART (RIGHT) OF THE SPECTRUM.**

Figure 9.6 shows two *red-edge* VIs: MTCI (sensitive for LCC, N, and height) and MCARI/OSAVI<sub>red edge</sub> (LCC), and two VIs including green: CVI (LCC and LAI) and CI<sub>green</sub> (LCC). Additional vegetation indices are attached in appendix XVIII and their sensitivities and sources in paragraph 5.4. A treatment is classified as underperforming if the mean value for a VI is relatively low, the variance is relatively large, or both. The most optimal treatment should show a relatively high mean and a small variation between image-objects. This could indicate a stable high production; the treatment is classified as outperforming.

The *fallow* treatment underperforms for most indices like MCARI/OSAVI, TCARI/OSAVI, and their red edge counterparts. *Fallow* shows large variations between plots with REP, CVI, CI<sub>green</sub>, CI<sub>red edge</sub>, and NDVI [550,800]. The indices where *fallow* underperforms mainly focus on LCC. Despite low performance with the mentioned indices, the treatment performs well with CVI, MTCI, NDVI [720,820], and NDVI [735,750]. Together with the low reflectance values in the green part of the spectrum, as shown in figure 9.5, this could indicate a low amount of chlorophyll within the crops.

The underperformance of crops treated with *lolium* monoculture applies for all VIs and is, therefore, much clearer as for *fallow*. The same applies for the mixture *lolium* and *trifolium*, although this mixture performs slightly better for all indices than *lolium*'s monoculture. The mixture *raphanus* + *vicia*, and the monoculture *raphanus* outperform with the MCARI/OSAVI<sub>red edge</sub> and TCARI/OSAVI<sub>red edge</sub> indices. Both indices are strongly related to LCC but insensitive to other aspects as LAI. *Raphanus* monoculture shows smaller variation between plots compared to its mixture, this could indicate a stable high production of *cichorium*. *Raphanus* monoculture slightly outperforms the mixture and performs equal for all indices. The ranking of the vegetation index CVI is deviating from other VIs. CVI which is mainly sensitive to LCC and LAI, shows best results for *fallow*, *trifolium* and *raphanus*.



**FIGURE 9.6 THE AVERAGE VEGETATION INDEX VALUES OF *CICHORIUM* GROWN IN DIFFERENT EXPERIMENTAL PLOTS WITH ASSOCIATED TREATMENTS. VEGETATION INDICES ARE MTCI, CVI, MCARI/OSAVI RED EDGE, AND CI GREEN.**

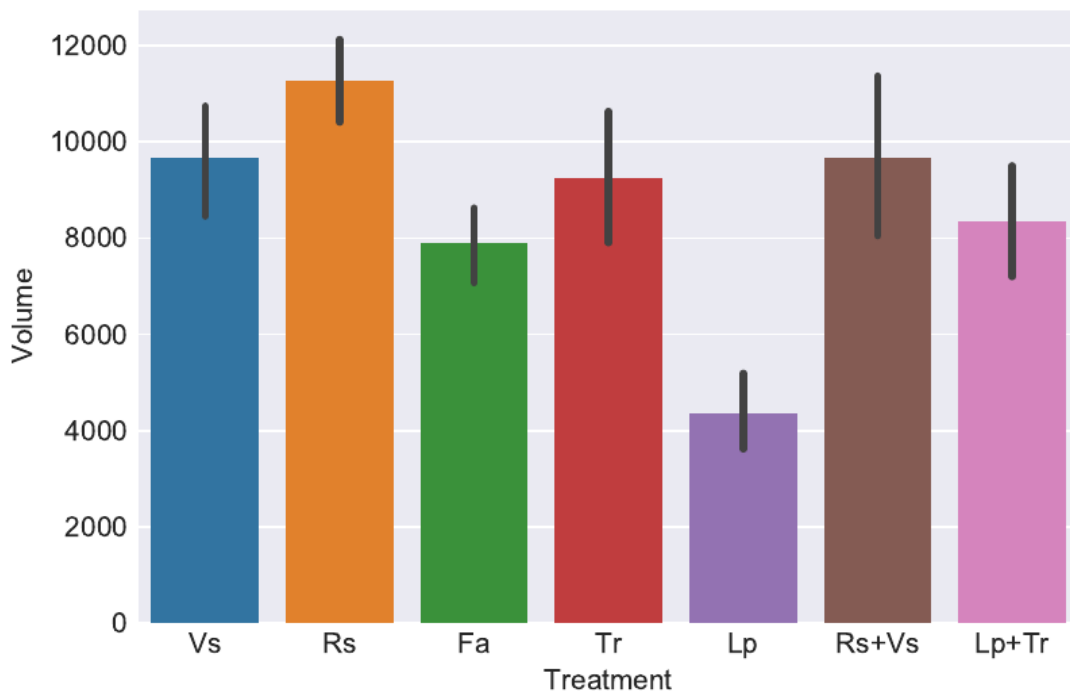
## 9.5 GEOMETRIC ANALYSIS

The average plant-volumes in cubic centimetres are visualized in figure 9.7. As described in paragraph 7.2, plots 105, 106, 108A, and 108B are removed due to distortion. Those plots are part of the following treatments respectively: *fallow*, *lolium*, *lolium + trifolium*, and *raphanus + vicia*. The *raphanus* monoculture is the most productive treatment based on the volume calculations. *Raphanus + vicia*, *vicia* monoculture, and *trifolium* monoculture show good results as well. Especially *lolium* monoculture is underperforming and it is notable that there is a significant difference with its mixture. This generally corresponds with the results based on the spectral data. The difference between *raphanus*'s monoculture and its mixture also stands out clearly. A visualization of the average crop volume per plot is presented in appendix XX.

**TABLE 9.3 OVERVIEW OF ALL PLANT-SOIL TREATMENTS INCLUDING A CONCLUSION BASED ON THE GEOMETRIC ANALYSIS**

Abbreviation	Full name	Main conclusion(s)
Fa	Fallow	Moderate performance.
Lp	Lolium	Lowest performance.
Rs	Raphanus	Highest performance.
Rs + Vs	Raphanus and Vicia	High performance. Lower performance than Raphanus monoculture.
Lp + Tr	Lolium and Trifolium	Moderate performance. Higher performance than Lolium monoculture.
Tr	Trifolium	High performance.
Vs	Vicia	High performance.

Statistical exploration of the volume and shoot biomass data shows that volume is normally distributed while shoot biomass is not. These explorative statistics are shown in appendix XIX. Shoot biomass' distribution is more hyperbolic than linear. The hyperbolic distribution could have a significant influence on the performance of Pearson correlation coefficient. Pearson shows an f-value of 0.433 and a p-value of 0.000286. F-value 0 means no correlation, +1 an exact monotonic positive relation, and -1 an exact monotonic negative relation. Alternatively, Spearman correlation coefficient is used as it does not assume normal distribution. Spearman shows an f-value of 0.462 and a p-value of 0.000094.



**FIGURE 9.7 AVERAGE PLANT-VOLUME (CM<sup>3</sup>) INCLUDING 95% CONFIDENCE INTERVAL**

# 10 DISCUSSION

The suitability of the investigated methodology for analysing plant traits and plant-soil treatment's legacies is discussed. The emphasis is on both strengths and deficiencies of the followed procedures. Important aspects are the degree of detail, accuracy, scalability, and automation. The discussion could give more insights on the potential of the methodology for delivering in-time information, usable for precision agriculture. This chapter will follow the six research questions presented in chapter 3.

## 10.1 OBIA

Multiresolution image segmentation (MIRS) alone is not capable of building single objects for individual crops. As described in Benz et al. (2004), the algorithm minimizes the average heterogeneity of image-objects over the whole image. It creates a hierarchical structure of fine objects; this hierarchical structure could have helped with classification and creating final crop-objects. Unfortunately, it turns out that too many fine objects cover multiple geographical crop-objects, as shown in figure 9.1. Despite its fine objects, MIRS likely has problems related to an old trade-off in image segmentation: averaging pixels over a larger area is needed to be certain about a pixel's class, while on the other hand, this makes the location of the object boundaries less certain (Bhalerao 1995). This finding shaped the rest of the research in terms of further chosen methodologies and the level of detail in the results.

Further research could investigate or develop new algorithms for improved individual crop segmentation and classification. It is decided to combine OBIA with a method for object detection. TM has the problem of overdetection, as previously described by Cheng and Han (2016). The problem is averted by using the OBIA objects for stratification. Individual *cichorium* crops could be detected with an accuracy of 99.83% based on VHR optical UAV-images using OBIA in combination with TM. More details on these results are shown in paragraph 9.3 and detected crops are shown in figure 9.3 and appendix XI.

There is some criticism on the classification method used. The classification does not make use of the hierarchy between fine objects. This is not possible because fine scale objects are not capable of representing single geographical crops, as they often overlap multiple crops. Instead, all three spectral bands red, green, and blue are used together within a VI for classification. The suitable VI is likely different for other crop species. Moreover, the classification threshold value of the VI is highly sensitive in respect to the OBIA results.

The objects derived with MIRS can be described as crop-covered areas instead of individual crops. Only if there is a minor buffer of bare soil (around 3-6 cm) around a crop, can this crop be represented by a single image-object, as shown in appendices III to V. This means that individual

crop-objects could have been built in early season. Plots include approximately 100 actual crops and are surrounded by bare soil, as shown in figure 6.1. If information about crop area on a more detailed level is desired, it is recommended to plant in smaller plots or rows. Despite this setback, it can be concluded that the resulting image-objects are highly suitable for calculating crop-cover surface. Crop and non-crop areas are well distinguished by the MIRS algorithm.

Until an algorithm is developed that could create single objects for individual crops despite overlap, it should be considered how many geographical crops an image-object represents. The detected crops with TM are suitable to use as a weight factor for image-objects. The object's surface can be averaged to a crop-level. Moreover, the smaller the number of crops without overlap with other crops the more accurate the results could be on the individual crop-level. No research is found in which they are able to build image-objects for individual crops. Torres-Sánchez et al. (2015) comes close, although they do not include a weight factor based on the number of crops within the image-object.

## 10.2 DATA FUSION

Combining other data sources with OBIA-objects is not self-evident. The DSM is well aligned with the orthophoto, but this is not the case for the HSD. Misalignment is shown in figure 7.1. The spectral data was captured by an additional sensor attached to the UAV. This allowed for a minor geometric shift between the orthophoto and the HSD. Although pre-processing steps are repeated and refined, the HSD is not suitable enough for individual crop-based analysis because of minor misalignment. An alignment error with a maximum of only a few percent of the total crop-width is desired. In this case, it is in our favour that MIRS creates objects containing multiple crops. Possible errors for individual crops are in this way disguised. Results of this research are promising as spectral analysis shows similar patterns as the field analysis of Barel et al. (2018) and the geometric analysis. Potential error-effects are overestimating and underestimating the VI values because of the exclusion or inclusion respectively of non-crop pixels. Further research on those effects is necessary but can only be done if field measurements for individual crops' plant traits, such as chlorophyll, are available. The development of a hyperspectral sensor which additionally creates RGB images is promising, as it does not allow for misalignment. Such a system is described by Chen et al. (2014) and the first sensor (RIKOLA Hyperspectral Camera) is successfully applied by Roosjen et al. (2018).

Distortions of a digital surface model (DSM) are common for height models created by stereo photogrammetry or digital aerial photogrammetry (DAP) (Tilly et al. 2014). Underestimated values occur at the edges of objects, overestimated values in the middle, and objects tend to be larger than the real-life objects. Again, the larger the image-objects, the smaller the effects of the DSM on the results. DAP data does not seem suitable for individual crop volume calculation, although it is suitable for finding patterns of productivity for different plots and treatments, based on average

crop volume. It should be considered that smaller and more isolated image-objects tend to have underestimated height values.

The height values of the CSM are depended on the DSM and the DTM. An accurate DTM can only be created if enough areas without vegetation cover are available for selection and interpolation, as shown by Goodbody et al. (2017). Special attention is needed around mosaic-lines within the image, a mosaic-line is where two flight lines are combined. It is decided to exclude three plots from the geometric analysis, because of too much distortion around the mosaic-line. A height deviation of 20 centimetres between the flight lines is too much when working on a crop scale. More about the DSM and CSM is explained in paragraph 7.2. With LiDAR technology real 3D object representations can be created without the cons of DAP. It is able to accurately estimate volume and aboveground biomass under conditions where passive optical and active radar sensors typically fail (Lefsky et al. 2002). Unfortunately, LiDAR's suitability for flexible applications in precision agriculture is limited, as it is far from being cost effective compared to UAV-technologies (Goodbody et al., 2017).

For further analysis, data fusion is necessary. Both the HSD and CSM data-layers need to be aggregated to the object-level. According to the literature this could be done by: selecting pixels completely within the image-object, selecting pixels with any overlap with the image-object and selecting pixels with a certain minimum overlap with the object (Tiede, 2014). Considering the distortions of the DSM, it is likely best to include only the pixels completely within objects. No comparisons of different selection procedures are executed, which is an accepted drawback. It is assumed that effects on the results between the different approaches are small due to reasonably fine pixel sizes. The method used creates a centroid for each raster cell. The attributes of all points within the target image-object are assigned to that object. More information on data fusion can be found in paragraph 8.3. The method was most feasible in respect to time and technical constraints. It can be categorized as selecting pixels with a certain overlap.

### 10.3 PLANT DIMENSIONS BASED ON DSM

Plant dimensions as crop-covered area, average crop volume, and biomass can be derived using OBIA and TM. Total crop-covered area can be calculated precisely, OBIA captures and represents crop-covered areas without including any shadows or within plot bare soil. It is assumed that statements about the crop-covered area could not be as detailed when using traditional pixel-to-pixel approaches. In particular, the exact crops' borders and bare soil areas within plots would have been difficult to incorporate with other methods. Second, average crop volume can be determined using OBIA in combination with TM. It was expected that OBIA could build objects around single real-life objects, but this is not possible. OBIA combined with TM is a suitable method for calculating average crop volume. A moderate positive correlation is found between average crop

volume and biomass. This confirms that volume can be used to make statements about crops' biomass. A more accurate DSM likely improves correlation.

## 10.4 BIOCHEMICAL PLANT TRAITS BASED ON HSD

Biochemical plant traits can be derived to a limited extent and with a limited certainty. Some vegetation indices focus mainly on leaf chlorophyll content (LCC), while others are also sensitive to other biochemical plant traits. For further elaboration on the used vegetation indices, consult paragraph 5.4. Different types of vegetation indices do not show remarkable contrasting results. Consequently, biochemical traits other than LCC cannot be predicted. It must be taken into consideration that in-situ measurements for those traits are not available. Correlation tests and mean-comparison tests, like ANOVA and Kruskal Wallis, could therefore not be applied. The estimations of LCC are compared with theories on plant-soil feedback and findings of the field experiment by Barel et al. (2018). Most effects on LCC are caused by the availability of N in the soil. The N-pool increases with more available organic material and more release of N by bacteria and fungi (Hodge, Robinson, and Fitter 2000). Similar patterns compared to Barel et al. (2018) can be found between plant-soil treatments for most vegetation indices.

## 10.5 PLANT-SOIL TREATMENT'S LEGACIES

Barel et al. (2018) states that treatments including *raphanus* could be a threefold more productive than *trifolium* and *lolium* monocultures and its mixtures. Although the difference is not as large as stated by Barel et al. (2018), this pattern is clearly visible in figure 9.7 which represents the results of the geometric analysis. An interesting finding is that the *raphanus* + *vicia* mixture performs slightly better than *raphanus* monoculture with most vegetation indices, as shown in figure 9.6 and appendix XVIII, which goes against the results of Barel et al. (2018) and our own geometric analysis. Field measurements of *chlorophyll* could determine if the VIs deliver correct information. A question arises from the findings: do successive crops of the *raphanus* + *vicia* treatment indeed contain more chlorophyll and are they healthier? When talking about productivity and general differences between treatments, the geometric analysis seems to deliver sufficient results.

Barel et al. (2018) saw no difference between the monoculture and related mixture treatments for *cichorium*'s productivity. An interesting finding is that both geometric and spectral analysis show differences between the two. With the geometric analysis, the *raphanus* monoculture performs better than *raphanus* + *vicia* mixture. Besides, *lolium* + *trifolium* mixture performs much better than its *lolium* monoculture. Especially, the *lolium* monoculture is underperforming for all vegetation indices. Finally, Barel et al. (2018) found that *lolium* monoculture, its mixture, and the *fallow* treatment significantly reduced the production of *avena* due to N availability. The reason for this is that the release of N by bacteria and fungi in the soil takes longer compared to other treatments. *Cichorium* crops are planted a few months after *avena* crops. It was expected that



effects of plant-soil feedback would be less visible between treatments, but the effects are still notable. So, an interesting finding is that the effects of these plant-soil treatments occur longer than expected. Research in the field of plant-soil feedback should confirm and clarify this.

Besides minor differences and notable findings, OBIA results are largely in line with results of previous studies. Especially the *lolium* monoculture is underperforming with the geometric analysis and for most VIs with the spectral analysis, as shown in figure 9.6 and 9.7. This corresponds with the findings of Barel et al. (2018) and the theory of Hodge et al. (2000). High performance of *raphanus* monoculture and mixture also corresponds with previous findings. Assumptions about productivity can be done and patterns recognized. Notwithstanding, because of the lack of field measurements of biochemical plant traits, it is first hard to determine accuracies for plant trait estimations, and second to prove which plant-soil feedback mechanisms are accountable for the differences between treatments.

## 10.6 SCALABILITY

As described by Andújar et al. (2016), UAVs are affordable and allow for flexible in-time delivery of information, are able to capture VHR optical images, and are not affected by clouds. DSMs can be derived automatically by DAP (Suomalainen et al. 2014). To be able to automate further analysis, data quality must be sufficient and consistent. It would be excellent if the methods and parameters used are directly scalable. However, there are some aspects that could be different for every dataset.

Although an UAV-derived orthophoto and DSM can currently be georeferenced automatically, extensive quality checking and additional pre-processing is still needed. It needs to be assessed if the orthophoto, HSD, and DSM are aligned sufficiently. Alignment is a time-consuming process. The development of a combined sensor is a true deal-breaker because it makes rectification completely superfluous. Moreover, a DTM must be created to be able to derive crop heights. DTM creation is only possible if there are enough bare ground areas between plots and around the field. If there are mosaic-lines in the image, it must be assessed if measurements around the line should be excluded in further processing and analysis due to height deviations.

The images used are taken just before harvest. As described before, images taken earlier in the season would improve results from the OBIA perspective. It is expected that the vast majority of the crops will be represented by single objects. It is assumed that the same MIRS parameters and *TGI* vegetation index can be used for *cichorium* crops during the whole season. It is also assumed that the *TGI* vegetation index is applicable for other light green crops; for dark green crops this assumption cannot be made. As the threshold value for classification based on the *TGI* vegetation index is highly sensitive to changes, this needs special care. When applying the investigated methods on other crop species, the most suitable segmentation parameters (especially the scale-factor), chosen vegetation index, and classification threshold value may be different.

It is assumed that the same template for TM could be used during the whole season because it incorporates different shadow directions, and the shape of the crops does not change over time. For other crop species, a different crop template should be built. TM is semi-automated within eCognition and easy to use, so no obstacles are foreseen. The crops in the image showed overlap, had irregular shapes, and included shadows. Based on these difficult conditions, it is assumed that TM will deliver similar results for other crop species. TM will only become more difficult when objects are generally not round shaped.

# 11 CONCLUSION

This chapter answers the main research question: “To what extent could plant-soil treatments’ legacies be identified using VHR optical UAV-imagery incorporating OBIA methods and techniques; considering plant dimensions, biomass and biochemical plant traits?”

The real power of OBIA is its ability to accurately calculate the areas of concerned real-life objects, even if shapes are irregular and small areas representing other land-use types are located within and between objects. The MIRS algorithm is not capable of detecting individual crop-objects in high-density areas nor building individual crop-objects. The TM detection algorithm can detect crops with an accuracy of 99.8% if used together with the results of MIRS. The quality of the HSD and DSM is rated insufficient for data fusion with individual crop image-objects. The resulting objects include a maximum of 10 x 10 crops, without including any shadow or bare soil. If an actual crop is surrounded by at least 3-6 cm of bare soil on all sides, it is represented by a single image-object. The larger resulting image-objects are found better suitable for further analysis in respect to the characteristics of additional data sources. In this way, an OBIA approach compensates for peaks and underrepresented areas in additional datasets, like in the CHM.

An advantage of using both TM and OBIA together is that the average crop area and volume can be calculated for image-objects representing multiple crops. This information could give insights on the crops’ productivity. The calculated average crop volume is a reasonable indicator for biomass as a moderate positive correlation was found between average crop volume and shoot biomass. The *raphanus* monoculture is the most productive treatment based on the volume calculations. *Raphanus* + *vicia* mixture, *vicia*, and *trifolium* show good results as well, while the *lolium* monoculture is underperforming. This pattern corresponds with the findings of Barel et al. (2018).

*Raphanus* monoculture and its mixture treatment have high reflectance values over the whole electromagnetic spectrum. The underperformance of crops treated with *lolium* monoculture and its mixture applies for all VIs. It is notable that differences between monocultures and mixtures are less present compared to the geometric analysis, which is more in line with Barel et al. (2018). They see no difference between the monoculture and related mixture treatments for the production of *cichorium*. Vegetation indices with different sensitivities did not show remarkable contrasting results.

The notable clear differences between treatments is not only interesting from a methodological perspective. It was expected by Gerlinde de Deyn, co-author of Barel et al. (2018), that effects of plant-soil feedback (PSF) would be minimal for *cichorium*. This because *cichorium* crops were planted a few months after *avena* crops, the other examined crop species in their research. The effects of the plant-soil treatments occur longer than expected.

The difference between plant-soil treatments' legacies could be identified in the hyperspectral and geometrical analysis; main patterns match with results of previous research based on destructive sampling. The methodology could be used in large scale research concerning plant-soil feedback and in precision agriculture. The UAVs flexibility and affordability together with the detail with which OBIA and related methods could give information about crop productivity, are a strong and promising combination for applications in precision agriculture. Although some adjustments are needed, it is assumed that the investigated methodology can be applied under different conditions and with different crop species.

# 12 RECOMMENDATIONS

There is a need for extended research that includes field measurements on the individual crop-level while covering a broader aspect of plant traits. This enables discovering and describing statistical relations between metrics of crops' image-objects and field measurements. This will provide more insight on the variability of certain OBIA metrics between individual crops. When estimation of certain plant traits on the individual crop-level is desired for precision agriculture, it is not only needed to find patterns and relations but also to prove consistency of the estimates.

As MIRS was not capable of building objects for individual crops, alternative algorithms need to be investigated or developed. It will be challenging to automatically build objects for individual crops in high-density areas. A suggestion is to look at seeded segmentation algorithms that could take detected crops, like detected with TM, as a starting point for building segments. It is recommended to work with a segmentation library in a programming language if possible. This allows for an extensive sensitivity analysis with multiple combinations of settings.

It is also recommended to investigate technologies and methods with which a more precise height model could be created. Segmentation algorithms based on a height model could then be investigated. A height model could also be represented by a point cloud instead of a raster-based DSM. Segmentation based on a point cloud enables creation of additional height metrics as standard deviation, maximum, minimum and mean height. Moreover, as described in paragraph 7.2, a DTM is needed to normalize the DSM and calculate crop heights. Within areas of large vegetation-cover, it can be difficult to derive an accurate DTM. It should be investigated if a LiDAR-based DTM could be used together with a DAP-based DSM.

As regards to data fusion with hyperspectral data, new sensors that could create optical as well as hyperspectral images at once are a welcome contribution. It ensures excellent alignment between the optical and hyperspectral images. This is necessary if accurate estimations of biophysical plant traits are desired for fine image-objects.



# 11 BIBLIOGRAPHY

- Andújar, D., A. Ribeiro, C. Fernández-Quintanilla, and J. Dorado. 2016. “Using Depth Cameras to Extract Structural Parameters to Assess the Growth State and Yield of Cauliflower Crops.” *Computers and Electronics in Agriculture* 122 (March): 67–73. <https://doi.org/10.1016/j.compag.2016.01.018>.
- Barel, J., T. Kuyper, W. de Boer, J. Douma, and G. de Deyn. 2018. “Legacy Effects of Diversity in Space and Time Driven by Winter Cover Crop Biomass and Nitrogen Concentration.” *Journal of Applied Ecology* 55 (1): 299–310. <https://doi.org/10.1111/1365-2664.12929>.
- Benz, U., P. Hofmann, G. Willhauck, I. Lingenfelder, and M. Heynen. 2004. “Multi-Resolution, Object-Oriented Fuzzy Analysis of Remote Sensing Data for GIS-Ready Information.” *ISPRS Journal of Photogrammetry and Remote Sensing* 58 (3–4): 239–58. <https://doi.org/10.1016/j.isprsjprs.2003.10.002>.
- Bhalerao, A.H. 1995. “Multiresolution Image Segmentation.” *1995 International Conference on Acoustics, Speech, and Signal Processing* 4 (November). <https://doi.org/10.1109/ICASSP.1995.479980>.
- Blaschke, T. 2010. “Object Based Image Analysis for Remote Sensing.” *ISPRS Journal of Photogrammetry and Remote Sensing* 65 (1): 2–16. <https://doi.org/10.1016/J.ISPRSJPRS.2009.06.004>.
- Boissonnat, J.D., and F. Cazals. 2002. “Smooth Surface Reconstruction via Natural Neighbour Interpolation of Distance Functions.” *Computational Geometry: Theory and Applications* 22 (1–3): 185–203. [https://doi.org/10.1016/S0925-7721\(01\)00048-7](https://doi.org/10.1016/S0925-7721(01)00048-7).
- Business Insider. 2017. “Exploring Agricultural Drones: The Future of Farming Is Precision Agriculture, Mapping, and Spraying,” August 1, 2017. <http://www.businessinsider.com/farming-drones-precision-agriculture-mapping-spraying-2017-8?international=true&r=US&IR=T>.
- Campbell, J., and R. Wynne. 2011. *Introduction to Remote Sensing*. Guilford Press. <https://www.guilford.com/books/Introduction-to-Remote-Sensing/Campbell-Wynne/9781609181765>.
- Candiago, S., F. Remondino, M. De Giglio, M. Dubbini, and M. Gattelli. 2015. “Evaluating Multispectral Images and Vegetation Indices for Precision Farming Applications from UAV Images.” *Remote Sensing* 7 (4): 4026–47. <https://doi.org/10.3390/rs70404026>.
- Castillejo-González, I., F. López-Granados, A. García-Ferrer, J. Peña, M. Jurado-Expósito, M. de la Orden, and M. González-Audicana. 2009. “Object- and Pixel-Based Analysis for Mapping Crops and Their Agro-Environmental Associated Measures Using QuickBird Imagery.” *Computers and Electronics in Agriculture* 68 (2): 207–15. <https://doi.org/10.1016/j.compag.2009.06.004>.
- CBS. 2017. “De Nederlandse Landbouwexport 2017.” <https://www.cbs.nl/nl-nl/publicatie/2018/03/de-nederlandse-landbouwexport-2017>.
- Chen, Z., N. Zhu, S. Pacheco, X. Wang, and R. Liang. 2014. “Single Camera Imaging System for

- Color and Near-Infrared Fluorescence Image Guided Surgery.” *Biomedical Optics Express* 5 (8): 2791–97. <https://doi.org/10.1364/BOE.5.002791>.
- Cheng, G., and J. Han. 2016. “A Survey on Object Detection in Optical Remote Sensing Images.” *ISPRS Journal of Photogrammetry and Remote Sensing* 117 (July): 11–28. <https://doi.org/10.1016/j.isprsjprs.2016.03.014>.
- Cho, M.A., A. Skidmore, F. Corsi, S.E. van Wieren, and I. Sobhan. 2007. “Estimation of Green Grass/Herb Biomass from Airborne Hyperspectral Imagery Using Spectral Indices and Partial Least Squares Regression.” *International Journal of Applied Earth Observation and Geoinformation* 9 (4): 414–24. <https://doi.org/10.1016/j.jag.2007.02.001>.
- Ciganda, V., A. Gitelson, and J. Schepers. 2009. “Non-Destructive Determination of Maize Leaf and Canopy Chlorophyll Content.” *Journal of Plant Physiology* 166 (2): 157–67. <https://doi.org/10.1016/J.JPLPH.2008.03.004>.
- Clark, M., W. Horwath, C. Shennan, and K. Scow. 1976. “Changes in Soil Chemical Properties Resulting from Organic and Low-Input Farming Practices.” *Can. J. Plant Sci. Microscale Agric. Agron. J* 66 (70). doi:10.2134/agronj1998.00021962009000050016x.
- Clevers, J., and L. Kooistra. 2012. “Using Hyperspectral Remote Sensing Data for Retrieving Canopy Chlorophyll and Nitrogen Content.” *Journal of Selected Topics in Applied Earth Observation and Remote Sensing* 5 (2): 574–83.
- Colomina, I, and P Molina. 2014. “Unmanned Aerial Systems for Photogrammetry and Remote Sensing: A Review.” <https://doi.org/10.1016/j.isprsjprs.2014.02.013>.
- Cortois, R., T. Schröder-Georgi, A. Weigelt, W. van der Putten, and G. de Deyn. 2016. “Plant–soil Feedbacks: Role of Plant Functional Group and Plant Traits.” *Journal of Ecology* 104 (6): 1608–17. <https://doi.org/10.1111/1365-2745.12643>.
- Dash, J, and P.J. Curran. 2004. “International Journal of Remote Sensing The MERIS Terrestrial Chlorophyll Index The MERIS Terrestrial Chlorophyll Index.” *International Journal of Remote Sensing* 2523 (March): 5403–13. <https://doi.org/10.1080/0143116042000274015>.
- Daughtry, C.S.T., C.L. Walthall, M.S. Kim, E. Brown de Colstoun, and J.E. McMurtrey. 2000. “Estimating Corn Leaf Chlorophyll Concentration from Leaf and Canopy Reflectance.” *Remote Sensing of Environment* 74 (2): 229–39. [https://doi.org/10.1016/S0034-4257\(00\)00113-9](https://doi.org/10.1016/S0034-4257(00)00113-9).
- Dixon, J., and M. McCann. 1997. *Precision Agriculture in the 21st Century. Geospatial and Information Technologies in Crop Management*. Washington DC. Washington, D.C.: National Academies Press. <https://doi.org/10.17226/5491>.
- Evert, F. van, R. Booij, J. Jukema, H. ten Berge, D. Uenk, E. Meurs, W. van Geel, K. Wijnholds, and J.J.H. Slabbekoorn. 2012. “Using Crop Reflectance to Determine Sidedress N Rate in Potato Saves N and Maintains Yield.” *European Journal of Agronomy* 43: 58–67. <https://doi.org/10.1080/19404158.2016.1189443>.
- Feng, Q., J. Liu, and J. Gong. 2015. “UAV Remote Sensing for Urban Vegetation Mapping Using Random Forest and Texture Analysis.” *Remote Sensing* 7 (12): 1074–94. <https://doi.org/10.3390/rs70101074>.
- Filella, I., L. Serrano, J. Serra, and J. Penuelas. 1995. “Evaluating Wheat Nitrogen Status with



- Canopy Reflectance Indices and Discriminant Analysis.” *Crop Science* 35 (5): 1400–1405. <https://doi.org/10.2135/cropsci1995.0011183X003500050023x>.
- Financial Times. 2017. “Precision Farming Will Feed the World the Green Way,” December 8, 2017. <https://www.ft.com/content/3eac4ec2-c569-11e7-b30e-a7c1c7c13aab>.
- Fischler, M., and R. Elschlager. 1970. “The Representation and Matching of Pictorial Structures.” *Ieee Transactions on Computers* 711 (1): 22–287. <https://ieeexplore.ieee.org/document/1672195/>.
- Fisher, R.A. 1928. “The General Sampling Distribution of the Multiple Correlation Coefficient.” *Proceedings of the Royal Society A: Mathematical, Physical and Engineering Sciences* 121 (788): 654–73. <https://doi.org/10.1098/rspa.1928.0224>.
- Flanders, D., M. Hall-Beyer, and J. Pereverzoff. 2003. “Preliminary Evaluation of ECognition Object-Based Software for Cut Block Delineation and Feature Extraction.” *Canadian Journal of Remote Sensing* 29 (4): 441–52. <https://doi.org/10.5589/m03-006>.
- Franceschini, M., H. Bartholomeus, D. van Apeldoorn, J. Suomalainen, and L. Kooistra. 2017. “Intercomparison of Unmanned Aerial Vehicle and Ground-Based Narrow Band Spectrometers Applied to Crop Trait Monitoring in Organic Potato Production.” *Sensors (Switzerland)* 17 (6). <https://doi.org/10.3390/s17061428>.
- Gates, D., H. Keegan, J. Schleiter, and V. Weidner. 1965. “Spectral Properties of Plants.” *Applied Optics* 4 (1): 11. <https://doi.org/10.1364/AO.4.000011>.
- Gitelson, A.A., Y. Gritz †, and M.N. Merzlyak. 2003. “Relationships between Leaf Chlorophyll Content and Spectral Reflectance and Algorithms for Non-Destructive Chlorophyll Assessment in Higher Plant Leaves.” *Journal of Plant Physiology* 160 (3): 271–82. <https://doi.org/10.1078/0176-1617-00887>.
- Goodbody, T., N.C. Coops, P.L. Marshall, P. Tompalski, and P. Crawford. 2017. “Unmanned Aerial Systems for Precision Forest Inventory Purposes: A Review and Case Study.” *The Forestry Chronicle* 93 (01): 71–81. <https://doi.org/10.5558/tfc2017-012>.
- Gunasekaran, S. 1996. “Computer Vision Technology for Food Quality Assurance.” *Trends in Food Science and Technology* 7 (8): 245–56. [https://doi.org/10.1016/0924-2244\(96\)10028-5](https://doi.org/10.1016/0924-2244(96)10028-5).
- Guo, T., T. Kujirai, and T. Watanabe. 2012. “Mapping Crop Status From an Unmanned Aerial Vehicle for Precision Agriculture Applications.” *ISPRS - International Archives of the Photogrammetry, Remote Sensing and Spatial Information Sciences* 39 (B1): 485–90. <https://doi.org/10.5194/isprsarchives-XXXIX-B1-485-2012>.
- Haboudane, D., J.R. Miller, N. Tremblay, P.J. Zarco-Tejada, and L. Dextraze. 2002. “Integrated Narrow-Band Vegetation Indices for Prediction of Crop Chlorophyll Content for Application to Precision Agriculture.” *Remote Sensing of Environment* 81 (2–3): 416–26. [https://doi.org/10.1016/S0034-4257\(02\)00018-4](https://doi.org/10.1016/S0034-4257(02)00018-4).
- Hauke, J., and T. Kossowski. 2011. “Comparison of Values of Pearson’s and Spearman’s Correlation Coefficients on the Same Sets of Data.” *Quaestiones Geographicae* 30 (2): 87–93. <https://doi.org/10.2478/v10117-011-0021-1>.
- Hay, G., and G. Castilla. 2008. “Geographic Object-Based Image Analysis (GEOBIA): A New Name for a New Discipline.” *Object-Based Image Analysis*, 75–89.

[https://doi.org/10.1007/978-3-540-77058-9\\_4](https://doi.org/10.1007/978-3-540-77058-9_4).

- Heinze, J., J. Bergmann, M. Rillig, and J. Joshi. 2015. "Negative Biotic Soil-Effects Enhance Biodiversity by Restricting Potentially Dominant Plant Species in Grasslands." *Perspectives in Plant Ecology, Evolution and Systematics* 17 (3): 227–35. <https://doi.org/10.1016/J.PPEES.2015.03.002>.
- Hodge, A., D. Robinson, and A. Fitter. 2000. "Are Microorganisms More Effective than Plants at Competing for Nitrogen?" *Trends in Plant Science* 5 (7): 304–8. [https://doi.org/10.1016/S1360-1385\(00\)01656-3](https://doi.org/10.1016/S1360-1385(00)01656-3).
- Houborg, R., J. Fisher, and A. Skidmore. 2015. "Advances in Remote Sensing of Vegetation Function and Traits." *International Journal of Applied Earth Observation and Geoinformation* 43: 1–6. <https://doi.org/10.1016/j.jag.2015.06.001>.
- Hung, C., M. Bryson, and S. Sukkarieh. 2012. "Multi-Class Predictive Template for Tree Crown Detection." *ISPRS Journal of Photogrammetry and Remote Sensing* 68 (March): 170–83. <https://doi.org/10.1016/J.ISPRSJPRS.2012.01.009>.
- Jones, C., N. Maness, M. Stone, and R. Jayasekara. 2007. "Chlorophyll Estimation Using Multispectral Reflectance and Height Sensing." In *Transactions of the ASABE*, 50:1867–72. St. Joseph, MI: American Society of Agricultural and Biological Engineers. <https://doi.org/10.13031/2013.23938>.
- Kalantar, B., S.B. Mansor, H. Zulhaidi, M. Shafri, and A.A. Halin. 2017. "Integration of Template Matching and Object-Based Image Analysis for Semi-Automatic Oil Palm Tree Counting in UAV Images." *The 37th Asian Conference on Remote Sensing* March. <https://www.researchgate.net/publication/314592054>.
- Kooistra, L., and J. Clevers. 2016. "Estimating Potato Leaf Chlorophyll Content Using Ratio Vegetation Indices." *Remote Sensing Letters* 7 (6): 611–20. <https://doi.org/10.1080/2150704X.2016.1171925>.
- Kulmatiski, A., K.H. Beard, J.R. Stevens, and S.M. Cobbold. 2008. "Plant-Soil Feedbacks: A Meta-Analytical Review." *Ecology Letters* 11 (9): 980–92. <https://doi.org/10.1111/j.1461-0248.2008.01209.x>.
- Ledgard, S. 2001. "Nitrogen Cycling in Low Input Legume-Based Agriculture, with Emphasis on Legume/Grass Pastures." *Plant and Soil* 228 (1): 43–59. <https://doi.org/10.1023/A:1004810620983>.
- Lefsky, M.A., W.B. Cohen, G.B. Parker, and D.J. Harding. 2002. "Lidar Remote Sensing for Ecosystem Studies." *BioScience* 52 (1): 19–30. [https://doi.org/10.1641/0006-3568\(2002\)052\[0019:lrsfes\]2.0.co;2](https://doi.org/10.1641/0006-3568(2002)052[0019:lrsfes]2.0.co;2).
- Lewis, J.P. 1995. "Fast Template Matching Template Matching by Cross Correlation 2 Normalized Cross Correlation Normalized Cross Correlation in the Transform Domain." *Pattern Recognition* 10 (11): 120–23. <http://citeseerx.ist.psu.edu/viewdoc/download?doi=10.1.1.157.3888&rep=rep1&type=pdf>.
- Mckinnon, T., and P. Hoff. 2017. "Comparing RGB-Based Vegetation Indices With NDVI For Drone Based Agricultural Sensing." *Agribotix.Com*, 1–8. <https://agribotix.com/wp->

content/uploads/2017/05/Agribotix-VARI-TGI-Study.pdf.

- McNamara, G., J. Larson, S. Schwartz, and M. Davidson. 2009. "Spectral Imaging and Linear Unmixing." *MicroscopyU*. Nikon MicroscopyU. <http://www.microscopyu.com/articles/confocal/spectralimaging.html>.
- Meij, B. van der, L. Kooistra, J. Suomalainen, J. Barel, and G. de Deyn. 2017. "Remote Sensing of Plant Trait Responses to Field-Based Plant–soil Feedback Using UAV-Based Optical Sensors." *Biogeosciences* 14: 733–49. <https://doi.org/10.5194/bg-14-733-2017>.
- Mueller, T.G., N.B. Pusuluri, K.K. Mathias, P.L. Cornelius, R.I. Barnhisel, and S.A. Shearer. 2004. "Map Quality for Ordinary Kriging and Inverse Distance Weighted Interpolation." *Soil Science Society of America Journal* 68 (6): 2042. <https://doi.org/10.2136/sssaj2004.2042>.
- Mulla, D. 2013. "Twenty Five Years of Remote Sensing in Precision Agriculture: Key Advances and Remaining Knowledge Gaps." *Biosystems Engineering* 114 (4): 358–71. <https://doi.org/10.1016/J.BIOSYSTEMSENG.2012.08.009>.
- Mulla, D., P. Gowda, W. Koskinen, B. Khakural, G. Johnson, and P. Robert. 2002. "Modeling the Effect of Precision Agriculture: Pesticide Losses to Surface Waters." In , 304–17. <https://doi.org/10.1021/bk-2002-0842.ch020>.
- Neubert, M., and G. Meinel. 2001. "Evaluation of Segmentation Programs for High Resolution Remote Sensing Applications." *City*, no. 1985. [http://www.ecognition.com/sites/default/files/356\\_neubert.pdf](http://www.ecognition.com/sites/default/files/356_neubert.pdf).
- Nex, F., and F. Remondino. 2014. "UAV for 3D Mapping Applications: A Review." *Applied Geomatics* 6 (1): 1–15. <https://doi.org/10.1007/s12518-013-0120-x>.
- Ouédraogo, M., A. Degré, C. Debouche, and J. Lisein. 2014. "The Evaluation of Unmanned Aerial System-Based Photogrammetry and Terrestrial Laser Scanning to Generate DEMs of Agricultural Watersheds." *Geomorphology* 214 (June): 339–55. <https://doi.org/10.1016/J.GEOMORPH.2014.02.016>.
- Peña-Barragán, J., P. Gutiérrez, C. Hervás-Martínez, J. Six, R.E. Plant, and F. López-Granados. 2014. "Object-Based Image Classification of Summer Crops with Machine Learning Methods." *Remote Sensing* 6 (6): 5019–41. <https://doi.org/10.3390/rs6065019>.
- Peña-Barragán, J., M. Kelly, A.I. de Castro, and F. López-Granados. 2012. "Object-Based Approach for Crop Row Characterization in Uav Images for Site-Specific Weed Management." *Proceedings of the 4th GEOBIA*, no. May 2011: 426–30. [digital.csic.es/bitstream/10261/98054/1/approach\\_crop\\_Pena.pdf](http://digital.csic.es/bitstream/10261/98054/1/approach_crop_Pena.pdf).
- Platt, R., and L. Rapoza. 2008. "An Evaluation of an Object-Oriented Paradigm for Land Use/Land Cover Classification\*." *The Professional Geographer* 60 (1): 87–100. <https://doi.org/10.1080/00330120701724152>.
- Postgate, J. 1998. "The Origins of the Unit of Nitrogen Fixation at the University of Sussex." *Notes and Records of the Royal Society of London*. Royal Society. <https://doi.org/10.1098/rsnr.1998.0055>.
- Pouliot, D., and D. King. 2014. "Approaches for Optimal Automated Individual Tree Crown Detection in Regenerating Coniferous Forests." *Canadian Journal of Remote Sensing*. <https://doi.org/10.5589/m05-011>.

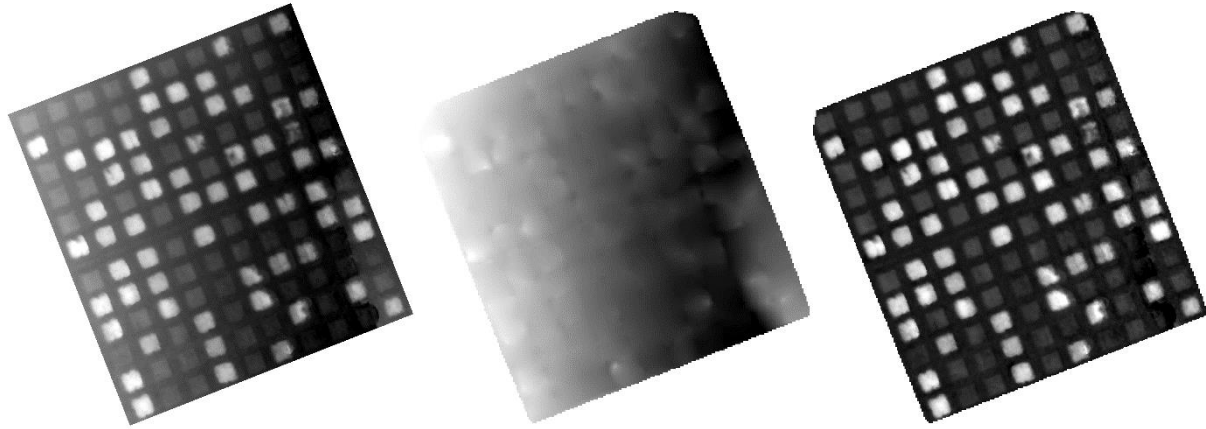
- Pouliot, D., D. King, and D. Pitt. 2005. "Development and Evaluation of an Automated Tree Detection-Delineation Algorithm for Monitoring Regenerating Coniferous Forests." <https://doi.org/10.1139/X05-145>.
- Putten, W. van der, R. Bardgett, J. Bever, T. Bezemer, B. Casper, T. Fukami, P. Kardol, et al. 2013. "Plant-Soil Feedbacks: The Past, the Present and Future Challenges." Edited by Michael Hutchings. *Journal of Ecology* 101 (2): 265–76. <https://doi.org/10.1111/1365-2745.12054>.
- Rabatel, G., N Gorretta, and S. Labbé. 2011. "Getting NDVI Spectral Bands from a Single Standard RGB Digital Camera: A Methodological Approach." *Computer Science* 7023: 333–42. [https://doi.org/10.1007/978-3-642-25274-7\\_34](https://doi.org/10.1007/978-3-642-25274-7_34).
- Rasmussen, J., G. Ntakos, J. Nielsen, J. Svensgaard, R. Poulsen, and S. Christensen. 2016. "Are Vegetation Indices Derived from Consumer-Grade Cameras Mounted on UAVs Sufficiently Reliable for Assessing Experimental Plots?" *European Journal of Agronomy* 74: 75–92. <https://doi.org/10.1016/j.eja.2015.11.026>.
- Richards, J.A. 2013. *Remote Sensing Digital Image Analysis*. Berlin, Heidelberg: Springer Berlin Heidelberg. <https://doi.org/10.1007/978-3-642-30062-2>.
- Roosjen, P.J., B. Brede, J.M. Suomalainen, H.M. Bartholomeus, L. Kooistra, and J.G.P.W. Clevers. 2018. "Improved Estimation of Leaf Area Index and Leaf Chlorophyll Content of a Potato Crop Using Multi-Angle Spectral Data – Potential of Unmanned Aerial Vehicle Imagery." *International Journal of Applied Earth Observation and Geoinformation* 66: 14–26. <https://doi.org/10.1016/j.jag.2017.10.012>.
- Soper, H.E., A.W. Young, B.M. Cave, A. Lee, and K. Pearson. 1932. "On the Distribution of the Correlation Coefficient in Small Samples." *Biometrika* 24 (3): 382–403. <http://www.jstor.org/stable/2331830> <http://about.jstor.org/terms>.
- Stumpf, A., and N. Kerle. 2011. "Object-Oriented Mapping of Landslides Using Random Forests." *Remote Sensing of Environment* 115: 2564–77. <https://doi.org/10.1016/j.rse.2011.05.013>.
- Suomalainen, J., N. Anders, S. Iqbal, G. Roerink, J. Franke, P. Wenting, D. Hünninger, H. Bartholomeus, R. Becker, and L. Kooistra. 2014. "A Lightweight Hyperspectral Mapping System and Photogrammetric Processing Chain for Unmanned Aerial Vehicles." *Remote Sensing* 6 (12): 11013–30. <https://doi.org/10.3390/rs6111013>.
- Tao, W., H. Jin, and Y. Zhang. 2007. "Color Image Segmentation Based on Mean Shift and Normalized Cuts." *IEEE Transactions on Systems, Man, and Cybernetics, Part B: Cybernetics* 37 (5): 1382–89. <https://doi.org/10.1109/TSMCB.2007.902249>.
- Tian, L. 2002. "Development of a Sensor-Based Precision Herbicide Application System." *Computers and Electronics in Agriculture* 36 (2–3): 133–49. [https://doi.org/10.1016/S0168-1699\(02\)00097-2](https://doi.org/10.1016/S0168-1699(02)00097-2).
- Tian, Y.C., X. Yao, J. Yang, W.X. Cao, D.B. Hannaway, and Y. Zhu. 2011. "Assessing Newly Developed and Published Vegetation Indices for Estimating Rice Leaf Nitrogen Concentration with Ground- and Space-Based Hyperspectral Reflectance." *Field Crops Research* 120 (2): 299–310. <https://doi.org/10.1016/j.fcr.2010.11.002>.
- Tiede, D. 2014. "A New Geospatial Overlay Method for the Analysis and Visualization of Spatial Change Patterns Using Object-Oriented Data Modeling Concepts." *Cartography and*

- Tiede, D., P. Krafft, P. Füreder, and S. Lang. 2017. “Stratified Template Matching to Support Refugee Camp Analysis in OBIA Workflows.” *Remote Sensing* 9 (4): 326. <https://doi.org/10.3390/rs9040326>.
- Tilly, N., D. Hoffmeister, Q. Cao, S. Huang, V. Lenz-Wiedemann, Y. Miao, and G. Bareth. 2014. “Multitemporal Crop Surface Models: Accurate Plant Height Measurement and Biomass Estimation with Terrestrial Laser Scanning in Paddy Rice.” *Journal of Applied Remote Sensing* 8 (1): 083671. <https://doi.org/10.1117/1.JRS.8.083671>.
- Torres-Sánchez, J., F. López-Granados, and J. M. Peña. 2015. “An Automatic Object-Based Method for Optimal Thresholding in UAV Images: Application for Vegetation Detection in Herbaceous Crops.” *Computers and Electronics in Agriculture* 114: 43–52. <https://doi.org/10.1016/j.compag.2015.03.019>.
- Tucker, C. 1979. “Red and Photographic Infrared Linear Combinations for Monitoring Vegetation.” *Remote Sensing of Environment* 8 (2): 127–50. <https://ntrs.nasa.gov/archive/nasa/casi.ntrs.nasa.gov/19780024582.pdf>.
- United Nations Department of Economic and Social Affairs, Population Division. 2017. “World Population Prospects The 2017 Revision Key Findings and Advance Tables.” *World Population Prospects The 2017*. <https://doi.org/10.1017/CBO9781107415324.004>.
- Vastaranta, M., M.A. Wulder, J.C. White, A. Pekkarinen, S. Tuominen, C. Ginzler, Vi. Kankare, M. Holopainen, and H. Hyypä. 2014. “Airborne Laser Scanning and Digital Stereo Imagery Measures of Forest Structure : Comparative Results and Implications to Forest Mapping and Inventory Update.” *Can. J. Remote Sensing* 39 (5): 382–95. <https://doi.org/10.5589/m13-046>.
- Verhoeff, E. 2017. “Automatic Scoring of Germination in the Field, Based on UAV Acquired High Resolution Imagery.” *Wur Msc. Thesis*. Wageningen University. <https://www.wur.nl/en/activity/Automatic-scoring-of-germination-in-the-field-based-on-UAV-acquired-high-resolution-images>.
- Vincini, M., E. Frazzi, and P. D’Alessio. 2008. “A Broad-Band Leaf Chlorophyll Vegetation Index at the Canopy Scale.” *Precision Agriculture* 9 (5): 303–19. <https://doi.org/10.1007/s11119-008-9075-z>.
- Wang, L., W. Sousa, and P. Gong. 2004. “Integration of Object-Based and Pixel-Based Classification for Mapping Mangroves with IKONOS Imagery.” *International Journal of Remote Sensing* 25 (24): 5655–68. <https://doi.org/10.1080/014311602331291215>.
- Wang, N., N. Zhang, and M. Wang. 2006. “Wireless Sensors in Agriculture and Food Industry—Recent Development and Future Perspective.” *Computers and Electronics in Agriculture* 50: 1–14. <https://doi.org/10.1016/j.compag.2005.09.003>.
- Westoby, M., J. Brasington, N. Glasser, M. Hambrey, and J. Reynolds. 2012. “‘Structure-from-Motion’ Photogrammetry: A Low-Cost, Effective Tool for Geoscience Applications.” *Geomorphology* 179 (December): 300–314. <https://doi.org/10.1016/J.GEOMORPH.2012.08.021>.
- Williamson, D.F., R.A. Parker, and J.S. Kendrick. 1989. “The Box Plot: A Simple Visual Method

- to Interpret Data.” *Annals of Internal Medicine* 110 (11): 916–21. <https://doi.org/10.7326/0003-4819-110-11-916>.
- World Bank. 2018. “Population, Total | Data.” 2018. <https://data.worldbank.org/indicator/SP.POP.TOTL>.
- Wu, C., Z. Niu, Q. Tang, and W. Huang. 2008. “Estimating Chlorophyll Content from Hyperspectral Vegetation Indices: Modeling and Validation.” *Agricultural and Forest Meteorology* 148 (8–9): 1230–41. <https://doi.org/10.1016/j.agrformet.2008.03.005>.
- Xiang, H., and L. Tian. 2011. “Method for Automatic Georeferencing Aerial Remote Sensing (RS) Images from an Unmanned Aerial Vehicle (UAV) Platform.” *Biosystems Engineering* 108 (2): 104–13. <https://doi.org/10.1016/j.biosystemseng.2010.11.003>.
- Yan, G., J. Mas, B. Maathuis, Z. Xiangmin, and P. van Dijk. 2006. “Comparison of Pixel-based and Object-oriented Image Classification Approaches—a Case Study in a Coal Fire Area, Wuda, Inner Mongolia, China.” *International Journal of Remote Sensing* 27 (18): 4039–55. <https://doi.org/10.1080/01431160600702632>.

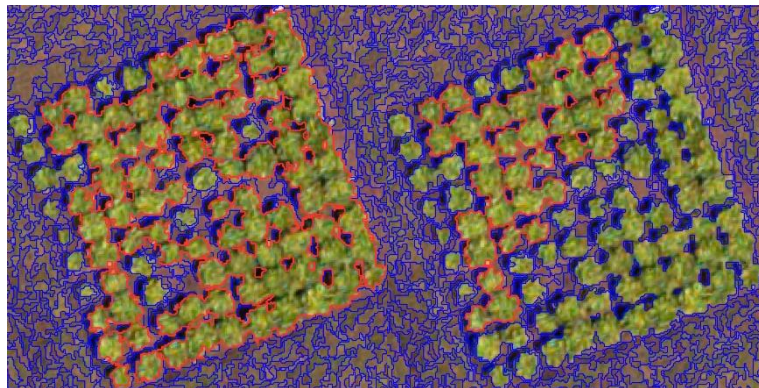
# 12 APPENDICES

IDSMS > DTM > CSM



## II SEGMENTATION TEST LAYER WEIGHT VALUES

Weight value of the green layer is 1 (left) and 20 (right). Using final classification rules.





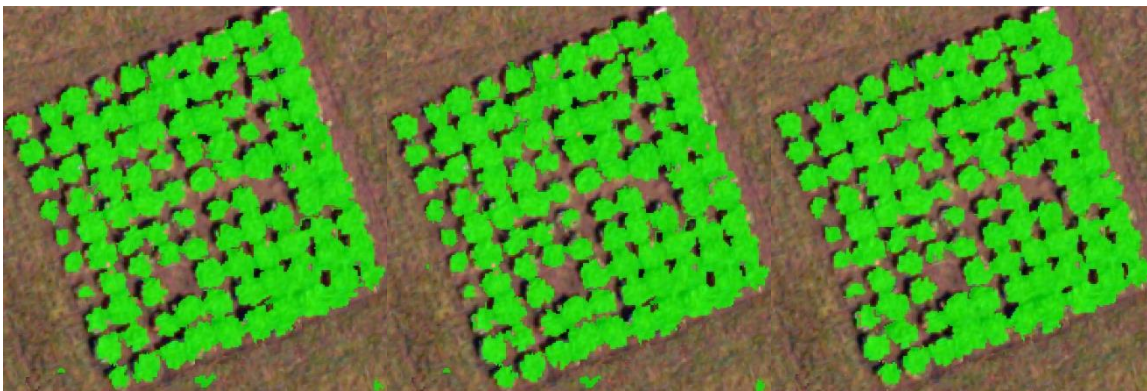
### III SEGMENTATION TEST SCALE-FACTORS

From the left to right image the scale-factor is 5, 10, and 15. Using final classification rules.



### IV SEGMENTATION TEST SHAPE FACTORS

From the left to right image the shape factor is 0.1, 0.2, and 0.5. Using final classification rules.



### V SEGMENTATION TEST COMPACTNESS FACTORS

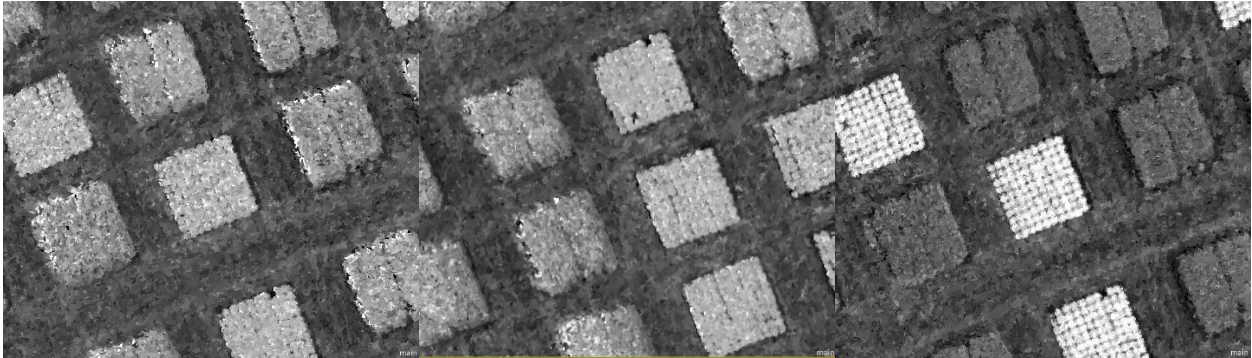
From left to right image compactness factor is 0.1, 0.5, and 0.9. Using final classification rules.





## VI VEGETATION INDICES APPLIED ON RGB IMAGE

From the left to right image the VIs NDVI (RGB version), VARI, and TGI are applied.

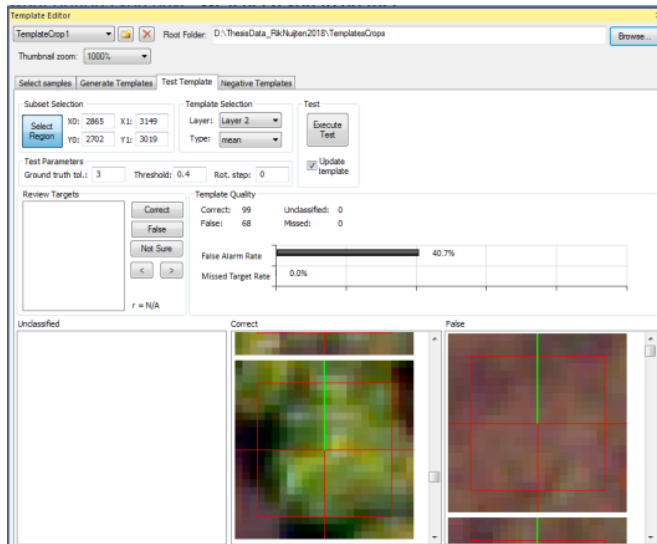
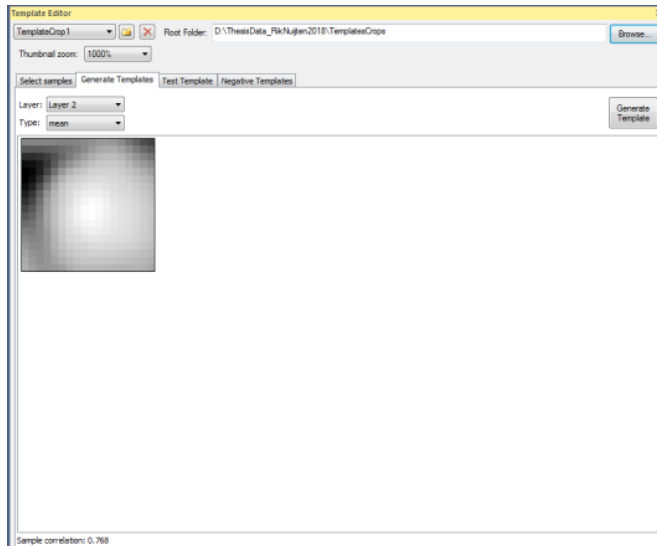
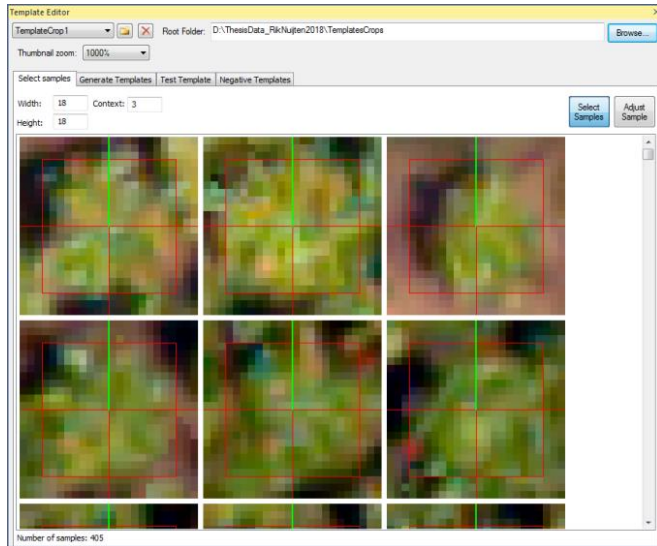


## VII CLASSIFICATION BASED ON TGI VEGETATION INDEX

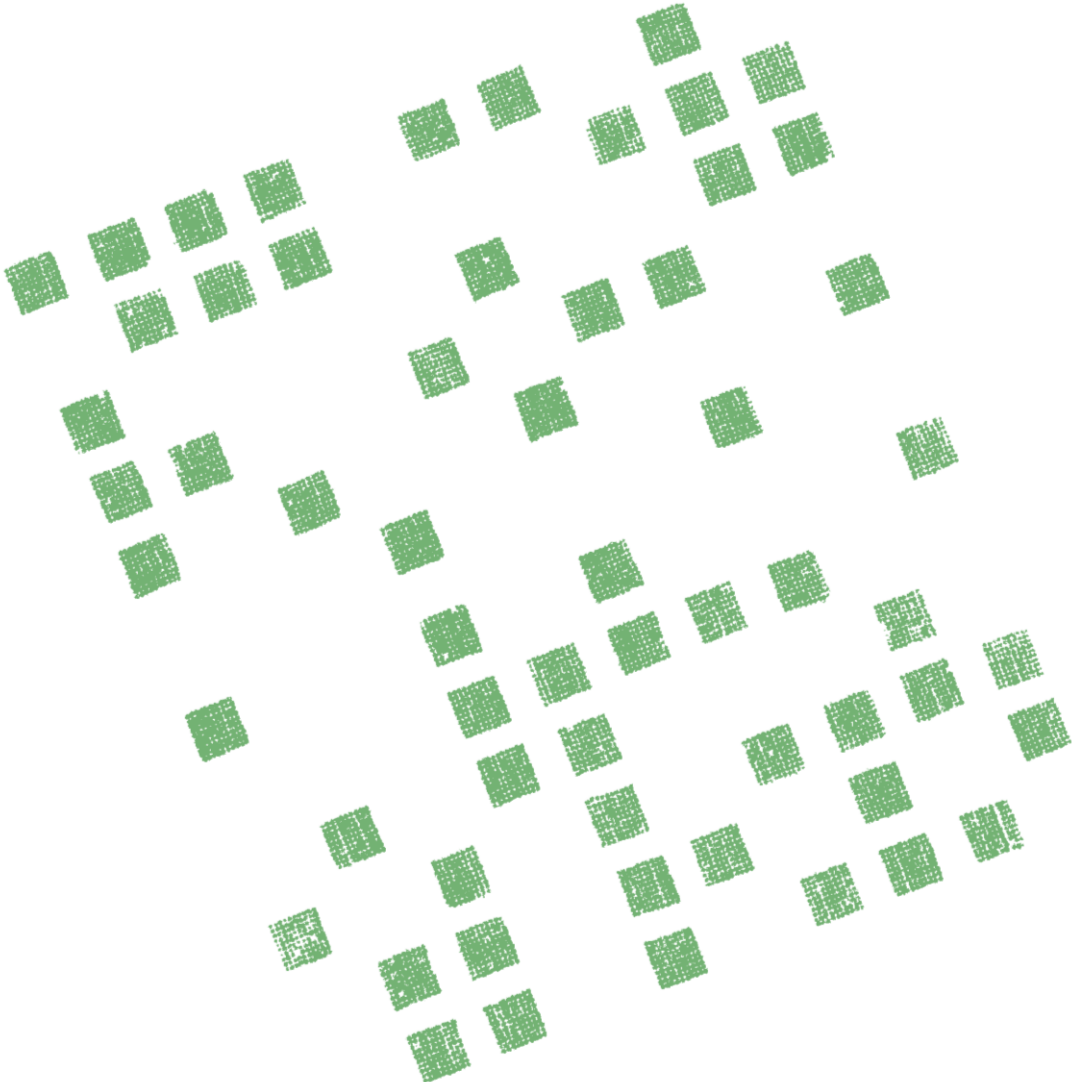
From the left to right image the threshold values are 37, 38, and 39.



# VIII TEMPLATE GENERATION

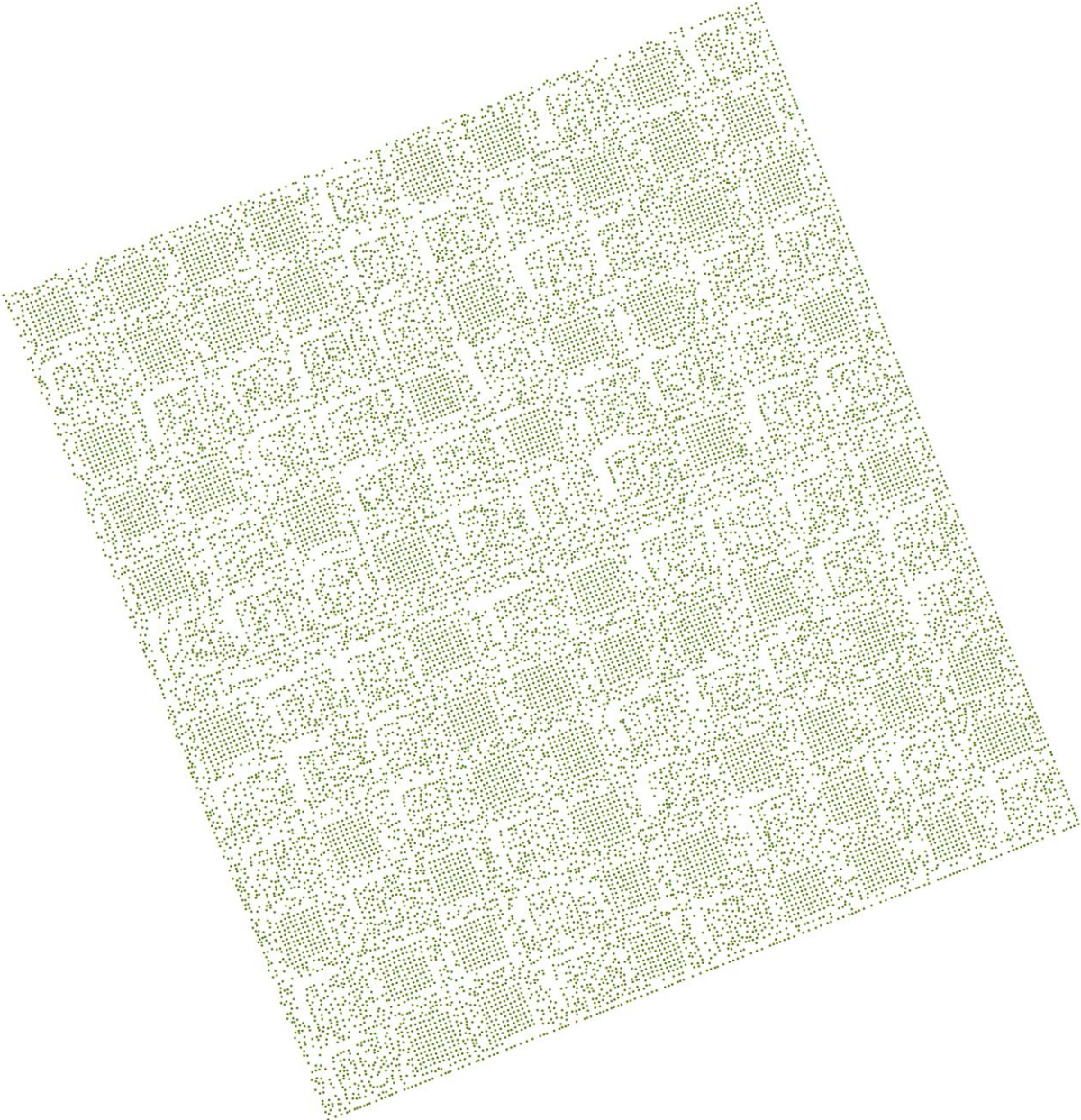


IX OBIA VECTOR-OBJECTS

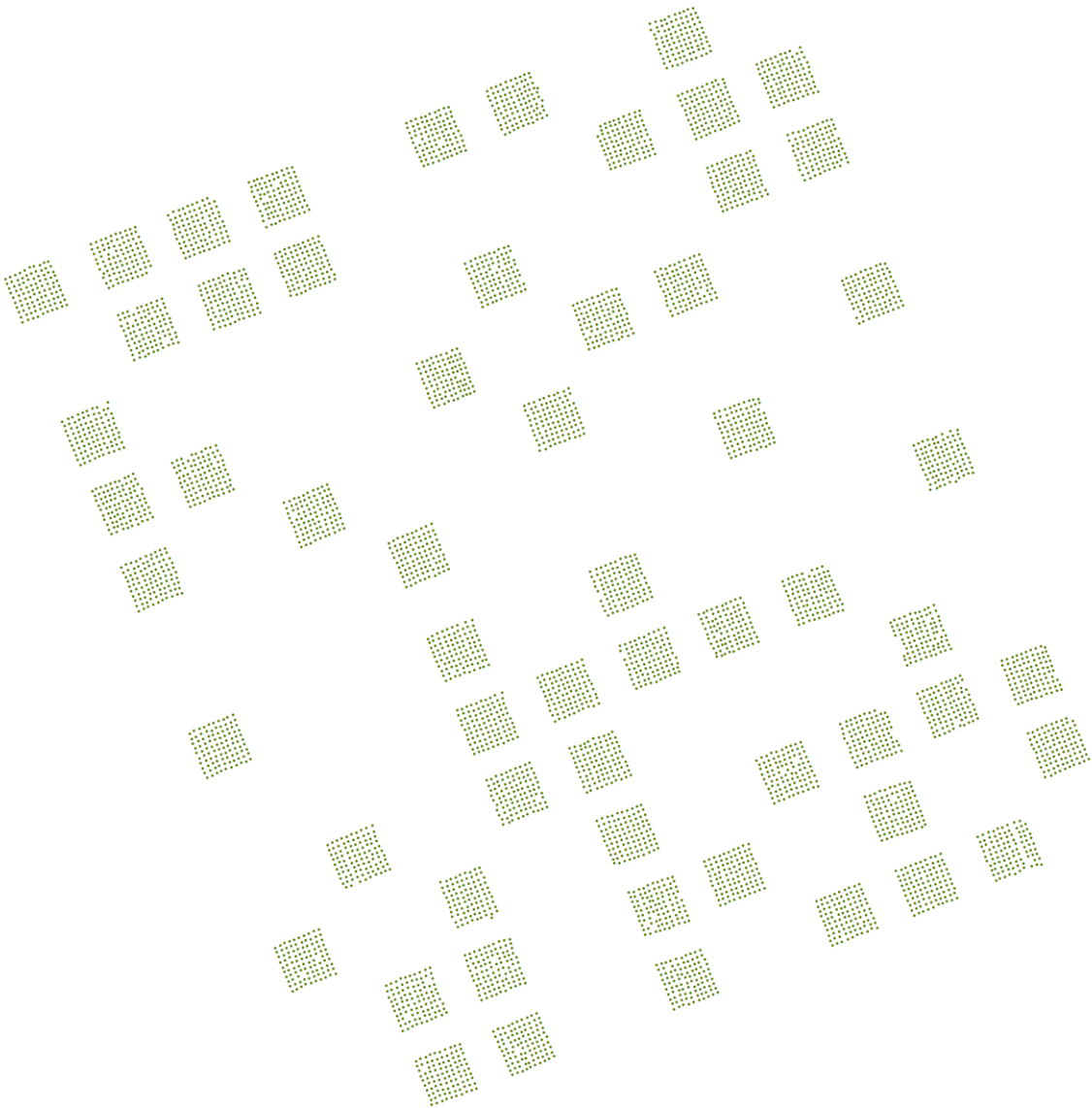




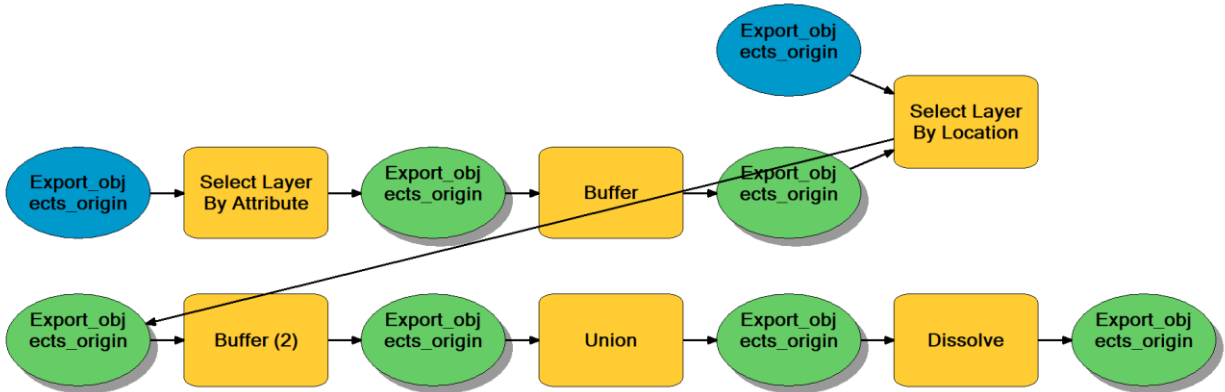
X TM POINT-FEATURES



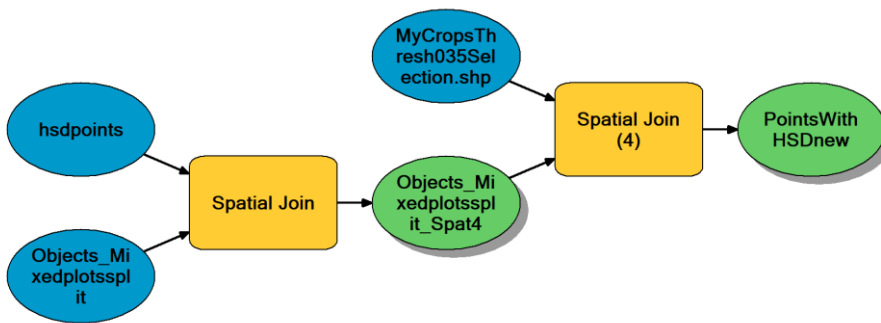
XI POINT-FEATURES RESULTING FROM TM AND OBIA



## XII ARCMAP-WORKFLOW FOR CREATING AOIS



## XIII ARCMAP-WORKFLOW FOR ADDING ATTRIBUTES TO OBJECTS AND POINT-FEATURES



## XIV PYTHON SCRIPT SPECTRAL SIGNATURES

```
import pandas as pd
import numpy as np
import matplotlib.pyplot as plt
import seaborn as sns

#Loads the Excelfile with point-features (crops)
#into a Pandas DataFrame
all_df = pd.read_excel("G:\MyDrive\MyFile.xlsx", index_col=0, header=0, parse_dates=True)

#Create an Numpy array with the wavelength values with steps of 5.
#This array is used to give the columns new column names
m = np.arange(450,920,5)

#A dictionary is build with all available treatments and plotnumbers included
Treatments = {'Fa' : [4, 37, 52, 73, 115, 14, 36, 61, 80, 105],
'lp' : [24, 26, 57, 84, 110, 10, 35, 71, 86, 118],
'Rs' : [3, 42, 63, 96, 97, 23, 45, 65, 88, 106],
'Rs+Vs' : ['5A', '34A', '95A', '111A', '21A', '44A', '67A', '94A', '108A', '59A'],
'lp+Tr' : ['5B', '34B', '95B', '111B', '21B', '44B', '67B', '94B', '108B', '59B'],
'Tr' : [7, 25, 58, 92, 98, 16, 38, 56, 90, 113],
'Vs' : [1, 29, 76, 119, 60, 13, 43, 68, 82, 99]}

#set the style for plotting with Seaborn
sns.set_style("darkgrid")

#Create a new empty figure
plt.figure()

#Sets the labels for the X- and Y-axis
plt.ylabel('Reflectance')
plt.xlabel('Wavelength')

#Loop which is executed for each treatment in the dictionary "Treatments"
for key in Treatments:

    #Creates a new DataFrame with all records from the DataFrame "all_df"
    #with the corresponding Plotname
    df = all_df.loc[all_df["Plot"].isin(Treatments[key])]

    #A new row is added which contains the mean values of all objects for a certain wavelength
    df.loc[str(key)] = df.mean()

    #The DataFrame is transposed
    df = df.T

    #A new DataFrame is created which columns concerning wavelength (450 till 915)
    #Wavelength column names are added with the array "m"
    #This DataFrame is extended with a new treatment with every loop
    select1 = pd.DataFrame(data=df.iloc[4:98,])
    select1["Wavelength"] = m

    #The average reflectance values are plotted with Seaborn
    ax = plt.plot(select1.Wavelength,select1[str(key)])
    ax = plt.legend()
    #Save figure
    plt.savefig("D:\MyDrive\SpectralSignature.pdf",format="pdf")
```

## XV PYTHON SCRIPT VEGETATION INDICES

```
# -*- coding: utf-8 -*-
"""
Created on Thu May 03 15:52:29 2018

@author: riknu
"""
###Load libraries
import pandas as pd
import matplotlib.pyplot as plt
import seaborn as sns

#Loads the Excelfile with point-features (crops)
#into a Pandas DataFrame
all_df = pd.read_excel("G:\MyDrive\MyFile.xlsx", index_col=0, header=0, parse_dates=True)

#All wavelength values are grouped (averaged) on the plot-level.
#Thereafter the index is reset, so the column "Plot" becomes available again for selections etc.
all_df = all_df.groupby(['Plot'])["Mean450", "Mean455", "Mean460", "Mean465", "Mean470",
"Mean475", "Mean480", "Mean485", "Mean490", "Mean495", "Mean500", "Mean505", "Mean510",
"Mean515", "Mean520", "Mean525", "Mean530", "Mean535", "Mean540", "Mean545", "Mean550",
"Mean555", "Mean560", "Mean565", "Mean570", "Mean575", "Mean580", "Mean585", "Mean590",
"Mean595", "Mean600", "Mean605", "Mean610", "Mean615", "Mean620", "Mean625", "Mean630",
"Mean635", "Mean640", "Mean645", "Mean650", "Mean655", "Mean660", "Mean665", "Mean670",
"Mean675", "Mean680", "Mean685", "Mean690", "Mean695", "Mean700", "Mean705", "Mean710",
"Mean715", "Mean720", "Mean725", "Mean730", "Mean735", "Mean740", "Mean745", "Mean750",
"Mean755", "Mean760", "Mean765", "Mean770", "Mean775", "Mean780", "Mean785", "Mean790",
"Mean795", "Mean800", "Mean805", "Mean810", "Mean815", "Mean820", "Mean825", "Mean830",
"Mean835", "Mean840", "Mean845", "Mean850", "Mean855", "Mean860", "Mean865", "Mean870",
"Mean875", "Mean880", "Mean885", "Mean890", "Mean895", "Mean900", "Mean905", "Mean910",
"Mean915"].mean().reset_index()

#Creates a emty list for the treatments per record
treat = []

#The column "Plot" is checked row by row;
#if the value is found than the concerned treatment-name is added to the list "Treat".
for row in all_df['Plot']:
    if row in [4, 37, 52, 73, 115, 14, 36, 61, 80, 105]:
        treat.append('Fa')
    if row in [24, 26, 57, 84, 110, 10, 35, 71, 86, 118]:
        treat.append('Lp')
    if row in [3, 42, 63, 96, 97, 23, 45, 65, 88, 106]:
```



```

        treat.append('Rs')
    if row in ['5A', '34A', '95A', '111A', '21A', '44A', '67A', '94A', '108A', '59A']:
        treat.append('Rs+Vs')
    if row in ['5B', '34B', '95B', '111B', '21B', '44B', '67B', '94B', '108B', '59B']:
        treat.append('Lp+Tr')
    if row in [7, 25, 58, 92, 98, 16, 38, 56, 90, 113]:
        treat.append('Tr')
    if row in [1, 29, 76, 119, 13, 43, 68, 82, 99, 60]:
        treat.append('Vs')

#The list "Treat" is added as a new column to the DataFrame.
all_df["Treatment"]=treat

#Calculate a new column with Vegetation Index formula
all_df["REP"] = 700 + (45*((all_df["Mean670"]+all_df["Mean680"]/2)-all_df["Mean700"])/
(all_df["Mean740"]-all_df["Mean700"])))

all_df["NDVI[650;800]"] = (all_df["Mean800"]-all_df["Mean650"])/
(all_df["Mean800"]+all_df["Mean650"])

all_df["NDVI[735;750]"] = (all_df["Mean750"]-all_df["Mean735"])/
(all_df["Mean750"]+all_df["Mean735"])

all_df["NDVI[720;820]"] = (all_df["Mean820"]-all_df["Mean720"])/
(all_df["Mean820"]+all_df["Mean720"])

all_df["MTCI"] = (all_df["Mean755"]-all_df["Mean710"])/(all_df["Mean710"]-all_df["Mean680"])

all_df["MCARI/MTVI2"] = (((all_df["Mean700"]-all_df["Mean670"]-0.2*(all_df["Mean700"]
-all_df["Mean550"]))*all_df["Mean700"]/all_df["Mean670"])/(1.5*(1.2*(all_df["Mean800"]
-all_df["Mean550"]))-2.5*(all_df["Mean670"]-all_df["Mean550"])/(((2*all_df["Mean800"]+1)**2)
-(6*all_df["Mean800"]-5*(all_df["Mean670"]**0.5))-0.5)**0.5))

all_df["CVI[550;870]"] = (all_df["Mean870"]/all_df["Mean550"])*(all_df["Mean670"]/
all_df["Mean550"])

all_df["TCARI/OSAVI"] = ( 3 * ((all_df["Mean700"]-all_df["Mean670"]) - 0.2
* (all_df["Mean700"] - all_df["Mean550"])) * (all_df["Mean700"] / all_df["Mean670"]) )
/ ( ( (1+0.16) * (all_df["Mean800"] - all_df["Mean670"]) ) / (all_df["Mean750"]
+ all_df["Mean670"] + 0.16) )

```

```

all_df["TCARI/OSAVIre"] = ( 3 * ((all_df["Mean750"]-all_df["Mean705"]) - 0.2
* (all_df["Mean750"] - all_df["Mean550"])) * (all_df["Mean750"] / all_df["Mean705"] )
/ ( ( (1+0.16) * (all_df["Mean750"] - all_df["Mean705"]) ) / (all_df["Mean750"]
+ all_df["Mean705"] + 0.16) )

all_df["MCARI/OSAVI"] = ( ( (all_df["Mean700"]-all_df["Mean670"]) - 0.2
* ( all_df["Mean700"] - all_df["Mean550"] ) ) * (all_df["Mean700"]/all_df["Mean670"] ) )
/ ( ( (1+0.16) * (all_df["Mean800"] - all_df["Mean670"]) ) / ( all_df["Mean800"]
+ all_df["Mean670"] + 0.16 ) )

all_df["MCARI/OSAVIre"] = ( ( (all_df["Mean750"]-all_df["Mean705"]) - 0.2
* ( all_df["Mean750"] - all_df["Mean550"] ) ) * (all_df["Mean750"]/all_df["Mean705"] ) )
/ ( ( (1+0.16) * (all_df["Mean750"] - all_df["Mean705"]) ) / ( all_df["Mean750"]
+ all_df["Mean705"] + 0.16 ) )

all_df["CIgreen"] = (all_df["Mean780"]/all_df["Mean550"]) - 1

all_df["CIre"] = (all_df["Mean780"]/all_df["Mean710"]) - 1

#set the style for plotting with Seaborn
sns.set_style("darkgrid")

#Create a new empty figure
#Define input Seaborn boxplot
#Save figure
plt.figure()
sns.boxplot(x="Treatment", y="REP", data=all_df)
plt.savefig("G:\My Drive\REP.pdf",format="pdf")

plt.figure()
sns.boxplot(x="Treatment", y="NDVI[735;750]", data=all_df)
plt.savefig("G:\My Drive\_NDVI[735;750].pdf",format="pdf")

plt.figure()
sns.boxplot(x="Treatment", y="NDVI[650;800]", data=all_df)
plt.savefig("G:\My Drive\_NDVI[650;800].pdf",format="pdf")

plt.figure()
sns.boxplot(x="Treatment", y="NDVI[720;820]", data=all_df)
plt.savefig("G:\My Drive\_NDVI[720;820].pdf",format="pdf")

```

```

plt.figure()
sns.boxplot(x="Treatment", y="MTCI", data=all_df)
plt.savefig("G:\My Drive\_MTCI.pdf",format="pdf")

plt.figure()
sns.boxplot(x="Treatment", y="MCARI/MTVI2", data=all_df)
plt.savefig("G:\My Drive\_MCARI_MTVI2.pdf",format="pdf")

plt.figure()
sns.boxplot(x="Treatment", y="CVI[550;870]", data=all_df)
plt.savefig("G:\My Drive\_CVI[550;870].pdf",format="pdf")

plt.figure()
sns.boxplot(x="Treatment", y="TCARI/OSAVI", data=all_df)
plt.savefig("G:\My Drive\_TCARI_OSAVI.pdf",format="pdf")

plt.figure()
sns.boxplot(x="Treatment", y="TCARI/OSAVIre", data=all_df)
plt.savefig("G:\My Drive\_TCARI_OSAVIre.pdf",format="pdf")

plt.figure()
sns.boxplot(x="Treatment", y="MCARI/OSAVI", data=all_df)
plt.savefig("G:\My Drive\_MCARI_OSAVI.pdf",format="pdf")

plt.figure()
sns.boxplot(x="Treatment", y="MCARI/OSAVIre", data=all_df)
plt.savefig("G:\My Drive\_MCARI_OSAVIre.pdf",format="pdf")

plt.figure()
sns.boxplot(x="Treatment", y="CIgreen", data=all_df)
plt.savefig("G:\My Drive\_CIgreen.pdf",format="pdf")

plt.figure()
sns.boxplot(x="Treatment", y="CIre", data=all_df)
plt.savefig("G:\My Drive\_CIre.pdf",format="pdf")

```

## XVI PYTHON SCRIPT VOLUME PLOTS

```
# -*- coding: utf-8 -*-
"""
Created on Fri May 04 10:26:11 2018

@author: riknu
"""

###Load libraries
import pandas as pd
import matplotlib.pyplot as plt
import seaborn as sns

#Loads the Excelfile with point-features (crops) including geometric attribute data
#into a Pandas DataFrame
all_df = pd.read_excel("G:\MyDrive\MyFile.xlsx", index_col=0, header=0, parse_dates=True)

#All volume and height values are grouped (averaged) on the plot-level.
#Thereafter the index is reset, so the column "Plot" becomes available again for selections etc.
all_df = all_df.groupby(['Plot'])[['Height', 'Volume']].mean().reset_index()

#Creates a emty list for the treatments per record
treat = []

#The column "Plot" is checked row by row;
#if the value is found than the concerned treatment-name is added to the list "Treat".
for row in all_df['Plot']:
    if row in [4, 37, 52, 73, 115, 14, 36, 61, 80]:
        treat.append('Fa')
    if row in [24, 26, 57, 84, 110, 10, 35, 71, 86, 118]:
        treat.append('Lp')
    if row in [3, 42, 63, 96, 97, 23, 45, 65, 88]:
        treat.append('Rs')
    if row in ['5A', '34A', '95A', '111A', '21A', '44A', '67A', '94A', '59A']:
        treat.append('Rs+Vs')
    if row in ['5B', '34B', '95B', '111B', '21B', '44B', '67B', '94B', '59B']:
        treat.append('Lp+Tr')
    if row in [7, 25, 58, 92, 98, 16, 38, 56, 90, 113]:
        treat.append('Tr')
    if row in [1, 29, 76, 119, 13, 43, 68, 82, 99, 60]:
        treat.append('Vs')

#The list "Treat" is added as a new column to the DataFrame.
all_df["Treatment"]=treat

#set the style for plotting with Seaborn
sns.set_style("darkgrid")

#Create a new empty figure
plt.figure()
#Define input Seaborn barplot
sns.barplot(x="Plot", y="Volume", data=all_df)
#Save figure
plt.savefig("G:\My_Drive\AvgCropVolumesPerPlot.pdf",format="pdf")

#Create a new empty figure
plt.figure()
#Define input Seaborn barplot
sns.barplot(x="Plot", y="Height", data=all_df)
#Save figure
plt.savefig("G:\My_Drive\AvgCropHeightPerPlot.pdf",format="pdf")
```

## XVII PYTHON SCRIPT CORRELATION

```
# -*- coding: utf-8 -*-
"""
Created on Fri May 04 10:26:11 2018

@author: riknu
"""

###Load libraries
import pandas as pd
import matplotlib.pyplot as plt
import seaborn as sns
from scipy.stats.stats import pearsonr
from scipy import stats

##Loads two Excelfiles
#First with point-features (crops) including geometric attribute data
#Second with field measurments
all_df = pd.read_excel("G:\MyDrive\MyFile.xlsx", index_col=0, header=0, parse_dates=True)
insitu_df = pd.read_excel("G:\My Drive\InSitu.xlsx", index_col=0, header=0, parse_dates=True)

#All volume and height values are grouped (averaged) on the plot-level.
#Thereafter the index is reset, so the column "Plot" becomes available again for selections etc.
all_df = all_df.groupby(['Plot'])[['Height', 'Volume']].mean().reset_index()

#Creates a emty list for the treatments per record
treat = []

#The column "Plot" is checked row by row;
#if the value is found than the concerned treatment-name is added to the list "Treat".
for row in all_df['Plot']:
    if row in [4, 37, 52, 73, 115, 14, 36, 61, 80]:
        treat.append('Fa')
    if row in [24, 26, 57, 84, 110, 10, 35, 71, 86, 118]:
        treat.append('Lp')
    if row in [3, 42, 63, 96, 97, 23, 45, 65, 88]:
        treat.append('Rs')
    if row in ['5A', '34A', '95A', '111A', '21A', '44A', '67A', '94A', '59A']:
        treat.append('Rs+Vs')
    if row in ['5B', '34B', '95B', '111B', '21B', '44B', '67B', '94B', '59B']:
        treat.append('Lp+Tr')
    if row in [7, 25, 58, 92, 98, 16, 38, 56, 90, 113]:
        treat.append('Tr')
```

```

    if row in [1, 29, 76, 119, 13, 43, 68, 82, 99, 60]:
        treat.append('Vs')

#The list "Treat" is added as a new column to the DataFrame.
all_df["Treatment"]=treat

#Sets for both Dataframes the Plotnumber as index, this enables an inner join.
all_df = all_df.set_index("Plot")
insitu_df = insitu_df.set_index("PlotComb")

#Joins (inner join) based on the plot numbers
resultjoin = pd.concat([all_df, insitu_df], axis=1, join='inner')

#Creates two new Pandas DataSeries
volume = resultjoin["Volume"]
biomassshoot = resultjoin["WCC.shootM2"]

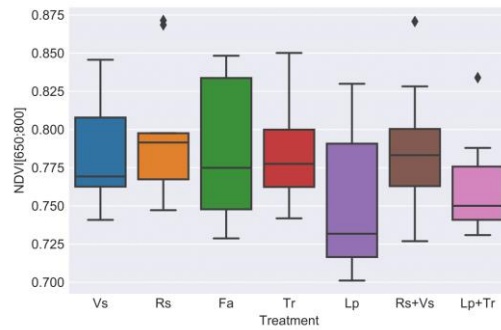
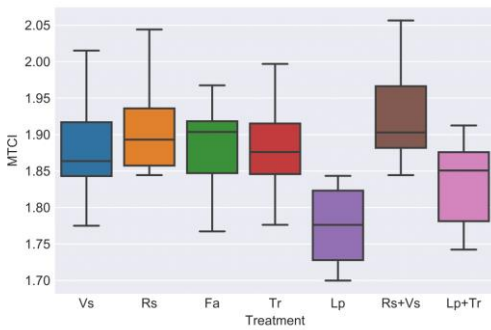
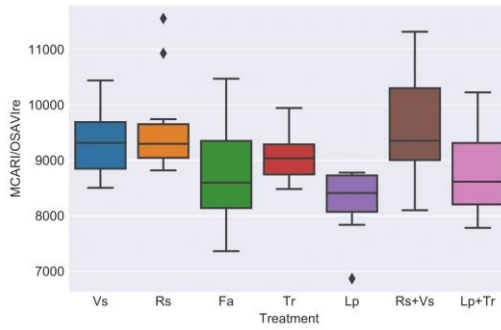
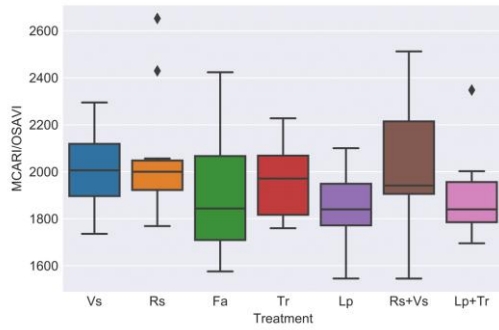
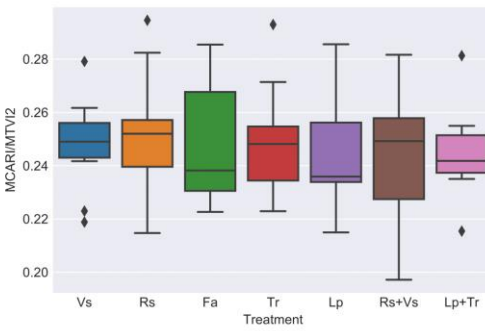
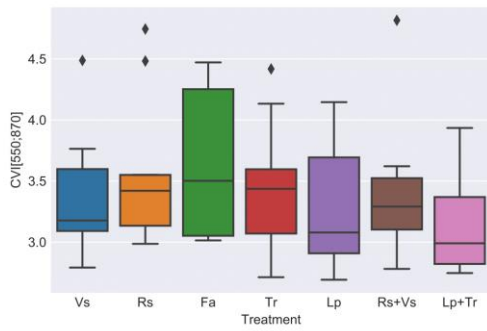
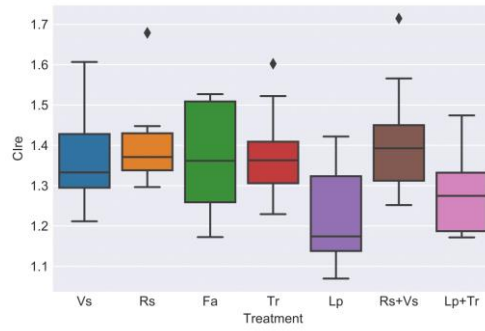
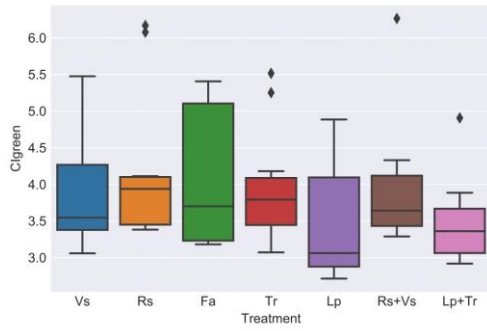
#Pearson coeff. with SciPy
pearsonr_coefficient, p_value_pear = pearsonr(volume,biomassshoot)
print("Pearson R Correlation Coefficient %0.3f" % (pearsonr_coefficient))
print("P-value = "+str(p_value_pear))

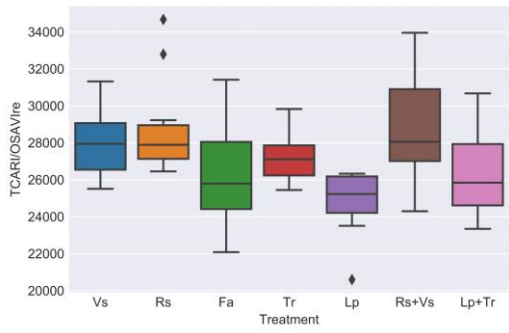
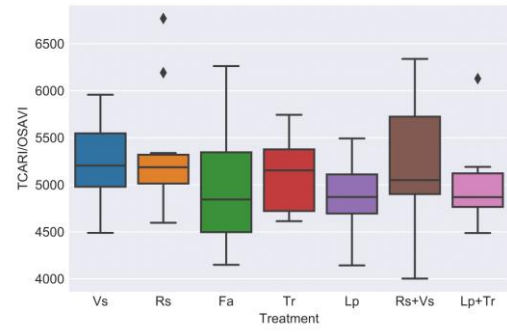
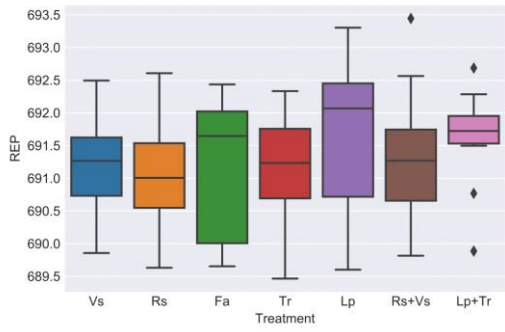
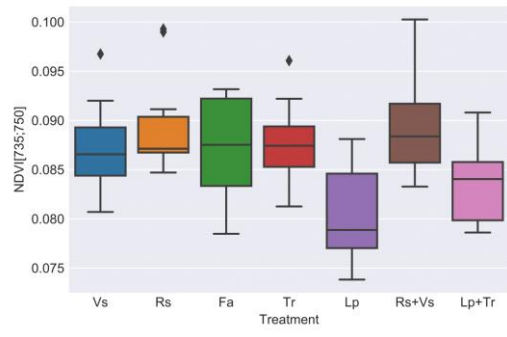
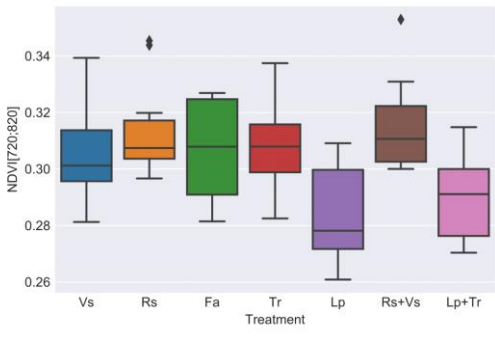
# Spearman coeff. with SciPy
spearman_coefficient, p_value_spear = stats.spearmanr(volume,biomassshoot)
print("Spearman R Correlation Coefficient %0.3f" % (spearman_coefficient))
print("P-value = "+str(p_value_spear))

#Plot figure exploration linearity and normality with Seaborn
plt.figure()
sns.set_style("darkgrid")
sns.pairplot(resultjoin[["Volume", "WCC.shootM2"]])
plt.savefig("G:\My Drive\CorrelationVolumeShoot.pdf",format="pdf")

```

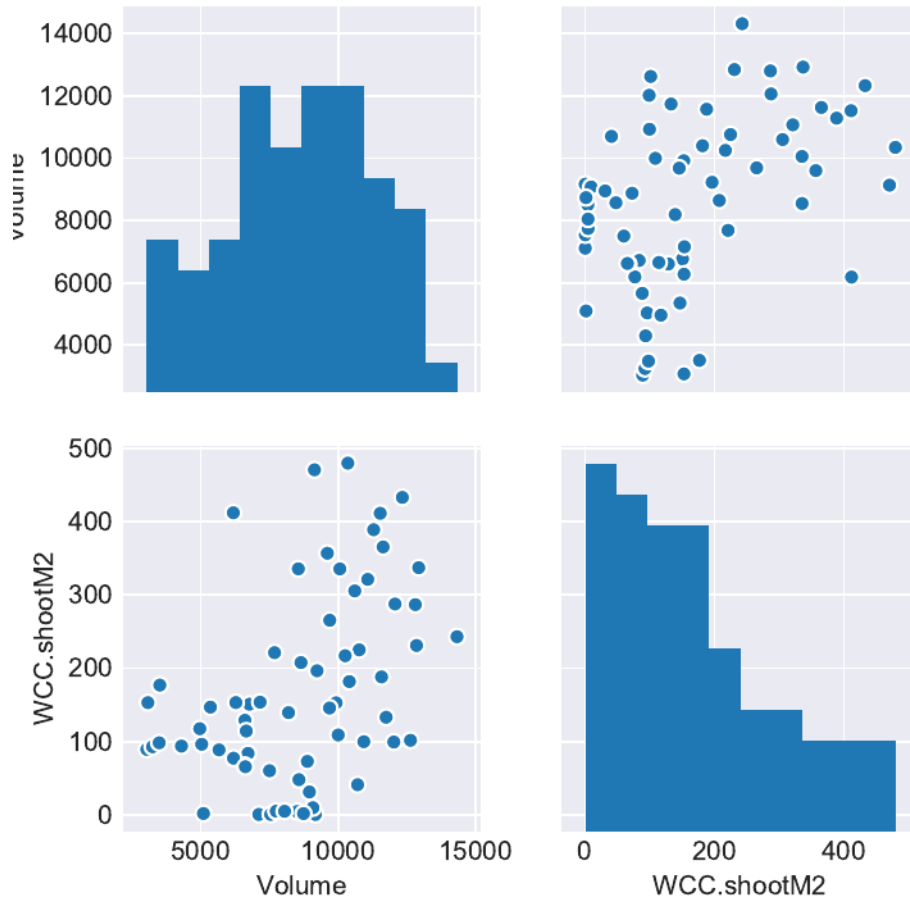
# XVIII VEGETATION INDICES APPLIED PER TREATMENT







# XIX EXPLORATION CORRELATION VOLUME AND SHOOT BIOMASS



XX AVERAGE CROP VOLUME (CM<sup>3</sup>) FOR EACH PLOT

